Simulation of the U.S. Great Plains Low-Level Jet Using Spatially-Coupled Mixed Layer Models

by

Michael Andrew Kistler

Submitted to the Department of Civil and Environmental Engineering
in partial fulfillment of the requirements for the degree of

Master of Science in Civil and Environmental Engineering

at the

MASSACHUSETTS INSTITUTE OF TECHNOLOGY

February 1999

Author .....
Department of Civil and Environmental Engineering
January 15, 1999

Certified by .....
Dara Entekhabi
Associate Professor
Thesis Supervisor

Accepted by .....
Andrew J. Whittle
Chairman, Departmental Committee on Graduate Studies

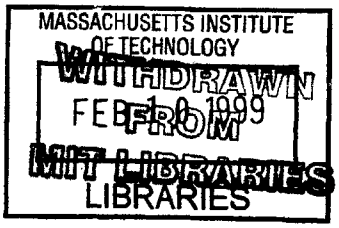

Simulation of the U.S. Great Plains Low-Level Jet Using Spatially-Coupled Mixed Layer Models

by

Michael Andrew Kistler

Submitted to the Department of Civil and Environmental Engineering
on January 15, 1999, in partial fulfillment of the
requirements for the degree of
Master of Science in Civil and Environmental Engineering

Abstract

This project examines the relationship between the Great Plains low-level jet (LLJ) and mixed-layer processes. Enhancing past characterizations of boundary-layer meridional flow, a new solution to the Ekman spiral under baroclinic conditions is derived and tested over the ranges of atmospheric parameters encountered over the Midwest. Implementing the Ekman solution, a set of three preliminary tests investigate meridional energy feedbacks and vapor transport, without mixed-layer interaction. A second group of more sophisticated tests diagnose the effects of both synoptic-scale meridional coupling and local-scale mixed-layer dynamics on the low-level jet. A subset of these experiments examine a hypothesized surface energy-balance-LLJ forcing mechanisms. Models proposed but not constructed for this thesis form a useful starting place for further simulation studies of low-level jet boundary-layer interaction.

Thesis Supervisor: Dara Entekhabi
Title: Associate Professor

Acknowledgments

I thank my parents Barbara and Jeffrey Kistler and my brother Matt for their continual support. I wouldn't have made it to MIT, much less made it out of MIT, without them.

My advisor, Dara, was wonderfully patient and kind with all of my wanderings and instabilities. Sections of this thesis have already reached international venues, via faxes to Iran.

Frank Lee and Peter Hsieh from Ashdown were the first people I met at MIT. They are among my best friends. Jane Brock, Inn Yuk, John Sogade, Yann Schrodi, Derrick Tate, Steve Mascaro, Kevin Ford, Kenneth Lau, Wesley Chan, Dave Kramer, and many others from GCF gave me invaluable support. Scott Rybarczyk and Babar Bhatti were my closest co-laborers in the lab, with whom I fought GAMS and MODFLOW in a noble but fierce battle. Karen Plaut, and Steve Margulis helped me a great deal. Daniel Derksen was very supportive with regard to my time constraints.

My current roomates Brett Conner and Hugh Cox helped me during the darkest hours of this project. Rachel Johnston helped me proofread this beast for spelling and grammar.

Finally, this thesis is an external display of talents and gifts from the Lord Jesus Christ. By His Grace I have not only finished this thesis, but more importantly have received the gift of life to live with Him, both now and eternally.

> Praise the LORD O my soul; all my inmost being, praise his holy name.
> Praise the LORD O my soul, and forget not all his benefits–
> who forgives all your sins and heals your diseases,
> who redeems your life from the pit
> and crowns you with love and compassion,
> who satisfies your desires with good things
> so that your youth is renewed like the eagle's.
> -Psalm 103:1-5 (NIV)

Contents

List of Figures

List of Tables

Chapter 1

Introduction

1.1 The impact of the U.S. Great Plains low-level jet on continental precipitation patterns

In recent years, much attention has been given to the mechanisms governing precipitation production over the the United States Great Plains. Observation records reveal a tendency for this continental region to receive periods of excessive rainfall, far from open bodies of water (Helfand and Schubert 1995, Rasmusson 1967, Arritt et al. 1997). In addition to extreme events, mean precipitation frequency and intensity over the Midwest also exhibit a nighttime maximum. As opposed to other land-locked areas on earth where precipitation is confined to light convective showers during the afternoon, the Midwest receives more rain after dark than during the day (Wallace 1975).

Past studies indicate that the nocturnal enhancement of precipitation over the Midwest results from long-lived cells known as mesoscale convective complexes. So-called "MCC's" begin as isolated afternoon thunderstorms, and intensify into organized cells, sustaining intense rainfall for hours, or even days (Wallace 1975). Nocturnal convection associated with MCC development apparently occurs only over the Midwest, and not over other parts of North America, where afternoon air-mass thunderstorms tend to dissipate after dark. Current research suggests that MCC's

are fueled by a synoptic-scale southerly wind current over the Great Plains, known as the low-level jet (LLJ). This diurnally oscillating, lower tropospheric phenomenon supports MCC development by both transporting water vapor over the Great Plains (Helfand and Schubert 1995, Rasmusson 1967) and by creating low level convergence (Bleeker and Andre 1951, Pitchford and London 1962). Individual case studies (Means 1954, Bonner 1966) and climatological studies (e.g., Augustine and Caracena 1994, Helfand and Schubert 1995) have diagnosed many essential LLJ properties and have proposed several causes for its development.

1.2 Land and atmosphere hydrologic processes and the LLJ

Among the possible explanations for nocturnal LLJ formation, boundary-layer processes appear to play a decisive role. At the surface, incident solar radiation is partitioned between sensible and latent heating (according to the Bowen ratio), which in turn is dependent upon surface hydrologic conditions. The land surface temperature and near-surface atmospheric baroclinicity are therefore linked with surface water balance and atmospheric vapor transport processes. Conversely, the hydrology of the Great Plains is influenced by the LLJ, through precipitation resulting from northerly vapor transport. In light of the importance of the LLJ in the hydrology of the Midwest, this paper investigates the complex set of feedbacks governing LLJ frequency and intensity. A set of models are designed to mimic, and eventually extend the simple atmospheric mixed-layer model developed Kim and Entekhabi (1998) to a 2-D meridional domain. Subsequent chapters outline the results of this low-level jet study, and outline further improvements on modeling and diagnostic codes.

Chapter 2 details the climatology and proposed causal mechanisms of the LLJ based on existing literature. Past studies from rawindsonde and wind profile networks are discussed to detail the temporal variation, geographic location, vertical distribution, and other mean characteristics of the LLJ. Following this phenomological

survey, LLJ possible forcing mechanisms are reviewed.

Background model derivations and assumptions appear in Chapter 3, which also details significant changes made to model assumptions after a preliminary failure due to a spurious energetic instability. A sensitivity analysis is conducted on the modified wind profile to facilitate stable model execution.

Chapter 4 presents the results of prototype stand-alone codes and an initial implementation of Kim and Entekhabi's (1998) tendency equations. In particular, this chapter scrutinizes model output for energy feedbacks due to radiation, convergence, entrainment, and advection.

Chapter 5 reviews the conclusions reached from this modeling study, and sets forth suggestions for future research.

The appendices provide fully-detailed derivations of the geostrophic shear and Ekman spiral solutions referenced in the text.

Chapter 2

Literature Review

2.1 Low-level jet climatology

2.1.1 Case studies and observational characteristics

In past literature, the term "low-level jet" or "low-level jet streak" has referred to a lower tropospheric wind current which achieves a certain threshold wind maximum relative to the next highest minimum in the vertical profile. Low-level jets in general are observed in a wide array of meteorological regimes ranging from sea breeze circulations, to cold air damming, to mountain-valley systems (e.g. Blackadar 1957). In this paper, however, the term "low-level jet" or simply "LLJ" will refer to a narrowly defined class of supergeostrophic wind maxima which satisfy several requirements in its vertical profile, temporal variability, and frequency and directional distribution.

A series of early case studies defined what has come to be uniquely known as the Midwest low-level jet. This wind regime is a major source of water vapor transport to the U.S. Great Plains and it plays an important role in the hydrology of the region. Means (1954) presents one of the first quantitative studies of a nocturnal southerly jet which was nearly exclusively responsible for causing the Kansas City floods July 10-12, 1951. In an early rawinsonde study, Blackadar (1957) links the LLJ with the development of the nocturnal inversion. Gerhardt (1962) uses observation

tower measurements to establish a vertical/temporal characterization of the southerly jet. He found that this wind maximum reached a peak speed shortly before dawn, and then decayed after sunrise, when adiabatic conditions had reached the level of highest wind speed. Using the same "Texas tower" at Cedar Hill, TX, Izumi and Barad (1963) more fully outlined the temporal development of a low-level jet; the temporal momentum peaks at the level of maximum speed lagged that of layers lying below, suggesting that LLJ formation actually begins at the surface and propagates into the overlying nocturnal inversion. In a similar study, Izumi (1964) verified that intensified turbulence at sunrise begins at the surface and propagates into the vestigial nocturnal temperature profile, and eventually dissipates the LLJ through adiabatic motions, corroborating Gerhardt's result.

The horizontal structure of the LLJ was analyzed by Hoecker (1963), who showed that the southerly low-level jet showed marked spatial coherence and supergeostrophic velocities during the nighttime, while being largely incoherent and subgeostrophic during daytime hours. Hoecker (1963) also first identified the term "low-level jet" as a boundary layer-induced phenomenon, as opposed to those jets resulting from the inertia of an upper tropospheric jet. Bonner (1966) also elaborated on the spatial characteristics of the LLJ in relation to thunderstorm development, and concluded that thunderstorm velocity at night was caused by broad areas of positive vertical velocity induced by LLJ convergence. He also noted that temperature and moisture advection by the LLJ were not enough to sustain thunderstorm development after dark, but might help to start local convection. Mahrt (1977) also correlates dynamical forcing from the LLJ in producing severe thunderstorms over the Great Plains.

The observation tools (primarily twice–daily rawinsondes in a sparse network) available for the study of the localized LLJ were extremely limited, both spatially and temporally, until recent decades and the advent of wind profiler instrumentation. As a result, more recent remote sensing-based studies have revealed much about LLJ structure. An airborne radar altimetry study by Parish et al. (1988) identified several forcing mechanisms (to be discussed in a later section) and reinforced past conceptions about LLJ evolution with far more reliable characterization. Previous

rawinsonde studies often missed peak wind speeds because the low-level jet might complete a cycle of growth and decay between the scheduled balloon launches. A state-of-the-art wind profiler network over the Great Plains facilitated a survey of another low-level jet scenario by Zhong et al. (1996) Like previous studies, Zhong et al. (1996) cites the nearly constant southerly/southwesterly directionality of the LLJ, and also the vast range in wind speeds across the diurnal cycle.

2.1.2 Vertical profile classification criteria

In addition to isolated case studies, climatological studies have delineated various criteria which have proven useful in LLJ classification and analysis. Blackadar (1957) differentiates between *significant* and *insignificant* wind maxima in a given vertical profile. Significant wind maxima are those maxima lying below 1.52 km (5000 ft) and whose wind speed exceeds the next highest minimum by 2.57 m s^{-1} (5 kts). A more elaborate scheme is presented in Bonner (1968), which sets the vertical cutoff at 2.5 km and categorizes the low-level jets among three speed criteria. Criterion 1, 2, or 3 jets must exceed 12, 16, or 20 m s^{-1} respectively, and must decrease by 6, 8, or 10 m s^{-1} to the next highest minimum or 3 km level. Whiteman et al. (1997) adds an additional "criterion 0" low-level jet which corresponds to a wind maximum exceeding 10 m s^{-1} with a falloff criterion of 5 m s^{-1}.

2.1.3 Spatial frequency and directionality distribution

The LLJ criteria posed by Bonner (1968) and Whiteman et al. (1997) are used in both papers to establish geographic patterns of the frequency and distribution of the LLJ. Bonner (1968) reports a maximum in the frequency Criteria 1-3 low-level jets over Oklahoma and southern Kansas, with less pronounced maxima over the east coast and South Dakota, however these local effects do not remain in Criteria 2-3 analysis.

Bonner (1968) determined an axis of maximum LLJ activity along a curve stretching from roughly 30 to 45 degrees north latitude, between 100 and 95 degrees west longitude. From this analysis, Bonner (1968) concludes that LLJ activity tends

to appear in the 0600 LST sounding than 1800 LST, tends to have a much more pronounced diurnal cycle in the summer, and is preferentially an early morning phenomenon at locations away from the Gulf Coast or Great Lakes. The paper also showed that near bodies of water, the frequency of morning jets as opposed to evening jets is less pronounced.

2.1.4 Mean horizontal structure

Bonner (1968) describes the horizontal structure of the low-level jet according to a relative coordinate system centered along the mean jet axis in radiosonde observations. This axis extends roughly north-south along a line from Midland, TX to between Bismark, ND and St. Cloud, MN. The normal direction to this coordinate system then extends roughly east-west from the jet axis. Bonner (1968) then plotted the observations on this modified natural coordinate frame to simplistically model the LLJ mean isotachs. After averaging the velocities at 28 stations, Bonner (1968) showed the climatological center of the LLJ axis to lie directly over Topeka, KS. Interestingly, Bonner (1968) also notes that an apparent (though here unexplained) limit to the low-level jet magnitude of about 28.27 m s^{-1} (55 kts), and draws upon anecdotal evidence to support this claim.

2.1.5 LLJ contribution to N. American water vapor budget

Rasmusson (1967) proposed the importance of diurnally varying winds upon the water vapor budget in a control volume over North America. The paper identifies that south of 50 degrees N, the summertime diurnal cycle influences the vapor transport across not only the Great Plains but also over parts of Mexico and Central America. Helfand and Schubert (1995) elaborate upon this finding through an atmospheric general circulation model (GEOS-1 AGCM) simulation which determined the relative contribution of the moisture-laden LLJ to the water vapor budget of the North American continent, and particularly over the Great Plains. They point out that much of the Pacific moisture in zonal flow never reaches the interior Great Plains,

anticyclonic circulation west of the Rockies which parallels, rather than intersecting the western boundary of the United States.

The LLJ, on the other hand, strongly influences the mean and transient vapor fluxes, and the resulting continental hydrology of the U.S. Great Plains. Helfand and Schubert (1995) compute the simulated vapor fluxes according to three discrete layers: surface to 850 hPa, 850-550 hPa, and 550-10 hPa. It is shown that not only does the southerly flow at the lowest level produce the majority of vapor flux into the United States, but the LLJ alone (a smaller "window" of the lowest layer) is responsible for about a third of the water vapor transport. Helfand and Schubert (1995) also discovered that there was a net divergence in the model vapor flux field over the continental United States, with evaporation supplying the net deficit in water vapor. The great role of the LLJ in transporting moisture into North America provides ample justification in discovering its physical mechanisms and establishing predictive/diagnostic tools for LLJ study, particularly with regard to its role in the hydrologic balance of North America.

2.2 Proposed low-level jet forcing mechanisms

2.2.1 Survey of early hypotheses

As one of the first serious studies of LLJ mechanisms, Bleeker and Andre (1951) proposed that the large scale convergence associated with the LLJ over the Midwest was due to local orographic circulations. Air sinking at night from the west slope of the Appalachians and the east slope of the Rockies creates a buildup of air over the Midwest, and hence produces low-level convergence and vertical motion. Indeed, according to Bleeker and Andre, the LLJ was forced merely as a secondary effect of this synoptic-scale mountain-valley circulation. In contrast, (Blackadar 1957) linked the LLJ directly with local boundary layer behavior. He claimed that the diurnal cycle of surface heating and cooling create variable eddy viscosity coefficients which in turn creates a nocturnal maximum in southerly wind flow. This study approximates

qualitative behavior found in climatological results, but fails to reproduce the strongly supergeostrophic magnitudes of the LLJ. Wexler (1961) proposes that the nocturnal frictional decoupling in Blackadar's model does not really force the LLJ, but rather allows the orographically deflected large scale flow associated with the Bermuda High to build down toward the surface. Though shown later not to be the dominant forcing in the Midwest LLJ, a later paper by Paegle et al. (1984) emphasizes this deflection effect in a similar low-level wind maximum monitored during ALPEX. (This hypothesis is analogous to the western boundary deflection of the Gulf Stream.) Holton (1967) models the "air drainage" theory in Bleeker and Andre (1951) according to a constant eddy viscosity Ekman spiral coupled with thermal effects.

2.2.2 Boundary layer effects on the LLJ

A numerical study by Wipperman (1973) outlines the effects of boundary layer stability, baroclinicity, and non-stationarity upon the LLJ. Wipperman (1973) found that a very stable boundary layer, regions of strong baroclinicity, and increasing non-stationarity in the boundary layer favor strengthening in the LLJ wind maximum. Zeman (1979) constructed a slab model of the boundary layer and found that the primary forcings of the LLJ in the model were the rate of surface cooling at sunset and the baroclinicity. McNider and Pielke (1981) modeled the low-level jet according to a one-dimensional ABL prognostic model coupled with the surface energy budget. Their study highlighted the effect of the thermal wind upon local flow. During the daytime, the thermal wind is in general northward over the Midwest, but reverses direction in the evening. (McNider and Pielke 1981) were able to show that the supergeostrophic wind maximum was caused by mesoscale thermal wind effects modified by frictional turning at the no-slip lower boundary. Parish et al. (1988) also points to the frictional decoupling and isallobaric contributions as forcing the LLJ.

Paegle and McLawhorn (1983) determined the LLJ flow over a complex terrain with detailed vertical structure. The model showed that convergence calculations were most dependent upon soil type, with the thermal conductivity the most important soil attribute. Soil type and soil moisture played a large role in this thermal forcing:

dry sand had the smallest thermal inertia, heated the boundary layer more, and produced a convergence pattern with greater magnitude, as opposed to clay and silt, which showed a higher thermal inertia. This paper also outlined LLJ model sensitivities to longwave radiation divergence and absolute rotation rate (latitude). McCorcle (1988) extends this model to include not only sensible heat flux but also allows the soil moisture to partition into latent fluxes at the surface. Because soil moisture plays an important role in the energy transfer at the surface, and since the low-level jet is a nocturnal boundary layer phenomenon, one would expect the LLJ to exhibit a degree of sensitivity to surface energy and moisture budgets. McCorcle (1988) imbeds a surface hydrology model into a tropospheric forecast model to test the LLJ for sensitivity to uniform magnitudes of soil saturation as well as heterogeneous moisture distributions. It was shown that saturated soil substantially reduced the LLJ magnitude, because of the decrease in diurnal temperature range. Wet soil over the Great Plains and dry soil over the Rockies strengthened the jet, while the converse was true for dry Plains and moist Rockies. Zhong et al. (1996) corroborates this finding in a wind-profiler case study, in which it is found that increasing latitude enhances the jet, and more importantly, that drier soils amplify the diurnal LLJ cycle. Wetter soils were found to damp this oscillation, but enhanced downstream convection through increased latent heat release.

2.2.3 A two-dimensional LLJ model

By taking a 2-D version of McCorcle (1988), Fast and McCorcle (1990) are able to more easily resolve the precise *surface* forcing mechanisms, as opposed those caused by to complex 3-D geometries and other synoptic-scale effects. A sensitivity analysis is conducted for three surface properties: slope, latitude, soil type, and soil moisture. Fast and McCorcle (1990) found that the low-level jet was most strongly influenced by the soil moisture and slope of the terrain. Changes in soil moisture caused even a greater response than in McCorcle (1988) but showed similar qualitative trends. Over flat (zero slope) terrain, the LLJ was substantially limited and failed to match observations. The addition of slope created a much closer approximation to observed

LLJ characteristics. Fast and McCorcle showed that latitude not only affected the magnitude of the jet, but also the time of LLJ onset. Model results indicated that points farther north were found to have a more intense LLJ, and an earlier onset of the jet. Uniform soil moisture variations caused substantial decreases in the LLJ magnitude, and heterogeneous changes to soil moisture also affected the jet in a similar fashion as McCorcle (1988). In this thesis, a similar model is used to investigate the sensitivities of the Midwest LLJ. Past models by Fast and McCorcle (1990) and McCorcle (1988) use soil moisture to partition radiative energy into sensible and latent surface fluxes. However, other studies have suggested the importance of local pressure gradients as well. e.g. (Zhong et al. 1996) As a result, simply decoupling the friction of the surface and allowing higher velocities to build does not speak of the entire physical process. In addition to surface effects creating frictional decoupling, they might also create local baroclinicity which influences not just the decoupling but also might significantly influence the geostrophic wind itself through thermal wind relationships, as supported by McNider and Pielke (1981) and others. Likewise, McNider and Pielke (1981) did not include the effects of soil moisture explicitly, which would strongly influence their thermal wind parameterization.

In addition,the Fast and McCorcle (1990) model neglects advection, and assumes that there are gradients only in the x and z direction. However, advection might play a great role in LLJ flow, particularly in energy and vapor fluxes. These fluxes are certainly non-trivial to low-level jet formation, (Rasmusson 1967, Helfand and Schubert 1995) and might play a large role in modifying the simplistic radiative energy partitioning in previous models. A complex set of possible feedback mechanisms develops as the advective and thermal wind effects are taken into account. For example, the latitudinal variation of time of LLJ onset might be an artifact of Fast and McCorcle's (1990) neglect of advection, which could equalize the surface gradients and cause a more uniform onset time. Past observational evidence supports a LLJ onset at sunset, and is apparently not dependent upon latitude. More important than the timing, the magnitude and vertical profile of the LLJ may also be impacted by thermal wind and advective properties, but these effects have not appeared together

in a single modelling study.

In light of the state of LLJ research, the forcings investigated by Fast and McCorcle (1990) form the starting point of investigation for this thesis, with additional attention given to advective effects as well as thermal wind variation of the geostrophic wind. A two dimensional model is utilized similar to that used in Fast and McCorcle (1990), but has a parameterized meridional flux component and a more crude hydrologic parameterization (bucket model with no vegetation canopy). The two dimensional character of the model is retained to facilitate narrow study of local boundary effects as opposed to mountain/valley drainage and other zonally varying effects. The balance of this thesis discusses the implementation and outcome of a thermal wind modified Ekman spiral and spatial coupling of model fluxes.

Chapter 3

Model assumptions and implementation

3.1 Spatial extent and resolution of model

In order to study the forcing of soil moisture upon low-level jet development, a model was developed in this thesis similar to the two-dimensional setup in McCorcle (1988). It is assumed in this paper that zonal effects (such as draining from the Rockies and Appalachians) are not linked with soil moisture and other boundary layer sensitivities, permitting a more isolated study of the LLJ phenomenon. The model is arranged as a meridional line of boxes, with the axis of the LLJ assumed to be only meridional, for simplicity. The actual mean LLJ axis in Bonner (1968) consists of a broad curve over the southern U.S., but this curvilinear pattern is ignored. The entire meridional domain stretches 1000 km, beginning at 26 deg N and extending northward along the LLJ mean axis to 35 deg N latitude. The boxes themselves are variable in height, depending upon the temporally and spatially variable mixed layer height. The resolution of the model was determined by stability constraints imposed by the number of timesteps feasible in a reasonably short numerical simulation. A resolution of 31.25 km was used for the grid box horizontal spacing. The vertical resolution of the wind between cells was 2000 grid points for the vertical range of the mixed layer, which was overlaid with the free atmosphere. Fig. 3-1 shows a schematic diagram of

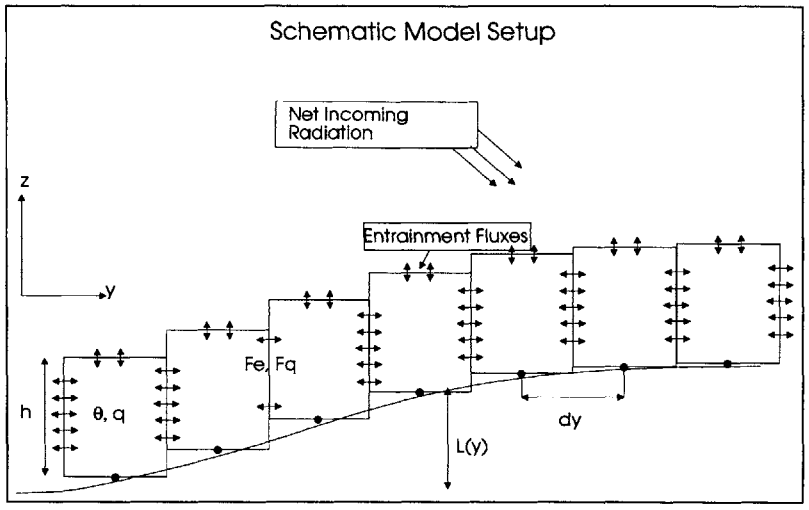

Figure 3-1: A schematic diagram of the meridional box model. An offline 0-D model solves the moisture and radiative energy balance equations at each point in the meridional domain. The boundary layer height, h, is parameterized at each point according to local atmospheric and surface energy balances. The atmosphere confined to the mixed layer is assumed to have a vertically uniform characteristic potential temperature and specific humidity. The soil maintains its own temperature, with soil moisture included. Interaction between the points occurs due to meridional advection from the ageostrophic wind, which is dependent upon a background zonal geostrophic wind and surface potential temperature gradients caused by differential heating and spatial soil moisture variations. The model accounts for topography by parameterizing a vertical velocity in the boundary layer model based upon the slope of the no flux surface, but this effect was not included due to project time limitations. External fluxes enter the system by way of entrainment of dry air at the top of the boundary layer and through radiative transfer.

the model design.

3.2 ABL variables, assumptions, and constraints

At each cell in the model, time evolution of atmospheric state variables is influenced by both communication with neighboring cells (via the parameterized wind field) and through the boundary layer phenomena modeled in the land-surface 0-D model. Assuming a well-mixed boundary layer, the potential temperature and specific humidity are assumed to be constant both horizontally and vertically within each cell. In the horizontal domain, meridional baroclinicity is allowed in terms of the

calculated gradients in the temperature and moisture fields. For this thesis, the density used for calculating the meridional fluxes in each cell is invariant with height, and each cell obeys mass conservation as flow passes in and out of the cell. Air can enter and exit the top and sides of the box. The dry atmosphere is assumed to obey the ideal gas law and hydrostatic assumption, with no vertical acceleration except during the parameterized boundary layer collapse. The overlying atmosphere interacts with the boundary layer only through the entrainment of dry air aloft, and through the parameterized geostrophic wind, which determines the Ekman deflected winds in the mixed layer.

3.3 Summary of boundary layer model and modifications

The boundary layer model utilized in this thesis is taken directly from (Kim and Entekhabi 1998) and simulates the surface energy and vapor budget and the planetary boundary layer, based upon the tendency equations for soil temperature, potential temperature, specific humidity, and the growth and collapse of the PBL. Surface energy and vapor transfers occur through turbulent sensible fluxes, latent heat fluxes, and terrestrial and solar radiation. The model consists of two slabs: the top layer of soil, with a characteristic thermal depth, and the atmospheric mixed layer, with a corresponding upper limit. The mixed layer is bounded aloft by a jump discontinuity in both the entropy and humidity fields, governed by specified lapse rates above the inversion and is no higher than the lifted condensation level at the top of the boundary layer (PBL). The soil slab is characterized by a uniform surface temperature value, as well as a pore saturation value. The soil hydrology is simulated according to a simple bucket model, with a depth scale arbitrarily set to create the desired thermal inertia properties of the soil, when heated and cooled during the diurnal cycle.

Besides accounting for the surface energy and moisture budgets, the offline 0-D model from Kim and Entekhabi (1998) must also accommodate terms for meridional

transport and parameterized large-scale vertical velocity. What follows is a summary of the tendency equations with their respective modifications for the LLJ 2-D model. The reader is urged to consult Kim and Entekhabi (1998) for more detailed information about model development and parameter sensitivity in the 0-D case. The original soil temperature, potential temperature, and specific humidity tendency equations are given by:

$$z_t C_s \frac{\partial T_s}{\partial t} = R_s (1 - a) + [R_{rad} (1 - \epsilon_a) + R_{sd}] \epsilon_s - R_{gu} - H - \lambda E \tag{3.1}$$

$$\rho c_p h \frac{\partial \theta}{\partial t} = [R_{ad} + R_{gu} + (R_{ad} (1 - \epsilon_a) + R_{sd}) (1 - \epsilon_s)] \epsilon_a - R_{sd} - R_{su} + H + H_{top} \tag{3.2}$$

$$\rho h \frac{\partial q}{\partial t} = E + E_{top} \tag{3.3}$$

The forcing in (3.1) consists of the absorbed shortwave radiation, incoming and outgoing longwave fluxes, and surface sensible and latent heat fluxes. The potential temperature in (3.2) is affected radiatively by longwave fluxes absorbed by atmosphere from the surface, the mixed layer itself, and from above the mixed layer. In addition, the mixed layer is heated from above through the entrainment of sensible heat fluxes, and from below in the surface sensible heat flux. Finally, the specific humidity in the zero-dimensional case is affected by incorporation of moisture from the earth's surface, and net losses to the free atmosphere through the entrainment of overlying dry air.

The mixed layer height responds to the heating and cooling during the diurnal cycle, and is parameterized according to a tendency equation given by

$$\frac{dh}{dt} = \frac{2 (G_* - D_1 - \delta D_2) \theta}{g h \delta_\theta} + \frac{H_\nu}{\rho c_p \delta_\theta} \tag{3.4}$$

While significant detail is omitted about the various technical variable definitions, it will be noted that the first term in (3.4) corresponds to mixed layer growth from mechanically generated turbulence, while the second term represents that growth due to sensible heat flux at the surface. During the daily collapse of the PBL, the height

is explicitly parameterized according to Smeda (1979).

$$h = -\frac{2\left(G_* - D_1\right)\rho c_p \theta}{H_\nu g} \tag{3.5}$$

During boundary layer collapse, the mixed layer height tendency is set to zero, and (3.5) has sole control until the nocturnal inversion stabilizes. In order to extend the 0-D tendency equations encompass the additional spatial effects in a 2-D LLJ model, four changes are made to the model equations. First, the atmospheric potential temperature, moisture, and soil temperature tendency equations are modified to include additional terms due to meridional transport. Second, the large-scale vertical velocity (created by topographic changes and mass convergence) is included into the entrainment flux and inversion strength equations and mixed layer height tendency equation. Third, the entrainment fluxes and inversion strength tendency equations must be modified to allow for nonzero fluxes at the top of the boundary layer during periods of collapse, in order to maintain mass conservation. Finally, the frictional velocity must be changed to accommodate the computed lateral winds, which are calculated according to the formulation in a previous section. This in turn creates a change in the aerodynamic resistance and hence the sensible and latent heat fluxes at the surface must be modified. This change simply involved adding a variable for the frictional velocity which varied according to screen-height winds, as opposed to the constant parameter in the 0D model, and will not be described in further detail. It might appear that the presence of a large scale vertical velocity would enhance the surface fluxes in addition to variation in the frictional velocity. However, because the large scale vertical velocity is the integrated meridional wind convergence at any given point, its value close to the surface is very small, and its effects on the surface fluxes will be ignored.

3.3.1 Meridional transport of energy and vapor

Assuming that the soil temperature in cell i has no effect on the soil temperature of neighboring cells (due to the low heat conductivity of the ground) (3.1) remains

unchanged, and is simply computed independently as if it were acting in the 0-D case. The potential temperature, however, does have a dependency upon meridional transport. Tendency equation (3.2) is therefore adjusted by adding a term for the local net meridional energy flux, F_e^{net} which is computed from the winds in the ith and $(i-1)$th cells and integrated from the surface to the top of the mixed layer. See subsequent sections for wind and flux calculations. The modified form of (3.2) becomes

$$\rho c_p h \frac{\partial \theta}{\partial t} = \left[R_{ad} + R_{gu} + \left(R_{ad}\left(1-\epsilon_a\right) + R_{sd}\right)\left(1-\epsilon_s\right)\right]\epsilon_a - R_{sd} - R_{su} + H + H_{top} + F_e^{net} \tag{3.6}$$

where F_e^{net} is in units of W m^{-2}. In a similar manner, the vapor tendency equation can also be modified to include the effects of meridional transport. The net meridional flux of moisture into the cell is denoted as F_q^{net} in units of kg s^{-1} m^2. So the new moisture tendency equation becomes

$$\rho h \frac{\partial q}{\partial t} = E + E_{top} + F_q^{net} \tag{3.7}$$

Both of these tendency equations are provided values from the offline model, which in turn yields respective time increments of each variable.

3.3.2 Effects from large-scale vertical velocity

To compensate for large scale vertical velocity at the top of the boundary layer, the energy and moisture entrainment terms (H_{top} in (3.6) and E_{top} in (3.7)) require an additional component to allow air to enter and exit the top of the cell. The original expressions for the sensible and latent heat entrainment are given by

$$H_{top} = \rho c_p \delta_\theta \frac{\partial h}{\partial t} \tag{3.8}$$

$$E_{top} = \rho \delta_q \frac{\partial h}{\partial t} \tag{3.9}$$

Let w_{top}^{LS} be the large scale vertical wind velocity at the top of the mixed layer, which is calculated in the meridional model. Then, the new composite entrainment fluxes are given by

$$H_{top}^{*} = \rho c_p \delta_\theta \left(\frac{\partial h}{\partial t} + w_{top}^{LS} \right) \tag{3.10}$$

$$E_{top}^{*} = \rho \delta_q \left(\frac{\partial h}{\partial t} + w_{top}^{LS} \right) \tag{3.11}$$

Thus, entrainment can now be induced through boundary layer growth and collapse or through input and output at the otherwise stationary mixed layer top. The tendency equations for the inversion strengths also must be adjusted for the additional vertical velocity. The original tendency equations are given by

$$\frac{\partial \delta_\theta}{\partial t} = \gamma_\theta \frac{\partial h}{\partial t} - \frac{\partial \theta}{\partial t} \tag{3.12}$$

$$\frac{\partial \delta_q}{\partial t} = \gamma_q \frac{\partial h}{\partial t} - \frac{\partial q}{\partial t} \tag{3.13}$$

Along the lines of (3.10) and (3.11), the new inversion tendency equations become

$$\frac{\partial \delta_\theta}{\partial t} = \gamma_\theta \left(\frac{\partial h}{\partial t} + w_{top}^{LS} \right) - \frac{\partial \theta}{\partial t} \tag{3.14}$$

$$\frac{\partial \delta_q}{\partial t} = \gamma_q \left(\frac{\partial h}{\partial t} + w_{top}^{LS} \right) - \frac{\partial q}{\partial t} \tag{3.15}$$

Physically, these equations now allow for vertical velocity to influence the inversion strength by mixing down the free atmosphere lapse rates. Finally, the parameterized growth of the mixed layer is adjusted to compensate for the large scale vertical velocity:

$$\left.\frac{dh}{dt}\right|_{new} = \left.\frac{dh}{dt}\right|_{old} + w_{top}^{LS} = \frac{2\left(G_* - D_1 - \delta D_2\right)\theta}{gh\delta_\theta} + \frac{H_\nu}{\rho c_p \delta_\theta} + w_{top}^{LS} \tag{3.16}$$

Note that the $\frac{dh}{dt}$ terms in (3.10), (3.11), (3.14), and (3.15) are given by $\left.\frac{dh}{dt}\right|_{old}$. This formulation was used for compatibility with the parameterized collapse of the boundary layer, in which the mixed layer height tendency term is set to zero, while

the entrainment and inversion strength equations are allowed to be nonzero. As the atmospheric boundary layer collapses, the mass needs to "escape" the model and avoid excessive heat buildup. In the 0-D model, these terms are all trivial when the boundary layer collapse occurs, but must be nonzero in the 2-D case to obey mass conservation.

3.4 Derivation of meridional winds

3.4.1 Assumptions of parameterized flow

In the two-dimensional model developed for this thesis, a low-level wind profile was desired which would include the effects of friction upon a background, zonal, and predominantly geostrophic wind. For the purposes of LLJ investigation, such boundary layer flow is best modeled by an Ekman spiral approximation. According to Holton (1992), the Ekman spiral solution assumes a "horizontally homogeneous turbulence above a viscous sublayer," and furthermore makes the flux gradient approximation upon the resulting Navier-Stokes equations in two dimensions. A classic Ekman spiral (hereafter denoted "Profile I") assumes a constant diffusivity with respect to height, and also holds the "background" geostrophic wind as an altitude-invariant quantity. While this wind regime allows the wind to depart from geostrophic values, it does so only through changes to the momentum diffusivity and latitude. Appendix B provides a full derivation and explanation of the Profile I Ekman spiral.

The goal of this project, however, was to allow the wind field to change as a result of temperature and moisture gradients arising from differential heating and surface energy partitioning across a meridional domain. Various Ekman spiral variations are documented in the current literature. Singh et al. (1993) uses a crude temporal variation of the momentum diffusivity to mimic the frictional decoupling after sunset. This parameterization alone is unsuitable for the model because it fails to take into account the effect of spatial gradients upon the wind field. In Holton (1967), an

analytic solution of the momentum equation allows a meridional geostrophic wind to respond to zonal temperature gradients, with topographic variation. Mahrt and Schwerdtfeger (1970) uses an exponential thermal wind structure which allows spatial variability, in their case, due to topographic changes over the Antarctic Plataeu. The exponential thermal wind structure in their paper, however, requires more information than available in the model used for this project; i.e., the potential temperature gradient is height invariant, so the shear term derived from local temperature gradients (via the thermal wind equation) must also be constant with respect to height, whereas in Mahrt and Schwerdtfeger (1970) the shear term changes continuously with altitude.

3.4.2 General description of Profile II

In this paper, a new wind profile was derived which exhibited reasonable sensitivities to available atmospheric parameters. Appendix B shows a fully detailed mathematical derivation of the Ekman profile, beginning with the simplest Profile I (height invariant geostrophic wind deflected by a constant K_m). However, since the shear of Profile I is zero, the resulting Ekman spiral solution exhibits no variability with respect to temperature gradients, and is thus unsuitable for the model. The simplest solution background geostrophic wind which exhibits sensitivity to potential temperature gradients is a constant shear model, which will be denoted "Profile II." Profile II assumes a fixed value of U_{g*} at height z_*, and constant (non-trivial) shear with respect to height. Its explicit formulation is given by

$$u_g = U_{g*} + m_* (z - z_*) \tag{3.17}$$

The extrapolation fixed point, z_* is simply an arbitrarily defined constant based upon the desired characteristics of the profile. The slope, m_*, is allowed to vary in response to local temperature gradients according to the thermal wind relationship, and is derived in Appendix A. The final form of the shear term which is used for this model

is

$$\left.\frac{\partial u_g}{\partial z}\right|_{z=z_*} = m_* = -\frac{U_{g*}\Gamma_d}{\theta - \Gamma_d z_*} - \frac{g}{f\left(\theta - \Gamma_d z_*\right)}\frac{\partial \theta}{\partial y} \tag{3.18}$$

where g is the acceleration of gravity, Γ_d is the dry adiabatic lapse rate, θ is the potential temperature, and $\frac{\partial \theta}{\partial y}$ is the local meridional potential temperature gradient. In order to test the wind profile in (3.17) for feasibility in the meridional model, z_* was assigned the value of the mixed layer height, h, which is also the vertical limit of interaction between model cells. After making the substitution $z_* = h$, the analytic expression for the Profile II zonal geostrophic wind becomes,

$$u_g \approx u_g|_{z=h} + \left(\left.\frac{\partial u_g}{\partial z}\right|_{z=h}\right)(z-h) = U_{gh} + m_h\,(z-h) \tag{3.19}$$

where the geostrophic wind at the top of the mixed layer is given by U_{gh}. In the presence of a no-slip boundary condition, the total wind field associated with the Ekman spiral solution exhibits the deflection of the background flow,

$$U = \left(U_{gh} + m_h\,(z-h)\right)\left(1 - e^{-\gamma\left(z-z_{sfc}\right)}\cos\gamma\,(z-z_{sfc})\right) \tag{3.20}$$

$$V = \left(U_{gh} + m_h\,(z-h)\right)e^{-\gamma\left(z-z_{sfc}\right)}\sin\gamma\,(z-z_{sfc}) \tag{3.21}$$

where $\gamma = \sqrt{\frac{f}{2K_m}}$, K_m is the eddy viscosity, f is the Coriolis parameter. A full derivation of the Ekman solution for the Profile II case is described in Appendix B.

3.4.3 Feasibility analysis of Profile II

The desired meridional profile for use in this model was required to have the property that zonal winds aloft would respond positively to increasingly negative baroclinicity, as one would expect over a continental, midlatitude regime. The selection of the fixed point in Profile II determines whether the linear model fits this feasibility criterion for the meridional model. The sensitivity of the zonal geostrophic wind with respect to potential temperature gradients is shown in Fig. 3-2. In this figure, it is apparent that at altitudes below and above the fixed point, opposing trends exist. Above the

fixed point, increasing atmospheric baroclinicity (more negative $\frac{\partial\theta}{\partial y}$) yields increasingly positive geostrophic flow as would be desired under normal synoptic conditions. Below the fixed point, increasingly negative baroclinicity yields lighter winds. Trends in the Ekman-deflected meridional and zonal components reflect this result, with both the zonal and meridional wind speeds decreasing with negative baroclinicity, while the opposite is true above the fixed point, which in this case is the height of the mixed layer. The results of the sensitivity analysis for the zonal and meridional winds are plotted in Figs. 3-3 and 3-4.

Though responding favorably to baroclinicity in the zonal wind field, Profile II was still found to be untenable, due to its response to small-scale (truncation) errors in the computed temperature gradient field. From the meridional sensitivity plot in Fig. 3-5, a hypothetical potential temperature perturbation is sketched to show how such patterns amplify as a result of their convergence field. The instability was not ameliorated by smoothing algorithms, reductions in the time step (or coarser spatial resolution), nor by using a relaxation factor in the time-evolution equations. Indeed, from Figs. 3-5 and 3-4 it is apparent that one could eliminate the numerical instability by moving the fixed point to the surface, and causing a reversal in the mixed layer meridional flow sensitivity. Such a shift would also cause the zonal wind to be increasingly sensitive to local temperature gradients with respect to height, and violate the original zonal wind sensitivity constraint.

3.4.4 Profile III motivation and description

In light of Profile II diagnostics, a more complex Ekman spiral solution was sought for the meridional flow which would both eliminate model instability and allow realistic sensitivity of upper-level wind fields to baroclinic conditions. With Profile II, either the upper-level zonal flow to responded correctly but with the response to meridional temperature perturbations (with the fixed point at the top of the mixed layer), or had unrealistic zonal winds aloft with desired damping characteristics to local temperature gradients (by fixing z_* at the surface). Profile III solves this dilemma by strategically weighting two separate geostrophic components by their respective altitudes. Like the

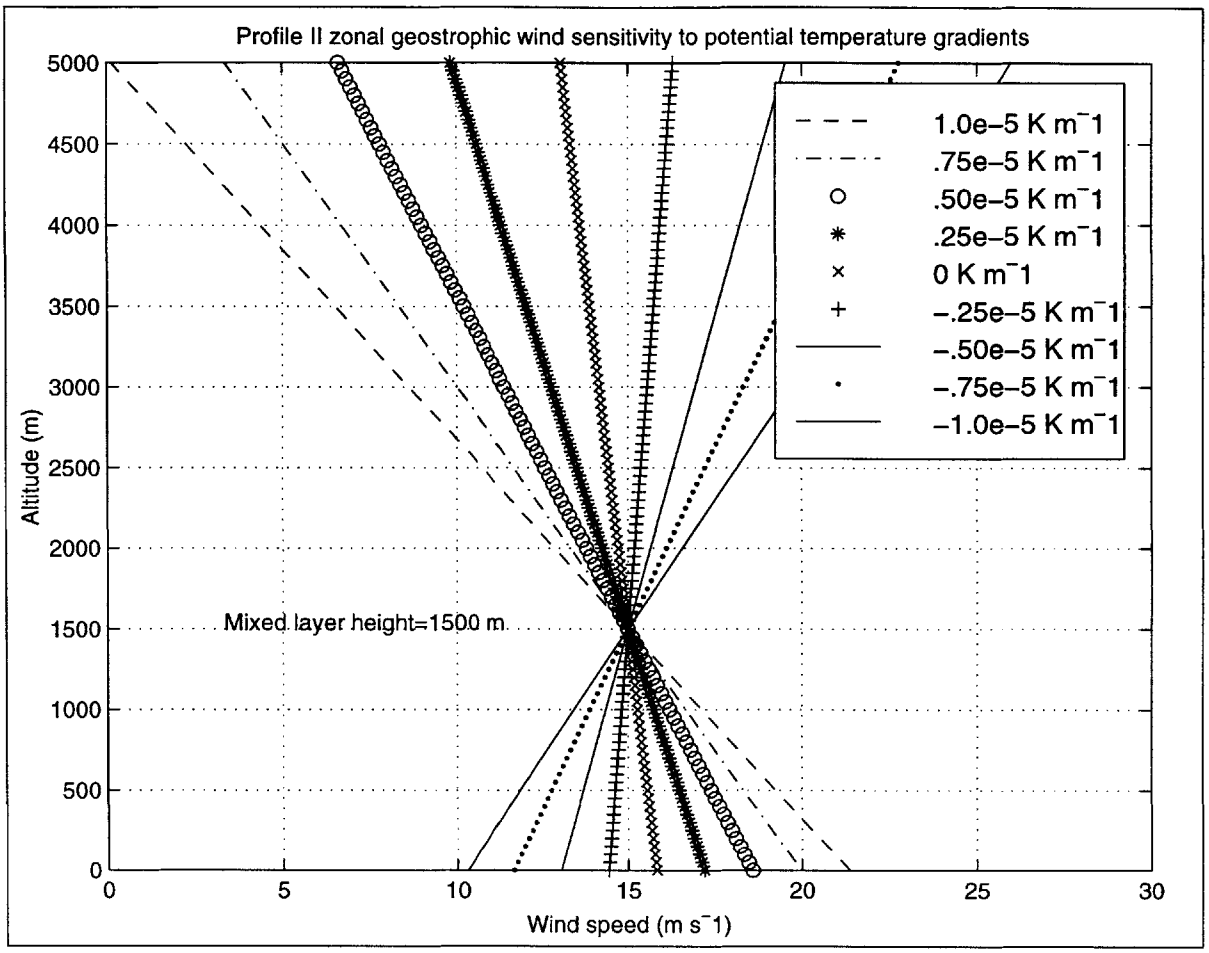

Figure 3-2: Linear profiles generated by varying the potential temperature gradient in (3.19). Here, $z_* = h = 1500$ m, $\theta = 280$ K and $f = 10^{-4}$ s^{-1}. Note that the extrapolation point is located at $z_* = h$; above the extrapolation point u_g increases as the potential temperature gradient becomes more negative, while at points below h the opposite trend is evident.

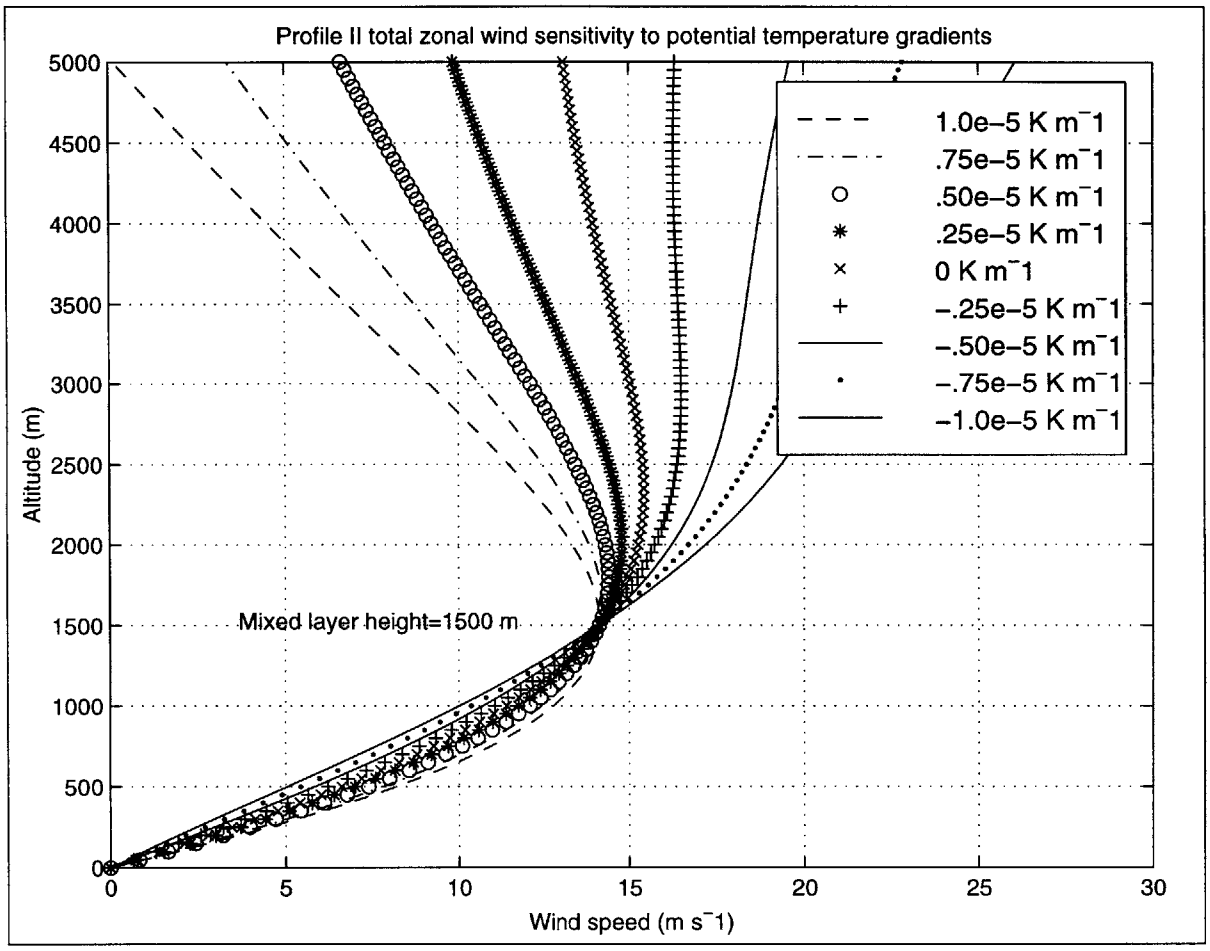

Figure 3-3: The Profile II Ekman spiral zonal wind profiles generated by varying the potential temperature gradient in (3.19). Here, $z_* = h = 1500$ m, $\theta = 280$ K and $f = 10^{-4}$ s^{-1}, and the depth of the Ekman layer is 3500 m. Below the fixed point, increasing baroclinicity results in a slight decrease in the net wind speed, while above the mixed layer, the zonal wind becomes dominated by the linear shear term as the Ekman spiral solution approaches the geostrophic wind with increasing altitude.

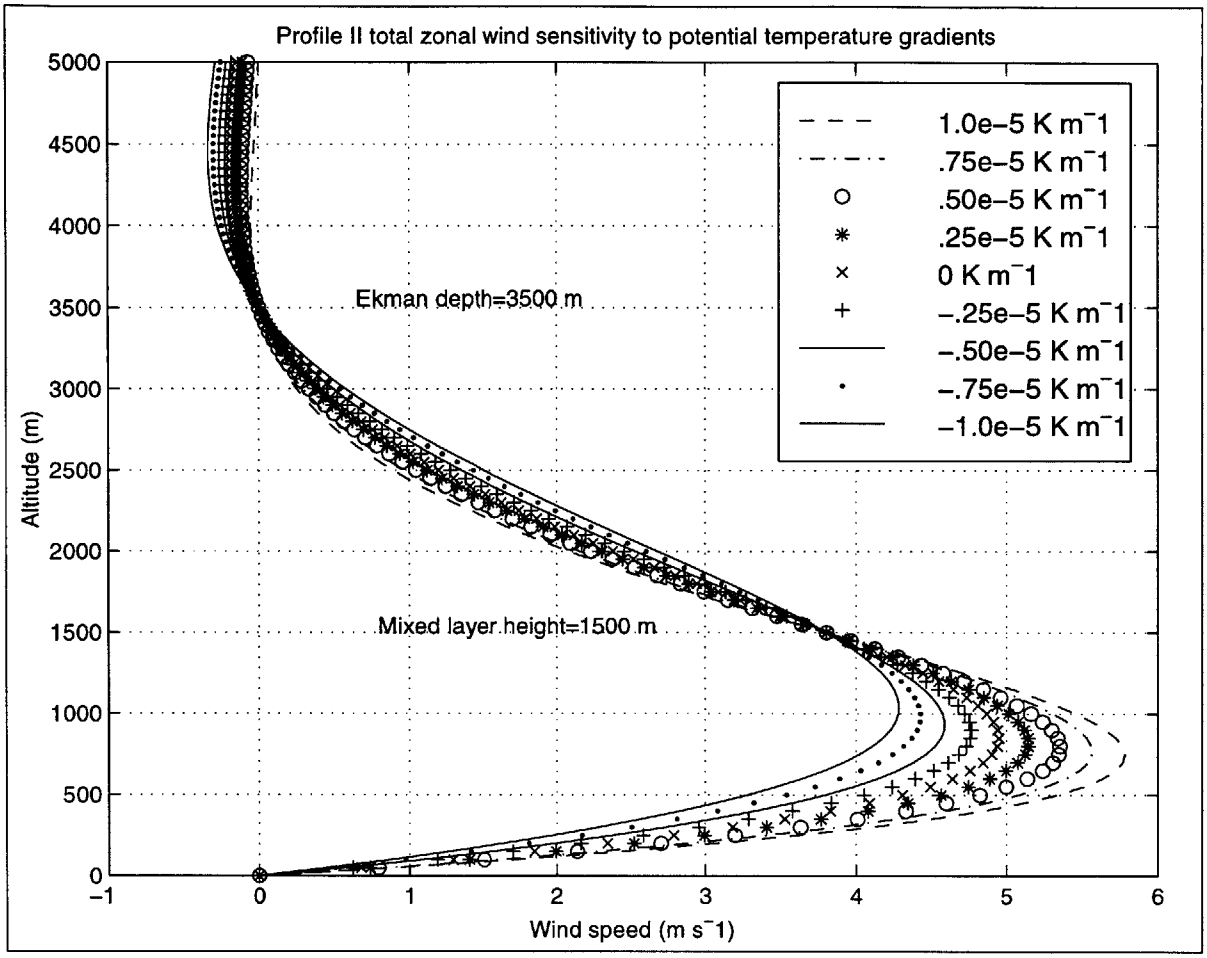

Figure 3-4: Resulting meridional wind profiles from changing the potential temperature gradient in (3.19). Here, $z_* = h = 1500$ m, $\theta = 280$ K and $f = 10^{-4}$ s^{-1} and the depth of the Ekman layer is 3500 m. As in the zonal wind, the meridional wind is invariant at the height $z = h$, due to the fixed point in the extrapolated geostrophic wind profile. A second fixed point is located at $z = 3500$ m, since the meridional wind speed is exactly zero at the top of the Ekman layer, by definition. Within the mixed layer, increasingly positive baroclinicity results in decreasing wind speeds.

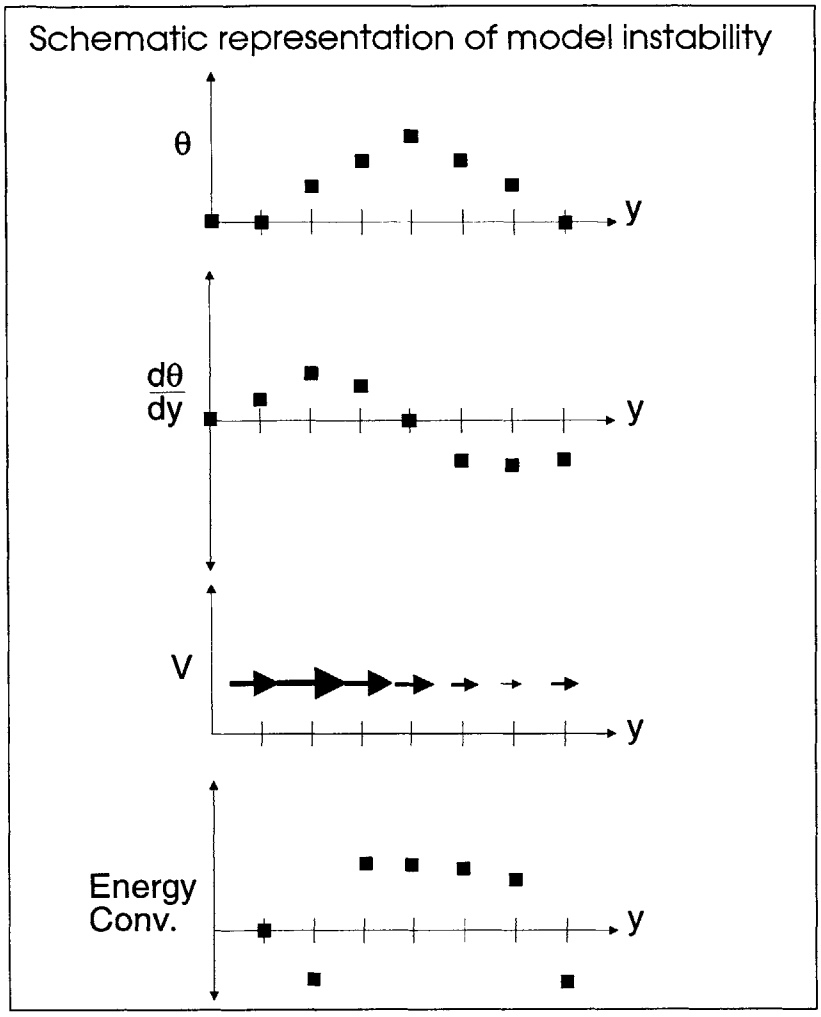

Figure 3-5: The amplification of small-scale perturbations in the potential temperature field due to Profile II baroclinic sensitivity. In the first frame, a small-scale perturbation in the potential temperature field occurs in the discretized meridional domain. The meridional potential temperature gradient is determined in the second plot through a centered finite difference numerical routine, with approximate values given. The positions of the zero point and local optima in the meridional gradient field are crucial in calculating the resulting flow and convergence fields. Representative wind arrows corresponding to the magnitude of the meridional flow are placed according to the low-level sensitivities shown in Fig. 3-4. The convergence field is calculated using the forward difference approach - the wind at each point corresponds to the exiting flow in that cell. The upstream wind is the entering wind. Note that the convergence field not only increases the magnitude of the potential temperature maximum, but also decreases the local minimum with a net tightening of the pattern. The potential temperature local minimum is amplified and shifted right while the maximum is amplified and shifted left, creating the unstable properties determined from diagnostic model runs. An opposite wind field sensitivity is required for this instability to be overcome, initiating study into another Ekman model.

geostrophic wind in Profile II, both Profile III geostrophic components have their own first order shear terms, which link their behavior to potential temperature gradients through the thermal wind relationship. At a given altitude, however, one component or the other dominates, depending on which component has a greater weighting factor. At points aloft, the desired geostrophic wind is one which is anchored at the top of the mixed layer, and whose linear shear term is influenced by synoptic-scale baroclinicity. This geostrophic wind will be denoted as

$$u_g^{LS} = U_{g*,LS} + m_{LS}\,(z - z_{LS}) \tag{3.22}$$

where $U_{g*,LS}$ is the fixed point value of the geostrophic wind, while m_{LS} is the shear term computed at the fixed point and is sensitive to large-scale baroclinicity. In the mixed layer (and down to the surface), a geostrophic wind is desired which will not produce amplification of temperature perturbations in the mixed layer. So, another geostrophic wind is introduced which has its fixed point at the surface:

$$u_g^{SS} = U_{g*,SS} + m_{SS}\,(z - z_{SS}) \tag{3.23}$$

Here, $U_{g*,SS}$ is the geostrophic wind value at the fixed point with m_{SS} likewise referring to the shear term arising from local scale-temperature gradients. In this project, the fixed point z_{SS} is assigned the value of zero. Two arbitrarily chosen profiles according to (3.22) and (3.23) are shown in Fig. 3-6. The components in (3.22) and (3.23) are then combined according to an exponential weighting function, namely

$$u_g = [U_{g*,LS} + m_{LS}\,(z - z_{LS})]\left(1 - e^{-\frac{z-z_{sfc}}{z_{scl}}}\right) + [U_{g*,SS} + m_{SS}\,(z - z_{SS})]\,e^{-\frac{z-z_{sfc}}{z_{scl}}} \tag{3.24}$$

where z_{scl} is an arbitrarily selected scaling factor. The corresponding exponential weighting functions are shown in Fig. 3-7, with the weighted geostrophic wind components (and their sum) shown in Fig. 3-8. In Appendix B, the Ekman profile derivation of the geostrophic wind profile in (3.24) yields zonal and meridional wind

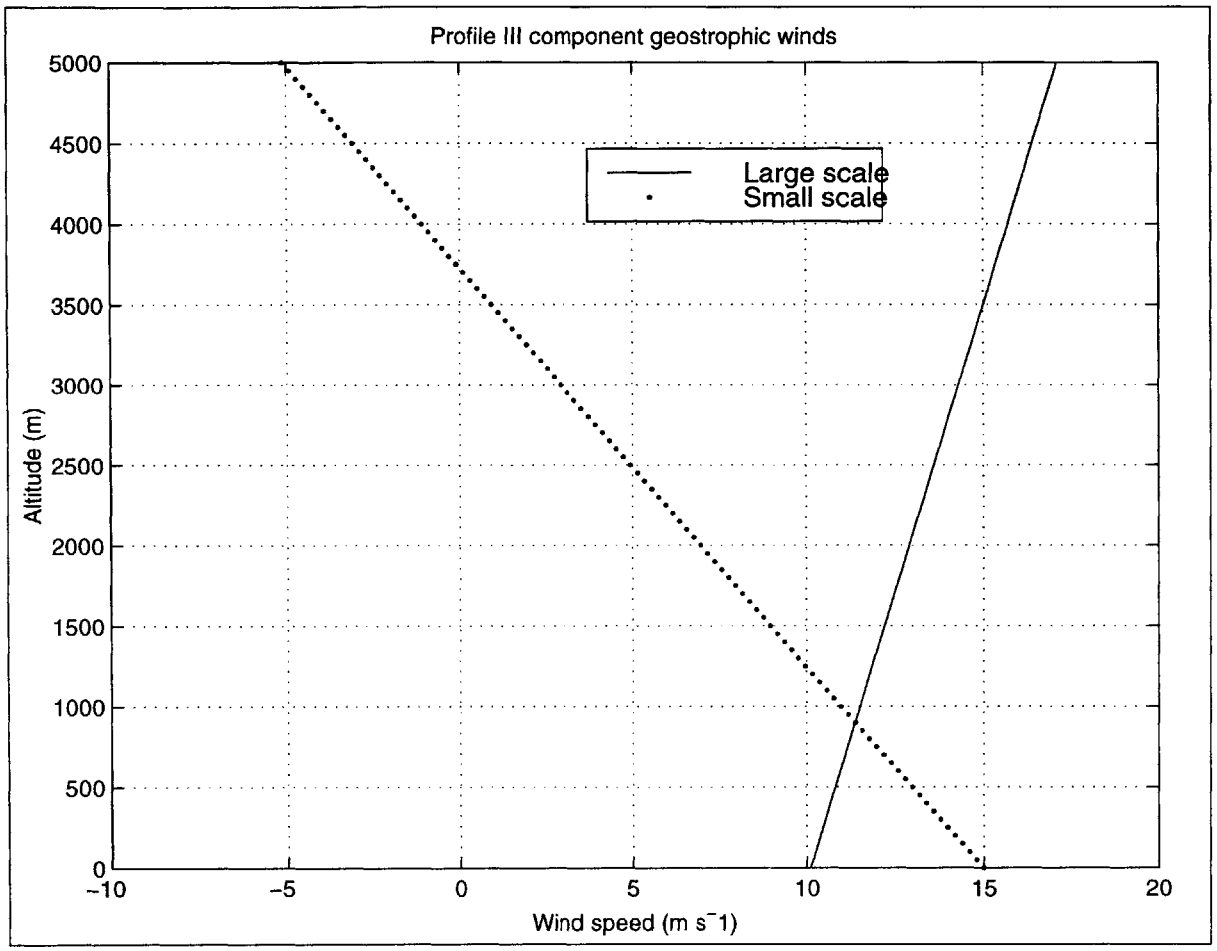

Figure 3-6: Component geostrophic winds with fixed points at the surface and aloft. The shear terms of the ground- and surface-based profiles are derived from the small scale and large scale potential temperature gradients, respectively. Though arbitrarily defined here, the small scale temperature gradients are typically of a higher magnitude (due to heterogeneity in surface heating) then the large scale gradient, which is computed from a least-squares slope of the meridional potential temperature distribution.

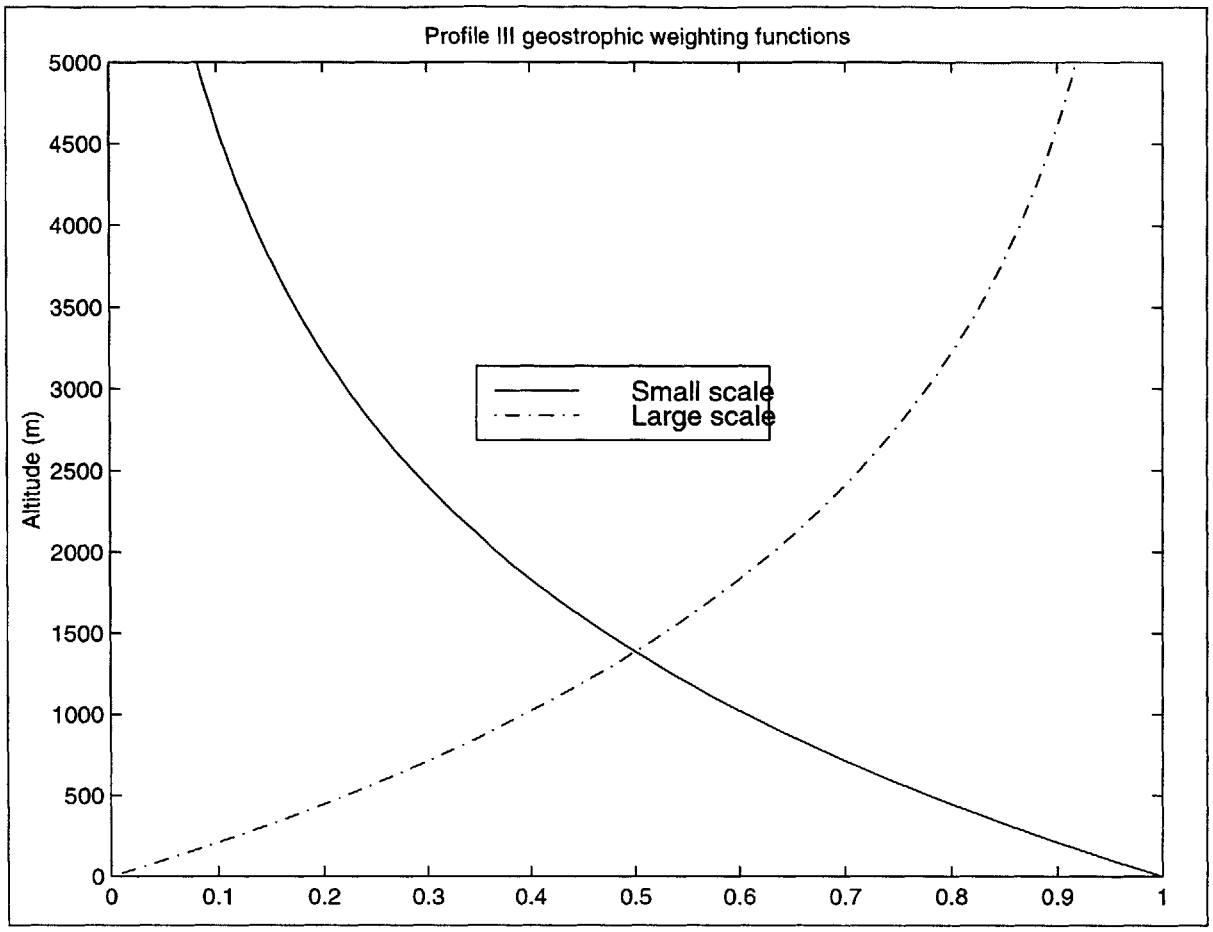

Figure 3-7: The exponential weighting functions used in Profile III, with a decay rate set at $z_{scl} = 2000$ m. These weighting functions sum to 1 at all altitudes and are multiplied by the component geostrophic winds in Fig. 3-6 to obtain a composite geostrophic wind.

components given by

$$\begin{aligned} U &= -\left(D_1 + D_2 z_{sfc} + J_3 + J_4 z_{sfc}\right) e^{-\gamma\left(z - z_{sfc}\right)} \cos\gamma\left(z - z_{sfc}\right) \\ &\quad -\left(K_3 + K_4 z_{sfc}\right) e^{-\gamma\left(z - z_{sfc}\right)} \sin\gamma\left(z - z_{sfc}\right) \\ &\quad +D_1 + D_2 z + J_3 e^{-\left(z - z_{sfc}\right)b} + J_4 z e^{-\left(z - z_{sfc}\right)b} \end{aligned} \tag{3.25}$$

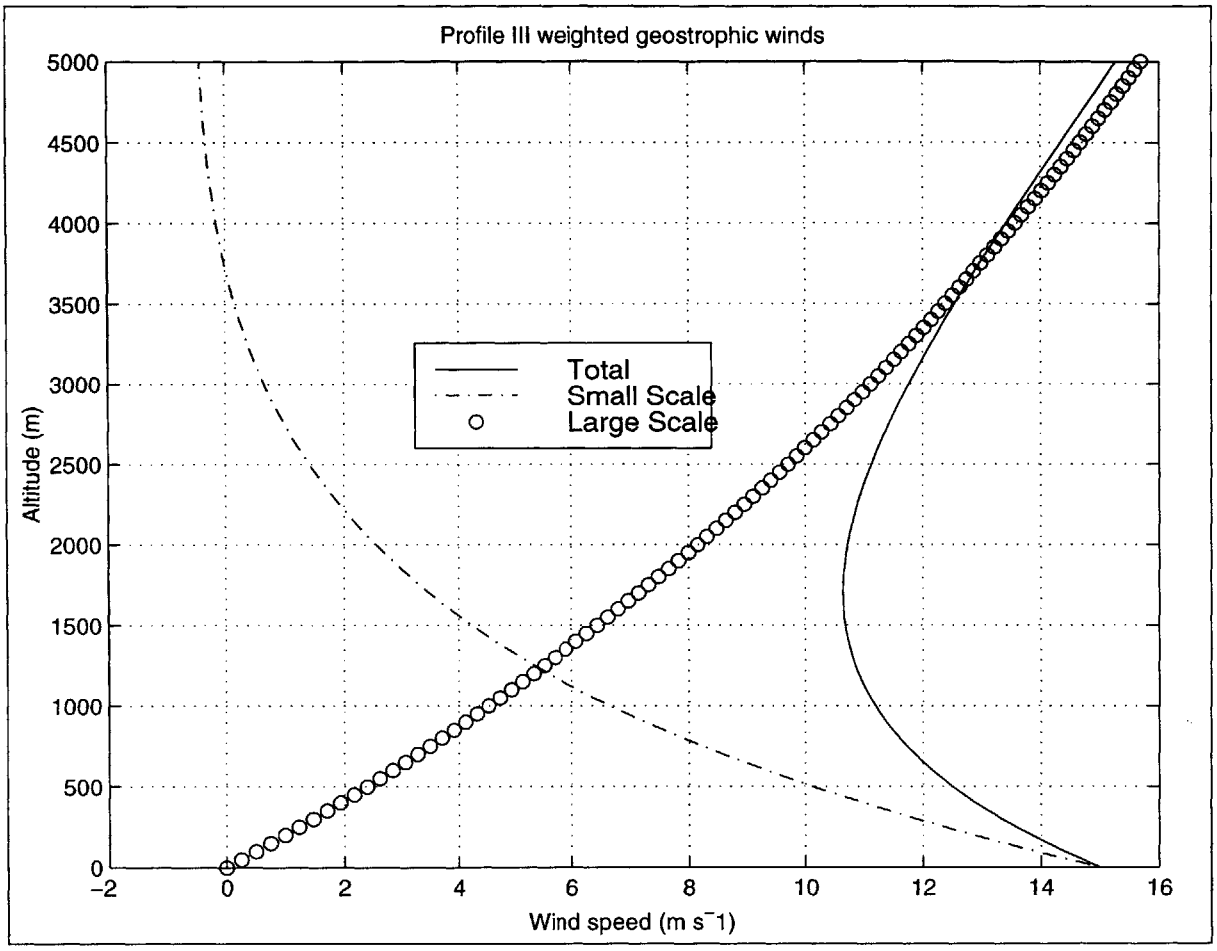

Figure 3-8: Exponentially-weighted geostrophic winds, corresponding to the components and weighting functions in Fig. 3-6 and Fig. 3-7. The first-order decay rate with respect to height is given by $z_{scl} = 2000$ m, above which the composite geostrophic profile is almost entirely dictated by the large (imposed synoptic) scale flow aloft, and below which local-scale winds dominate. To generate Profile III winds, the composite geostrophic wind shown here (solid line) is subjected to Ekman layer deflection.

$$
\begin{aligned}
V \;=\; & -\left(K_3 + K_4 z_{sfc}\right) e^{-\gamma\left(z - z_{sfc}\right)} \cos\gamma\left(z - z_{sfc}\right) \\
& + \left(D_1 + D_2 z_{sfc} + J_3 + J_4 z_{sfc}\right) e^{-\gamma\left(z - z_{sfc}\right)} \sin\gamma\left(z - z_{sfc}\right) \\
& K_3 e^{-\left(z - z_{sfc}\right)b} + K_4 z e^{-\left(z - z_{sfc}\right)b}
\end{aligned}
\tag{3.26}
$$

where D_i, E_i, J_i, K_i are coefficients which arise from the integrated geostrophic z-dependencies in the momentum diffusivity equation. Although the full analytic expression for this wind field is complicated, the overall effect upon the wind field is slight when compared with Profile II. The largest difference between the expressions in (3.20)-(3.21) and (3.25)-(3.26) is its response to baroclinic effects, which will be analyzed in the next section.

3.5 Sensitivity of Profile III winds

3.5.1 Default vertical characteristics

The Profile III zonal and meridional components exhibit the properties necessary for the two-dimensional model, as shown in the following sensitivity analysis. First, a set of "default values" was established in order to form a basis for comparison with profiles resulting from model parameter variation. The default vertical plot of the Profile III winds is shown in Fig. 3-9. Here, the meridional profile matches well with the general LLJ "shape" documented in Bonner (1968), with a maximum in the meridional wind at 700 m. The zonal flow exhibits the deflection and differential shear of the zonal geostrophic wind, as is apparent in the existence of two "slopes." (See Appendix B for further details.) The magnitude of the zonal wind exceeds that of the meridional wind, in contrast to observational evidence in Bonner (1968) but could be altered to acquire the correct absolute magnitude. Although only the meridional flow is included in the model, the complementary zonal flow is also analyzed to check for physically plausible sensitivity to baroclinic effects aloft.

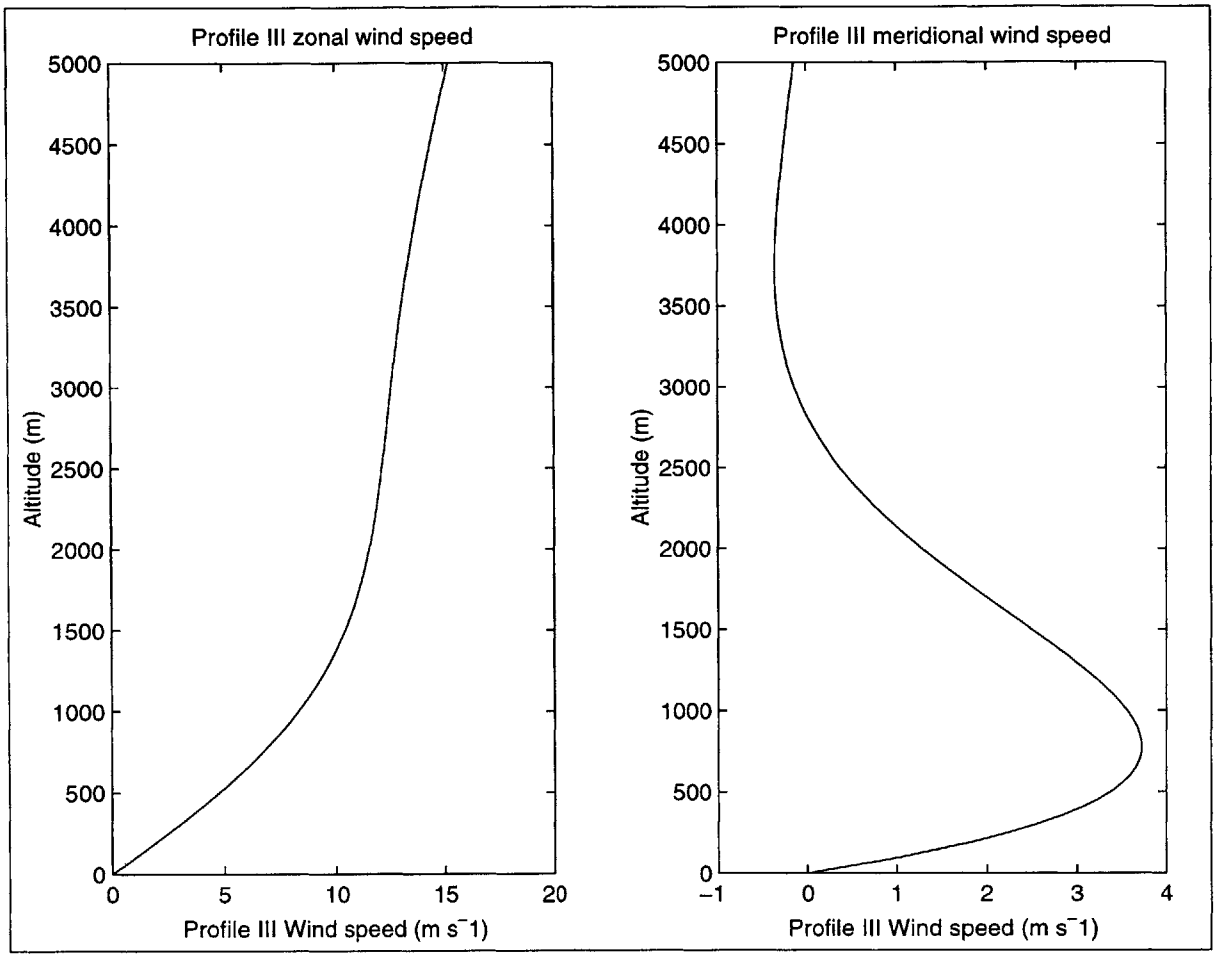

Figure 3-9: The u and v flow components generated from default settings. In all Profile III sensitivity plots, the following parameters hold, except the variable being analyzed: $f = 10^{-4}\text{s}^{-1}$, $z_{ek} = 3500$ m, $z_{sfc} = 0$, $\theta = 280$ K, $\frac{\partial\theta}{\partial y}\Big|_{SS} = 10^{-5}$ K m^{-1}, $\frac{\partial\theta}{\partial y}\Big|_{LS} = 5 * 10^{-6}$ K m^{-1}, $U_g^{LS} = 15$ m s^{-1}, $U_g^{SS} = 15$ m s^{-1}, $z_{scl} = 2000$ m. Notice the desired LLJ-like meridional wind structure, with a highly pronounced maximum at around 800 m.

3.5.2 Large-scale vs. small-scale baroclinic effects

In the meridional model, large-scale potential temperature gradients are defined as the least squares linear regression slope of potential temperature field, while small scale temperature gradients are found using a centered finite difference approach (see later section for boundary layer effects). The local finite difference gradient requires a unique numerical value at each point, while the large-scale gradient is assumed to be constant over the entire domain. Figs. 3-10 and 3-10 show the effect of the small- (local-) scale temperature gradient upon the zonal and meridional winds, respectively. The zonal wind field aloft increases in magnitude when the temperature gradient becomes more negative, which is the desired response, as specified earlier. Similarly, the meridional wind responds to local temperature gradients by increasing in magnitude at lower levels when the baroclinicity becomes more negative. Thus, the Profile III meridional wind field responds in a fashion opposite to that in Fig. 3-5. With Profile III, a meridional temperature perturbation would be damped, rather than amplified by the ensuing convergence pattern. The wind arrows in Fig. 3-5 would reflect the opposite pattern, and would serve to de-amplify the peak.

Besides adhering to the spatial stability constraint, the Profile III zonal component must respond positively (at points aloft) to increasingly negative large-scale temperature gradients, as is typical of N.H. weather patterns. Indeed, Fig. 3-12 shows that above the top of the Ekman layer (3500 m) the zonal wind exhibits the required response. Below that point, a more subdued sensitivity of the opposite sign occurs. Because the large-scale gradient should change slowly and is spatially invariant, the sensitivity to large scale gradients in Fig. 3-13 does not effect model stability.

3.5.3 Sensitivity to fixed-point geostrophic wind

The response of Profile III winds to fixed-point geostrophic wind values is governed by two effects. First, the exponential weighting of the geostrophic winds dictates that the large-scale geostrophic wind (and hence its fixed point) will have a greater impact

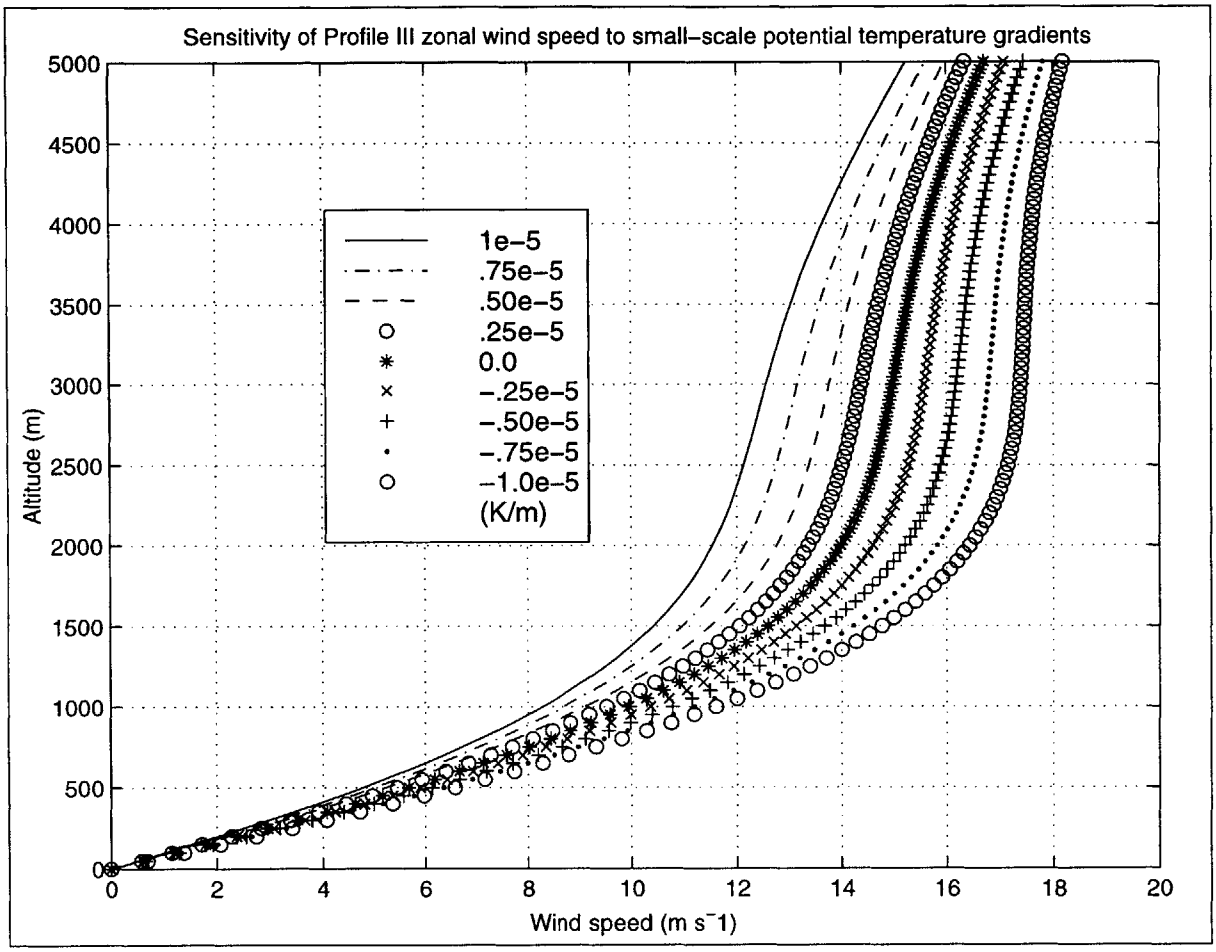

Figure 3-10: The composite Ekman-deflected u component - this is not the geostrophic zonal flow, but exhibits the geostrophic flow under the influence of friction. Notice how this field vanishes at z=0, while the geostrophic flow in preceding figures had a non-zero value at the surface. It is clear from this plot that increasingly negative small-scale baroclinicity (colder air to the north) creates a stronger zonal flow, as one would expect in a typical Northern Hemisphere regime.

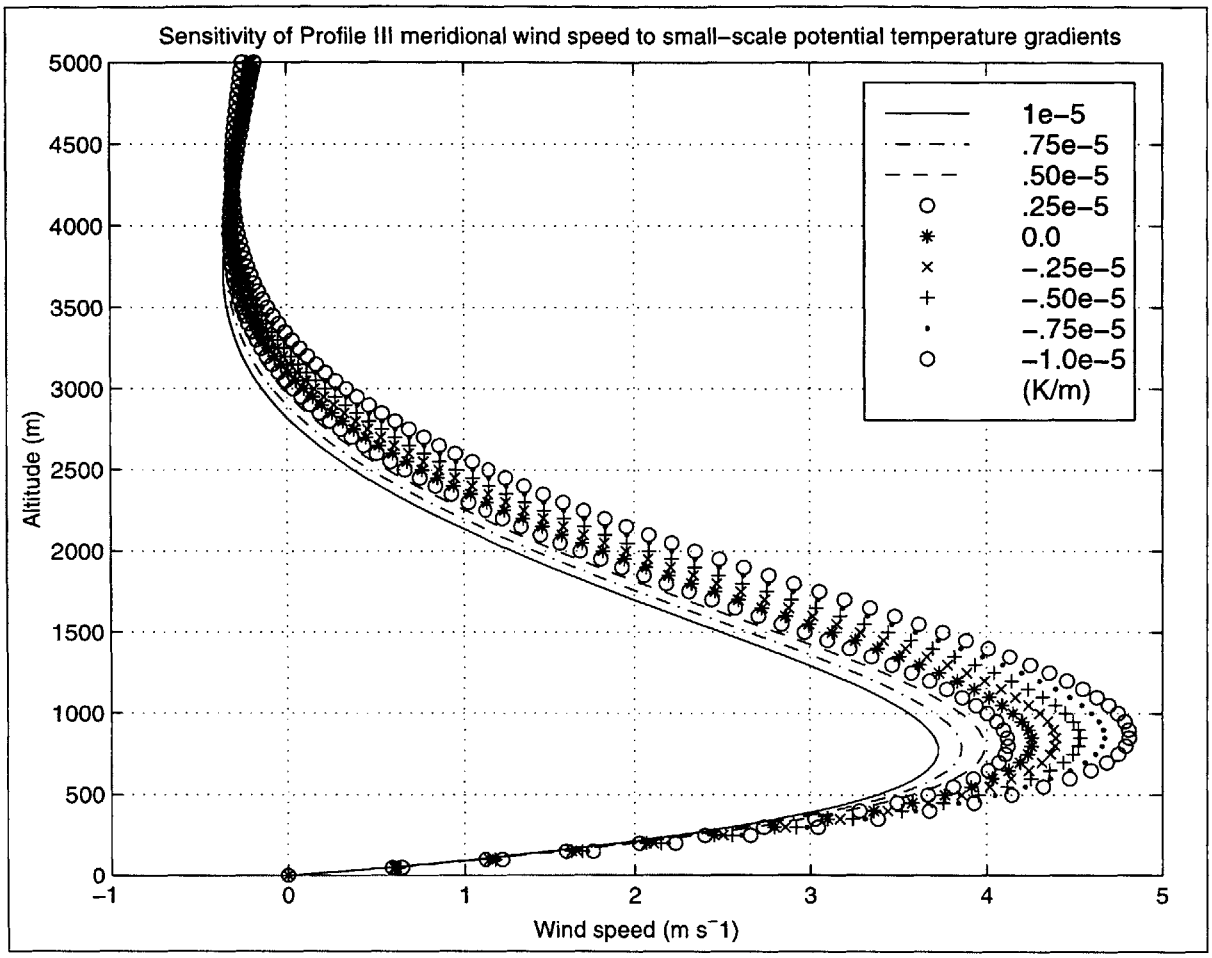

Figure 3-11: This plot shows the change in meridional flow with increasingly baroclinic conditions at the surface. The region of maximum impact of shear occurs at low levels, because of the exponential decay of surface geostrophic component upon the overall wind field, and since the Ekman spiral meridional wind is ageostrophic and decays with height. Again, by varying the small scale temperature gradient by a factor of 10, the meridional wind changes by .25 at the LLJ height.

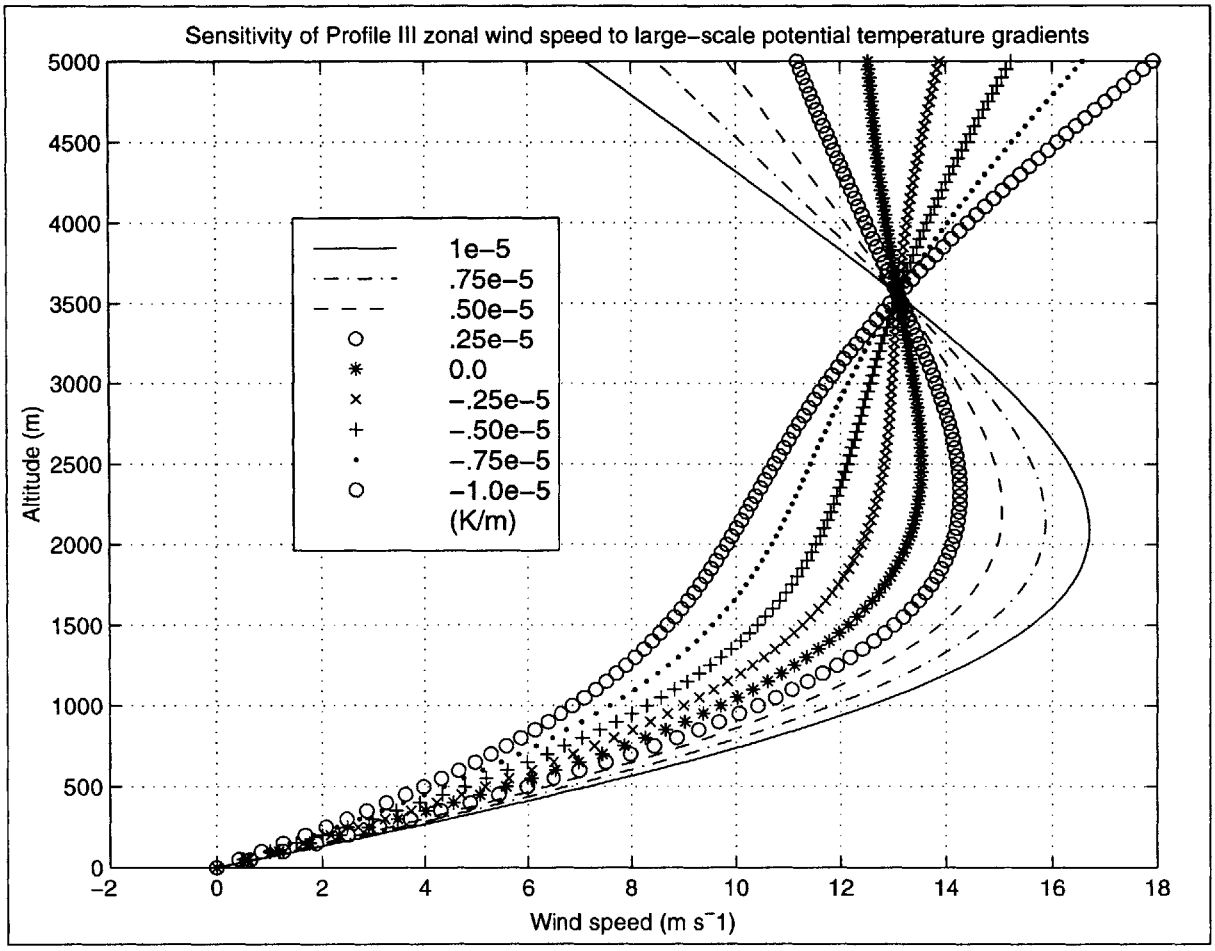

Figure 3-12: The zonal wind exhibits opposite trends above and below the Ekman layer height=3000 m. Aloft, the zonal wind increases with negative baroclinicity. At lower levels the wind shows the opposite trend, although the change is less pronounced due to the Profile III exponential weighting with respect to height.

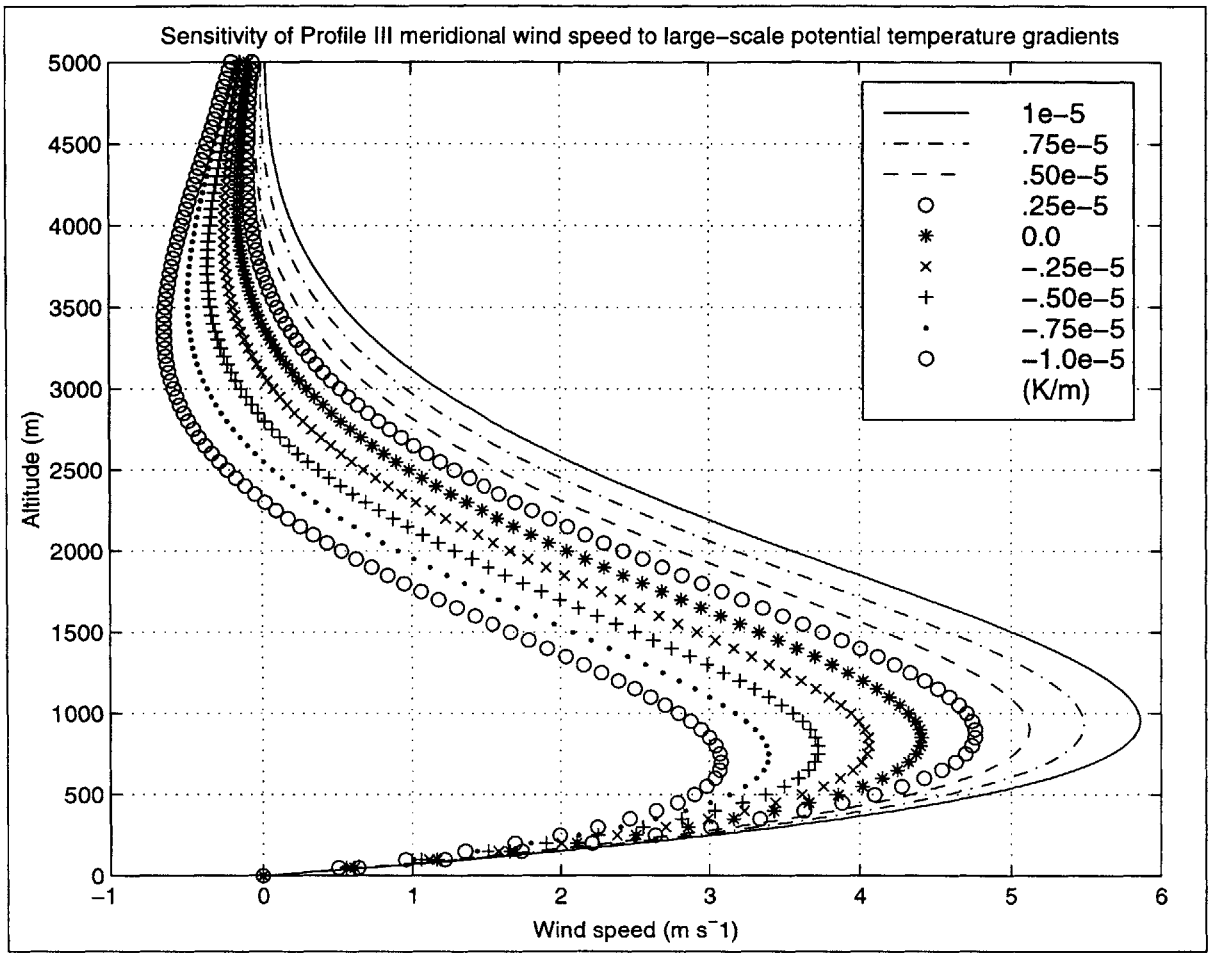

Figure 3-13: The change in meridional wind due to perturbations in the large-scale temperature gradient. As the meridional temperature gradient becomes more positive, the wind velocity increases. However, it is unlikely that the large scale gradient would exhibit such a large range of magnitudes, so this effect is not deleterious to the overall scheme for both modeling a LLJ with desired sensitivities and for preventing numerical instability due to truncation error. The bifurcation point on the zonal flow plot disappears in this case because the meridional flow does not switch sign above the Ekman height - refer to hodograph diagrams in Appendix B.

upon the winds at higher altitudes, while at lower levels the surface geostrophic wind (and its fixed point) will have a greater effect. Second, the Ekman spiral creates a meridional wind which decays with height, while the zonal wind flow approaches the background geostrophic wind with increasing height. So, according to the derivation in Appendix B, the meridional wind should show a limited response with increasing altitude, while the zonal flow should approach a linear response at height. Fig. 3-14 shows the effect of increasing the large scale geostrophic wind at the fixed point with identical shear throughout. As expected, the zonal flow at all levels is positively correlated with the large-scale fixed point value, with the highest sensitivity at points aloft. The meridional winds in Fig. 3-15 are also positively correlated, with greatest sensitivity at the LLJ altitude, but also for a significant part of the profile at higher points, due to effects just described. In contrast, the zonal wind shows the strongest sensitivity to U_{go}^{SS} at 1500 m, and the meridional flow shows the greatest sensitivity at 800 m. Due to the exponential weighting functions, the zonal flow in Fig. 3-14 shows an asymptotic approach to the unchanged large-scale geostrophic component. The meridional flow also shows a rapid decrease in sensitivity with respect to height, as the changes in U_{go}^{SS} are downed out by the large-scale geostrophic wind.

3.5.4 Effects of location and scaling

The latitude of a given wind profile influences the shear, and therefore the geostrophic wind of Profile III winds, according to the Coriolis dependence in (3.18). The background geostrophic wind is assumed to be constant with latitude, so any north-south variations will be due to the impact upon the linear shear terms in the large and small scale components. Figs. 3-18 and 3-19 show a very slight impact of latitude upon the zonal and meridional profiles over the range of Northern Hemispheric locations encountered in the LLJ model. In both cases, the wind field increases in magnitude with increasing latitude, with the exception of those altitudes far above the LLJ axis. For the purposes of the model, this effect is included, but is not worthy of further attention, even though Coriolis deflection might be important in forming the bow-shaped jet core over the Midwest. e.g., (Bonner 1968) The exponential

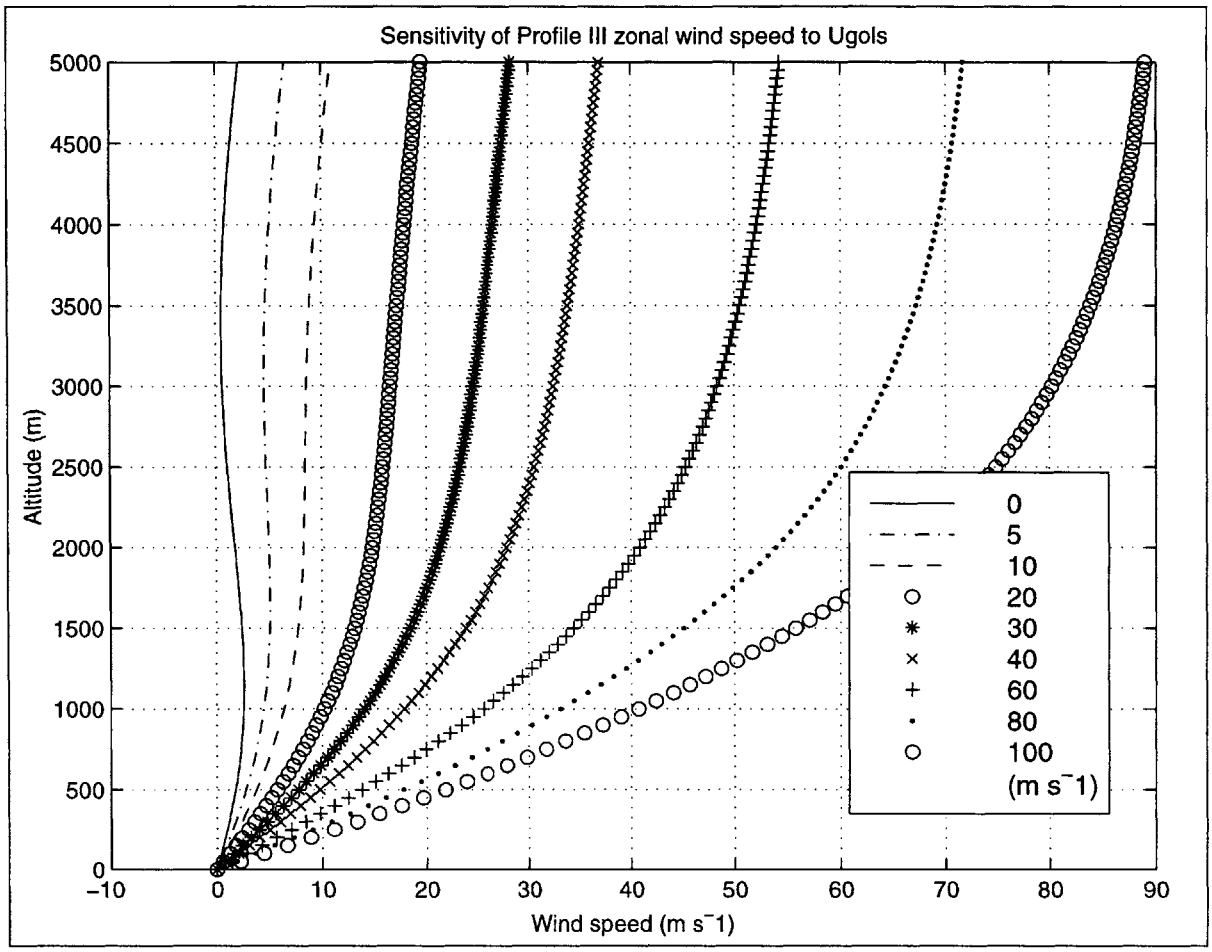

Figure 3-14: The change in zonal wind with respect to changes in large-scale geostrophic wind parameter. The variation of the zonal wind is greatest at higher altitudes, weighted by the exponential scaling as well as the upper limit to the Ekman spiral.

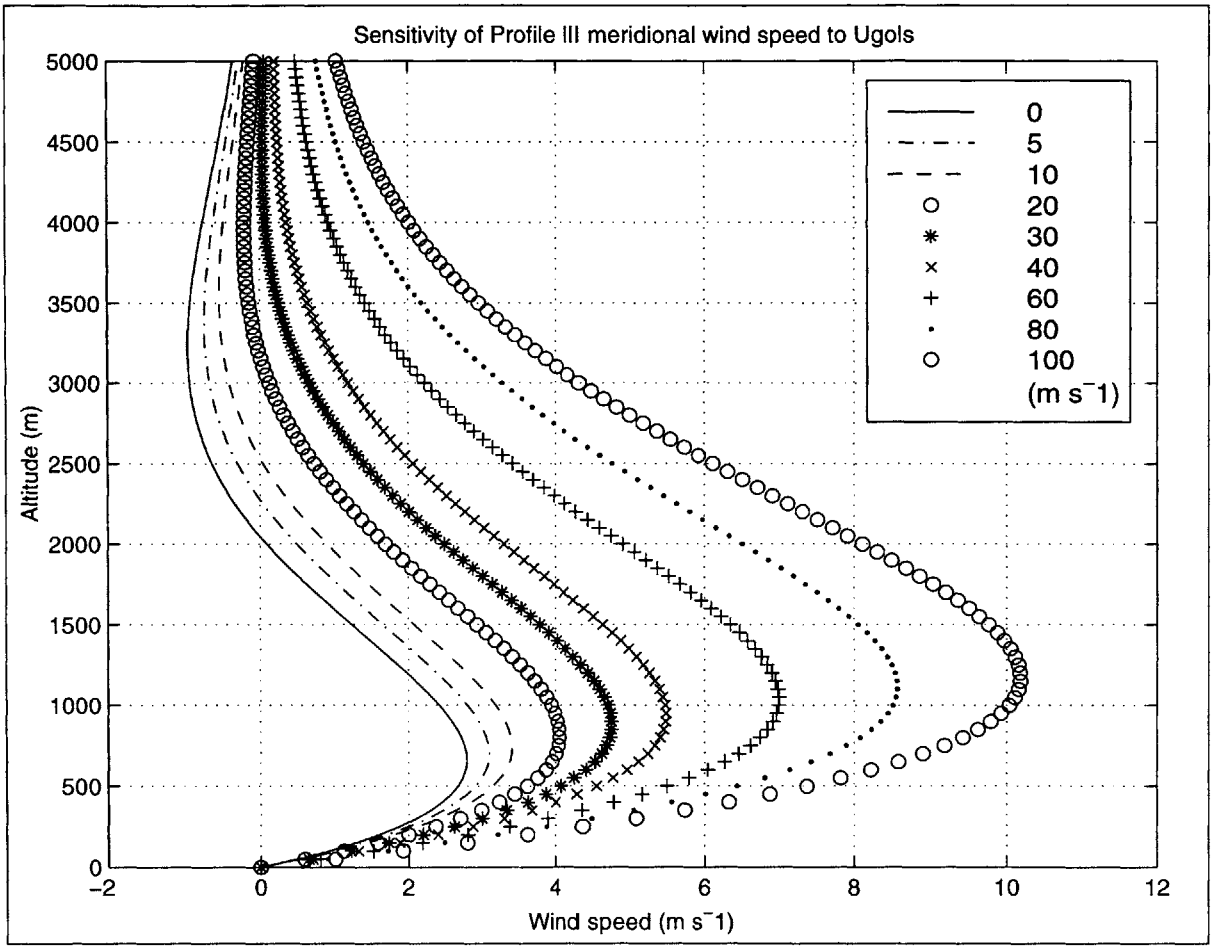

Figure 3-15: As opposed to the zonal wind profile, the meridional profile shows the greatest sensitivity to large scale geostrophic wind increases at the level of the LLJ. The Ekman spiral meridional wind approaches zero with increasing altitude, regardless of the fixed-point value.

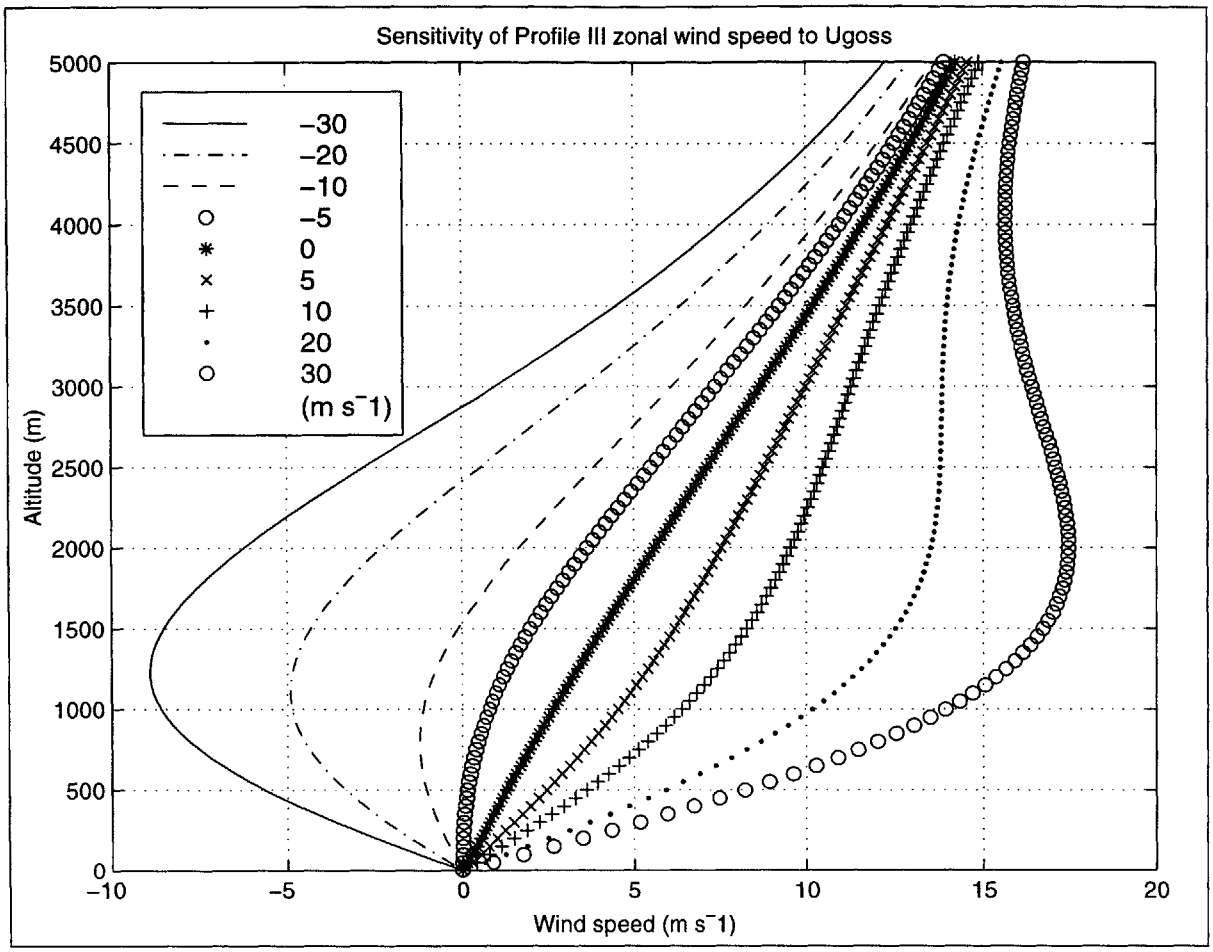

Figure 3-16: The greatest sensitivity in this plot occurs at the height of the LLJ, as a result of the exponential weighting of the geostrophic winds. Here, negative values of the surface geostrophic wind are considered, whereas in the large-scale sensitivity plots only positive values were used. Notice that as the profiles increase in altitude, they are less sensitive to perturbations in the surface geostrophic wind, as intuitively should be the case.

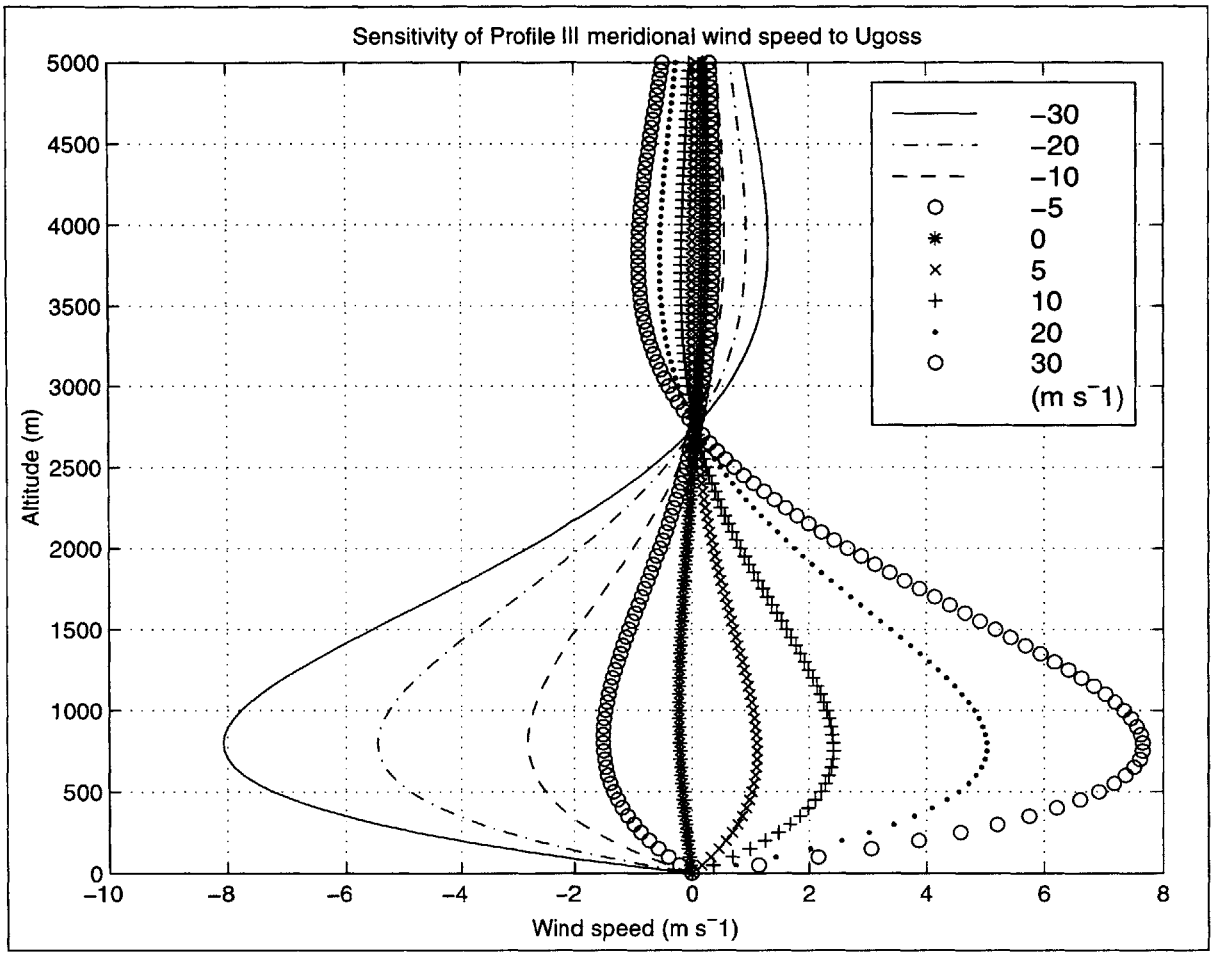

Figure 3-17: The sensitivity of meridional wind to the surface geostrophic wind parameter. Note the fixed point at the Ekman height of 3500 m. The sensitivity is of opposite polarity, and of a lesser magnitude aloft compared with regions below the Ekman depth.

scaling parameter limits the amount that each respective geostrophic component (local- or large-scale) affects the resultant wind. Figs. 3-20 and 3-21 show a very wide logarithmic span of the wind profiles with various scale heights. In both the zonal and meridional plots, the wind profiles fall into two distinct families of curves, which simply correspond to the two (unchanging) geostrophic wind profiles dominating over each other, in the extreme limits of the scale height. Intermediate profiles lie in between the two families, since both geostrophic wind profiles are providing a significant impact on the overall profile.

3.6 Computation of meridional energy and vapor fluxes

The general expressions for the vertically-integrated meridional transport of energy and vapor into an atmospheric column from neighboring columns are given by F_E and F_{H_2O}, respectively,

$$F_E = \int_{z_{sfc}}^{h} \rho c_P T V dz \tag{3.27}$$

$$F_{H_2O} = \int_{z_{sfc}}^{h} \rho q V dz \tag{3.28}$$

where V is the total meridional wind, h is the height of the mixed layer, z_{sfc} is the elevation of the surface from mean sea level, q is the specific humidity, c_P is the specific heat capacity of air at constant pressure, and ρ is the mass density of air. The meridional wind passing through an atmospheric column at a particular grid point in the model domain is partitioned into the geostrophic and ageostrophic components, namely

$$V(z) = v_g(z) + v_a(z) \tag{3.29}$$

where v_g and v_a are the geostrophic and ageostrophic components of the meridional wind, respectively. Using these expressions, the fluxes in (3.27) and (3.28) become

$$F_E = \int_{z_{sfc}}^{h} \rho c_P T V dz = \int_{z_{sfc}}^{h} \rho c_P T \left(v_g + v_a\right) dz \tag{3.30}$$

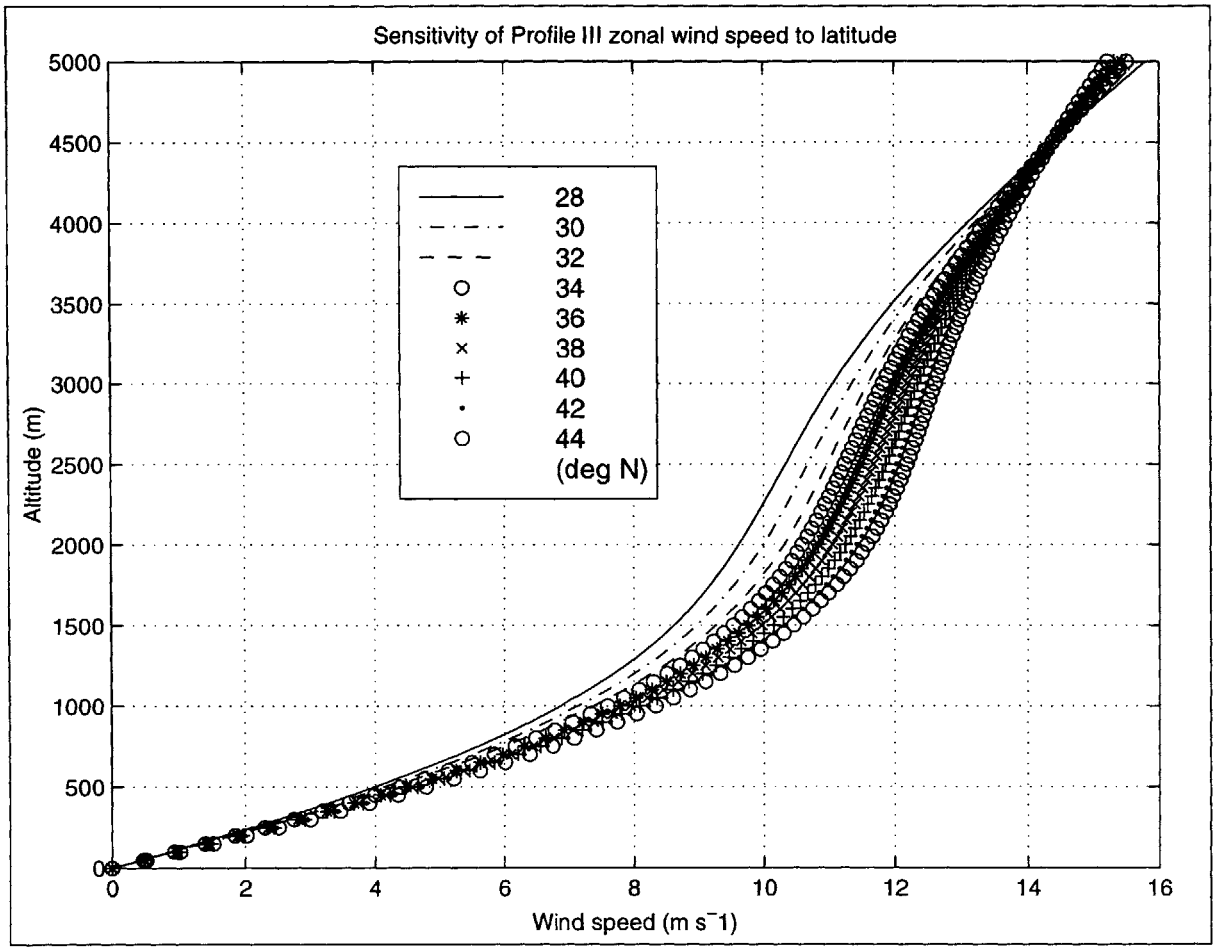

Figure 3-18: The effect of latitude upon the zonal flow. As the latitude increases, the contribution of the shear due to local temperature gradients is diminished. The ultimate impact upon the the wind speed is determined by the sign of $\frac{\partial \theta}{\partial y}$. The shear term responds, but not in an intuitive way (see derivation of thermal wind). The background geostrophic flow is not dependent on latitude as a model assumption.

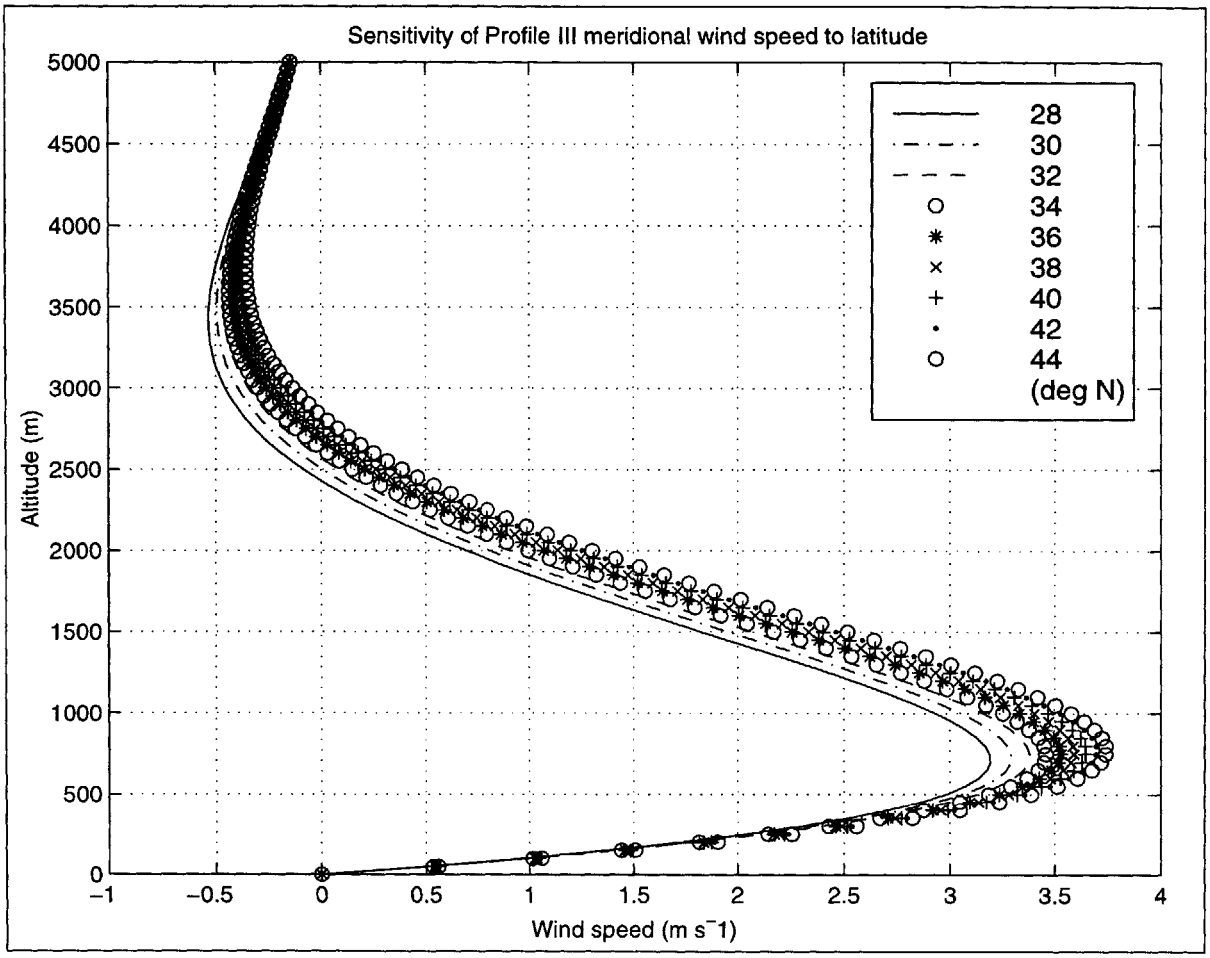

Figure 3-19: The effect of latitude upon the meridional flow. As the latitude increases in magnitude, the shear term responds, but not in a straightforward manner (see Fig. 3-18).

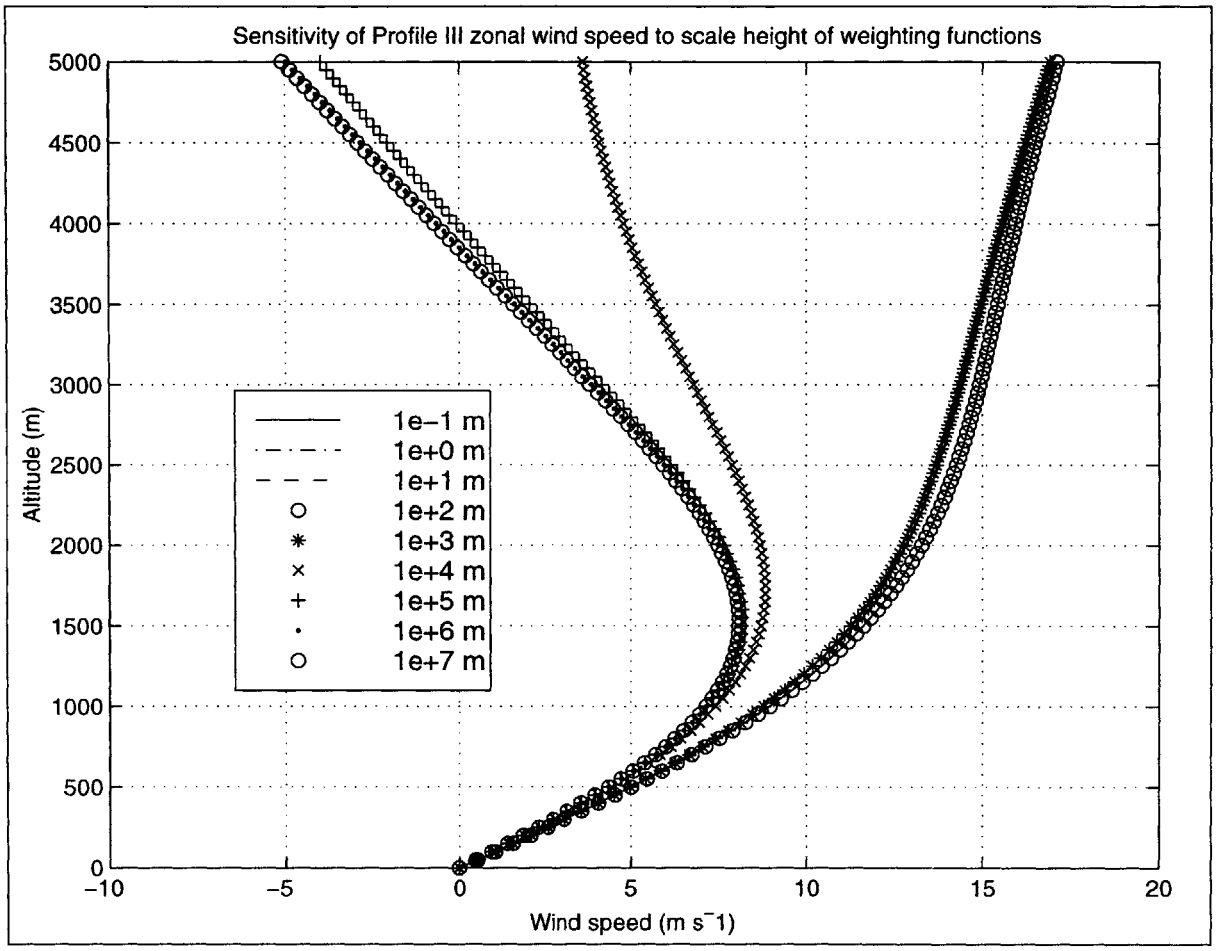

Figure 3-20: The impact of order-of-magnitude adjustments of the scale height upon the zonal wind. Note the wind profile transition period between 1000 and 10000 m. At orders of magnitude outside of this intermediate range, only one of the geostrophic wind profiles dominates. However, if the scale height is the on the order of the Ekman layer height, both components will exert a significant influence upon the overall structure. The scale height has a relatively small impact upon the zonal wind, particularly in contrast to order of magnitude changes in the large scale potential temperature gradient.

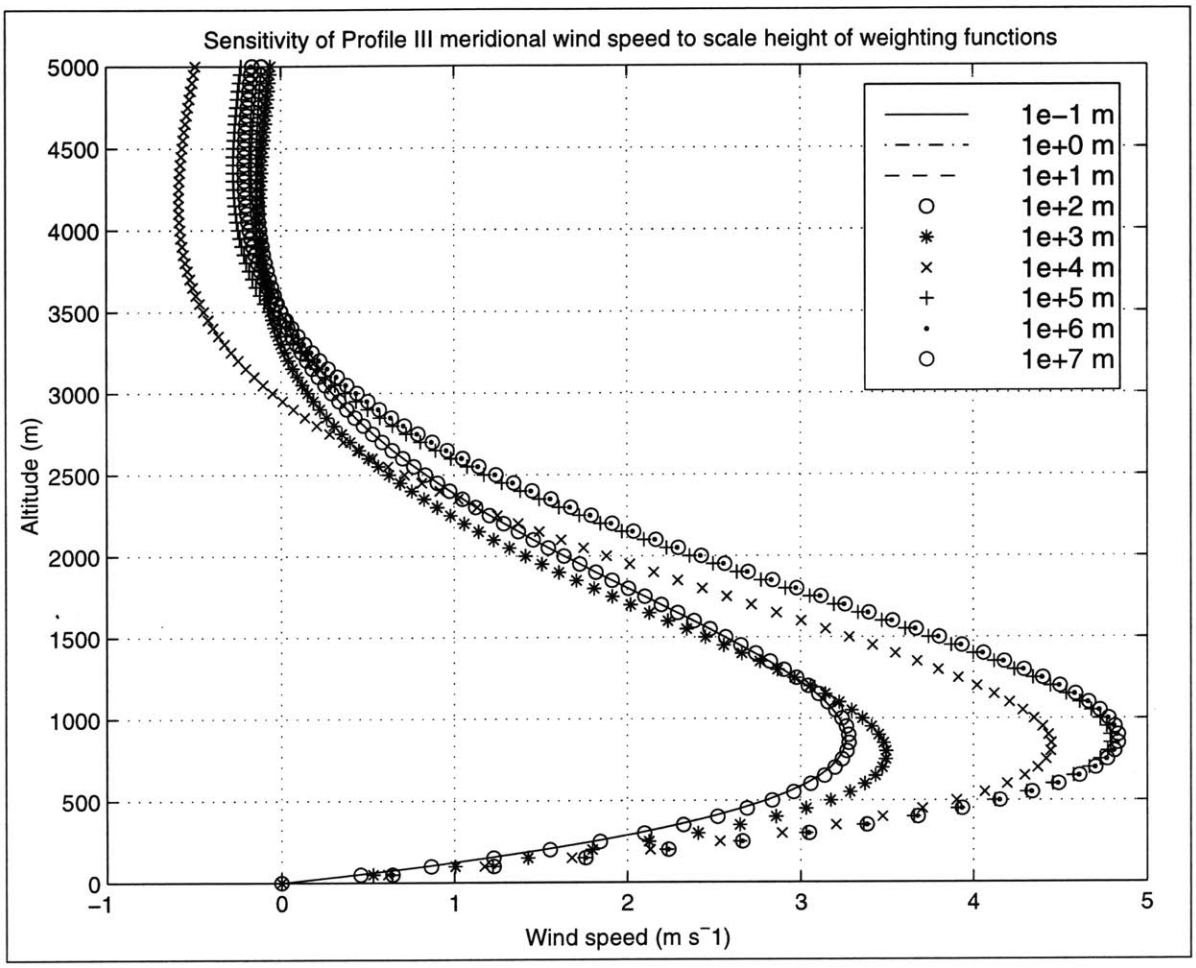

Figure 3-21: The meridional wind field shows a very slight sensitivity to changes in the scale height. The meridional wind field at the height of the LLJ shows bipolar behavior as evidenced in the two distinct families of curves. One family corresponds to the Ekman deflection of the large scale geostrophic flow (lesser magnitude v curves) while the other family corresponds to the deflection of the small-scale flow only.

$$F_{H_2O} = \int_{z_{sfc}}^{h} \rho q V dz = \int_{z_{sfc}}^{h} \rho q \left(v_g + v_a\right) dz \tag{3.31}$$

After substituting the Profile III expression for V in (3.26), the energy and vapor fluxes in (3.27) and (3.28) now become

$$\begin{aligned} F_E = \int_{z_{sfc}}^{h} \rho c_P \left(\theta - \Gamma_d z\right) \Big[& - \left(K_3 + K_4 z_{sfc}\right) e^{-\gamma\left(z - z_{sfc}\right)} \cos\gamma \left(z - z_{sfc}\right) \\ & + \left(D_1 + D_2 z_{sfc} + J_3 + J_4 z_{sfc}\right) e^{-\gamma\left(z - z_{sfc}\right)} \sin\gamma \left(z - z_{sfc}\right) \\ & K_3 e^{-\left(z - z_{sfc}\right)b} + K_4 z e^{-\left(z - z_{sfc}\right)b} \Big] dz \end{aligned} \tag{3.32}$$

$$\begin{aligned} F_{H_2O} = \int_{z_{sfc}}^{h} \rho q \Big[& - \left(K_3 + K_4 z_{sfc}\right) e^{-\gamma\left(z - z_{sfc}\right)} \cos\gamma \left(z - z_{sfc}\right) \\ & + \left(D_1 + D_2 z_{sfc} + J_3 + J_4 z_{sfc}\right) e^{-\gamma\left(z - z_{sfc}\right)} \sin\gamma \left(z - z_{sfc}\right) \\ & K_3 e^{-\left(z - z_{sfc}\right)b} + K_4 z e^{-\left(z - z_{sfc}\right)b} \Big] dz \end{aligned} \tag{3.33}$$

3.7 Parameterization of vertical velocity

Because the convergence of mass is an undesirable component in the energy flux calculation (e.g., Fig. 3-5), it follows that by removing mass divergence some model instabilities may be averted. This derivation assumes the conservation of energy in the cells of the meridional model, and is based upon the conservation of mass entering and exiting a 3-D control volume. The net accumulation of mass in a grid cell is given by (in kilograms per second)

$$M_{in} - M_{out} = \rho \Delta x \int_0^h \left(V_{i-1} - V_i\right) dz \tag{3.34}$$

This mass is evacuated from the cell by a parameterized vertical velocity in the cell, such that all mass accumulation per unit time is offset by the mass of air evacuated at the top of the cell. The vertical velocity is assumed to be horizontally uniform;

the mass leaving the top of the cell per unit time is given by

$$M_{top} = \rho w_{top} \Delta x \Delta y \tag{3.35}$$

Equating the expressions in (3.34) and (3.35) and solving for the vertical velocity yields

$$w_{top} = \int_0^h \frac{(V_{i-1} - V_i)}{\Delta y} dz.$$

Chapter 4

Model Results

4.1 Overview of spatially-coupled mixed-layer models

Utilizing the theoretical concepts derived in Chapter 3, a series of incremental modeling studies was designed to assess LLJ activity based upon mixed layer processes. First, a set of stand-alone codes was implemented to diagnose feedbacks resulting from Profile III sensitivities to spatial gradients in model parameters. Only a minimal "skeleton" of boundary layer processes was used to isolate the effects of meridional variability; these simple models helped establish confidence in 2-D feedbacks *before* engaging the mixed layer feedbacks at both the 0-D and 2-D levels. Table 4.1 shows an outline of the three tests used to achieve this goal. The three incremental goals of these tests were (i) to comprehensively assess the behavior of winds resulting from a given stationary meridional temperature field, (ii) to establish patterns between time-dependent energy coupling and spatial flow profiles, and (iii) to verify the transport of moisture as a passive admixture. These respective studies will be denoted Test 1, Test 2, and Test 3, respectively; the outcomes of these models follow later in this chapter. In each of the prototype models, consult Table 4.3 for specific information on model parameters used to run the model.

After establishing patterns of meridional coupling with the prototype models, the

mixed layer 0-D model is inserted at each point, replacing the temporary boundary layer parameterization in Tests 1-3. Three types of feedbacks were possible in such a model: (i) those limited to the mixed-layer model; (ii) those created by meridional coupling alone (e.g. the Profile II feedbacks which have been already discussed); and (iii) those feedbacks caused by *both* the mixed-layer forcing and meridional coupling. With regard to the hypothesis of this paper, the final category of feedbacks is of the most interest for constructing a LLJ model. The first category of feedbacks has been largely documented by Kim and Entekhabi (1998), which include effects caused by surface evaporation resistance and atmospheric specific humidity. The second category of feedbacks is tested using the results of the simple prototype models, and are only a function of spatial coupling. For example, Tests 1-3 revealed that Profile II flow creates a nefarious feedback between the temperature and convergence fields (as shown in Fig. 3-5). This phenomenon could have been overlooked if the model were introduced all at once; the incremental approach facilitated a more timely and complete solution to the error and motivated the development of Profile III flow.

The third category of feedbacks (including, most notably, the role of soil-moisture in creating stronger or weaker LLJ's) was investigated using a set of experiments which systematically introduced more complex processes and tendencies into the model, in parallel with the meridional coupling prototypes. A list of these tests is found in Table 4.2, where five separate trials are briefly described. The model parameters used in the executed models are found in Table 4.3. Experiment 1 calculates winds at each point in the domain, as a separate diagnostic residing offline from the mixed-layer model; the winds do not impact the state variables in neighboring cells. The second experiment couples the winds and the potential tendency terms through the vertically integrated heat flux, $Q_h\,(V)$. Experiment 3 likewise couples the meridional and mixed layer moisture tendency terms. In Experiment 4, the frictional velocity is altered from a constant parameter to a variable that can both change through time and space based upon the calculated winds at screen-height. Finally, Experiment 5 utilizes the fully integrated model to compute meridional LLJ winds. In this thesis, only the prototype models and Experiment 1 were completed as outlined here. Further work could be

Strategy of Successive 2-D Models

Test Number	$V = V\left(\frac{\partial\theta}{\partial y}\right)\Big\|_{t=t_0}$	$V = V\left(\frac{\partial\theta}{\partial y}\right)\Big\|_{t}$	$Q_q(V)$	Description of Test
Test 1	Yes	No	No	Diagnostics to test wind field in time invariant θ profile
Test 2	Yes	Yes	No	"Dry" time dependent test of energy coupling
Test 3	Yes	Yes	Yes	Test of passive moisture transport

Table 4.1: The incremental stages used to develop a prototype meridional LLJ model. As intermediate steps toward the goal of modeling soil moisture sensitivity, these tests established patterns of Profile III flow under highly constrained atmospheric conditions with a minimum of parameterized boundary layer physics. The series of stand-alone codes verified LLJ sensitivity to meridional baroclinic conditions (Test 1), deployed Profile III under time-dependent energetics (Test 2), and investigated passive water vapor transport under the influence of time-dependent meridional flow (Test 3). By separately modeling the meridional coupling, the tests formed a practical vantage point from which to assess the impact of a more complex suite of mixed-layer processes.

Series of Coupled Models: Experimental Design

Experiment Number	$R_n(\phi)$	$V = V\left(\frac{\partial\theta}{\partial y}\right)\Big\|_{t=t_0}$	$V = V\left(\frac{\partial\theta}{\partial y}\right)\Big\|_{t}$	$Q_\psi(V)$	u^{fric}	$\frac{ds}{dt} = f(s)$	Description of trial
1	Yes	Yes	No	No	No	No	Meridional wind diagnostics
2	Yes	Yes	Yes	No	No	No	Heat advection coupled
3	Yes	Yes	Yes	Yes	No	No	Heat & moisture advection coupled
4	Yes	Yes	Yes	Yes	Yes	No	Heat, moisture, and momentum coupled
5	Yes	Yes	Yes	Yes	Yes	Yes	Full Model

Table 4.2: The proposed implementation of boundary-layer processes in a coupled meridional domain, using a 0-D code from Kim and Entekhabi (1998). Implementation of boundary layer effects begins with an uncoupled diagnostic run (Exp. 1), and continues systematically with energetic coupling (Exp. 2), vapor transport and feedbacks (Exp. 3), aerodynamic effects at the surface in terms of the frictional velocity (Exp. 4), and with a non-trivial soil moisture tendency term (Exp. 5). In this thesis, only the first experiment was completed: LLJ meridional coupling and boundary layer effects were implemented separately but not together. The latter entries in this table serve as a point of departure for further research.

done to fully implement the final experiments in the mixed-layer implementation. The following sections report on the results of the modeling studies and lay the groundwork for future LLJ models.

Model Parameters

Parameter	Test 1 (Sinusoidal)	Test 1 (Linear)	Test 2 (Sinusoidal)	Test 2 (Linear)	Test 3	Exp. 1	Description
BC	NA	NA	Periodic	Nondiver-gent	Nondiver-gent	Nondiver-gent	Boundary Conditions
DT/DY	200 s/50 km	200 s/50 km	200 s/50 km	200 s/50km	200 s/50 km	200 s/50 km	Time increment/y increment
f_0	6.845E-5 s^{-1}	6.845E-5 s^{-1}	6.845E-5 s^{-1}	6.845E-5 s^{-1}	6.845E-5 s^{-1}	6.845E-5 s^{-1}	Cor. param. at southern boundary
z_{ekman}	3500 m	3500 m	3500 m	3500 m	3500 m	3500 m	Ekman height
K_m	42.48 $m^2 s^{-1}$	42.48 $m^2 s^{-1}$	42.48 $m^2 s^{-1}$	42.48 $m^2 s^{-1}$	42.48 $m^2 s^{-1}$	42.48 $m^2 s^{-1}$	Momentum Diffusivity
H	NA	NA	1500 m	1500 m	1500 m	Variable	Mixed-layer height
z_{scl}	2E6 m	2E6 m	2E6 m	2E6 m	2000 m	2000 m	Profile III scaling height
S_0	NA	NA	50.5 W m^{-2}	50.5 W m^{-2}	100 W m^{-2}	modeled	Effective shortwave flux
ϵ	NA	NA	.04	.04	.04	modeled	Longwave emmisivity

Table 4.3: List of selected model parameters. Here, "NA" refers to the Test 1 case in which that variable was not needed. "Modeled" refers to parameters which are no longer needed in the meridional coupling routines, since they are now incorporated into the 0-D model from Kim and Entekhabi (1998)

4.2 Prototype meridional models

4.2.1 Meridional wind and feedback diagnostics: Test 1

Meridional wind and flux profiles from a sinusoidal temperature field

The first prototype LLJ model was designed as an extension of the Profile III sensitivity studies conducted in Chapter 3. Here, however, the profile is not only analyzed for its vertical characteristics, but also for the horizontal variation in response to spatial gradients in the potential temperature field. By definition, this test is actually not a "model" unto its own, but is rather a verification snapshot of any time-dependent model. For the purpose of creating an intermediate prototype model, a sinusoidal temperature profile was used, which would capitalize upon periodic boundary conditions. Fig. 4-1 shows the resulting wind field from a sinusoidal temperature gradient in the meridional direction. The mean velocity (an indication of the magnitude) shows that the wind is far more responsive to the potential temperature gradient than the actual temperature value, due to the effect of *local* temperature gradients acting upon the Profile III wind flow. The wind profile is out of phase with the temperature profile and in phase with the potential temperature gradient - increasingly negative baroclinicity creates higher wind speeds. The gradient of the winds (or wind divergence) is alligned with temperature profile. The meridional gradient of the horizontal flow in Fig. 4-1 gives rise to mass/energy convergence, as derived in Chapter 3. In Fig. 4-2, the vertically integrated upstream and downstream energy fluxes indicate a buildup of energy in cells as indicated in the Q convergence plots. The vertical velocity corresponds to the meridional wind gradient, which is in phase with this curve (see Chapter 3 for derivation of the large scale vertical flow).

The energy convergence slightly leads the temperature curve which indicates two opposing effects in calculating energy convergence - the advective and divergence contributions. The advective contribution is due to the wind passing over a temperature gradient, while the divergence effect creates a "pile-up" of mass, and hence energy.

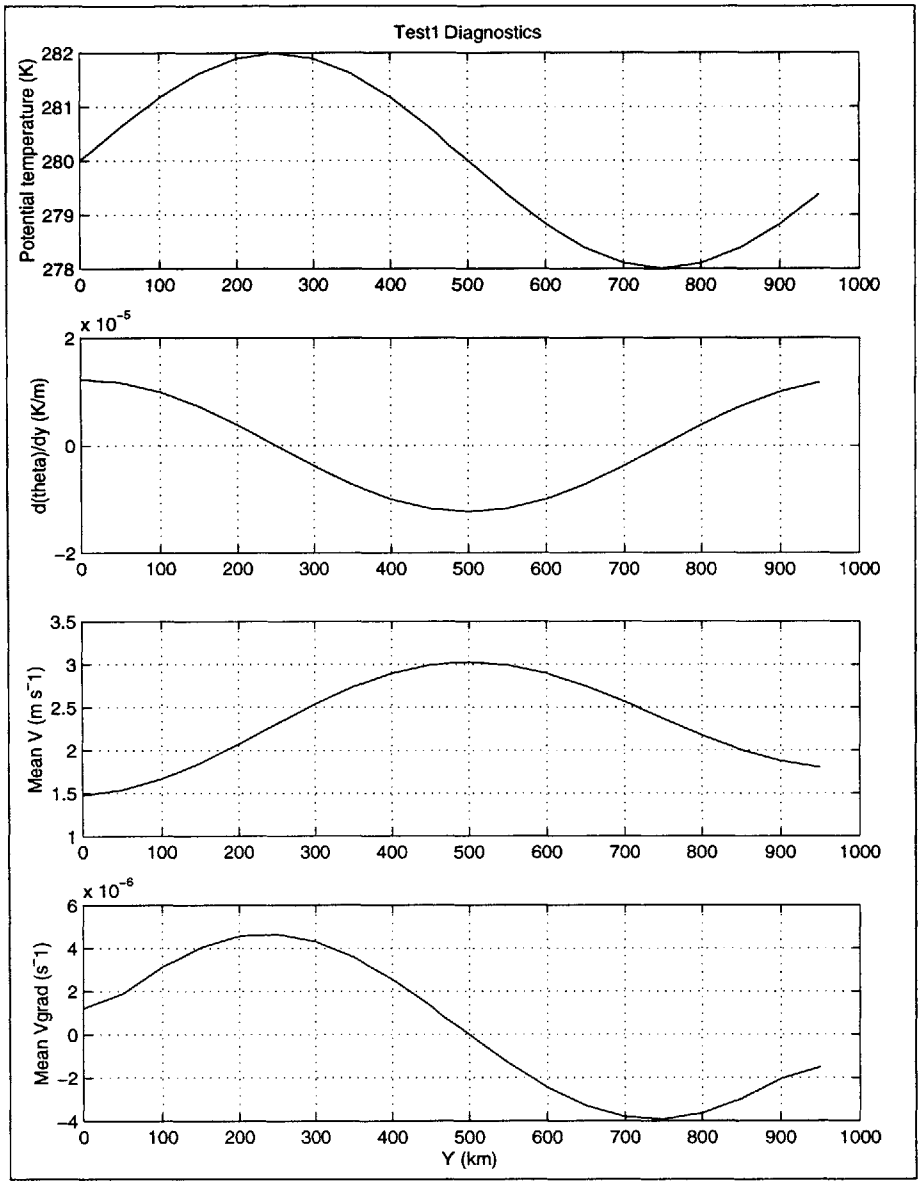

Figure 4-1: Results of initial diagnostic test showing the role of baroclinicity in producing a characteristic meridional flow field. The top plot shows the time-invariant sinusoidal temperature profile, with an amplitude of 2 K, and a wavelength encompassing the entire domain (1000 km). The corresponding horizontal temperature gradient $\frac{\partial \theta}{\partial y}$, is calculated using a centered finite difference algorithm, and exhibits the $\frac{\pi}{2}$ phase shift expected from a sine differential. Note that the temperature gradient varies over the entire range of magnitudes studied in the previous chapter. The resulting meridional wind field and divergence plots show a nearly perfect alignment with the temperature plots. Clearly, the phase of the third and fourth plots indicates the overwhelming response of the meridional flow to the temperature *gradients* as opposed to the *temperature*. The wind field and gradient are vertically averaged; their vertical profiles can be readily assessed from figures in the Profile III sensitivity analyses.

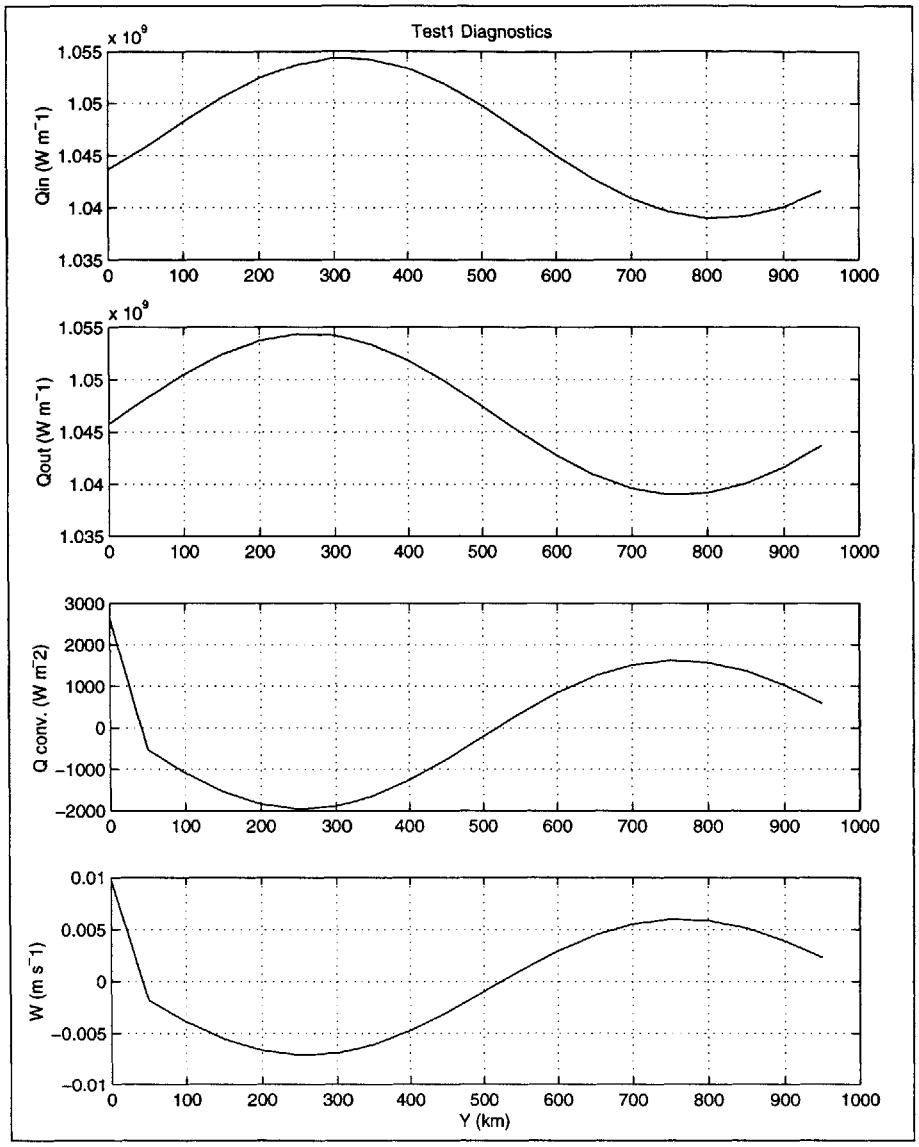

Figure 4-2: The vertically-integrated energy flux, energy flux convergence, and large-scale vertical velocity fields corresponding to the meridional wind and temperature variation in Fig. 4-1. The first plot shows the upstream (incoming) energy flux computed from the atmospheric state variables in the $i-1$th cell, while the second plot depicts the downstream (outgoing) flow from the ith cell. The cell height is listed in Table 4.3. The energy deposition created by the difference in the first and second curves is plotted in the convergence field (third plot). Where the outgoing energy flux exceeds the incoming flux, the convergence is positive (e.g. near the center of the domain). Notice that the energy convergence field leads *slightly* ahead of the potential temperature gradient curve in Fig. 4-1. This small phase shift reveals the relative magnitudes of the advective and wind convergence components of the energy flux convergence. See Fig. 4-3 for a detailed look at these components. The vertical velocity in the final plot is dependent solely upon the wind convergence, and is identical to the negative v gradient in Fig. 4-1.

Effects of Profile III parameters upon convergence partitioning

Due to the importance of convergence in energetic coupling of the LLJ, a more thorough analysis was conducted to quantify the advective and divergence contributions to the total energy convergence. From (3.30), the vertically integrated energy flux (energy per unit cross-sectional length) is given by

$$F_E = \int_{z_{sfc}}^{h} \rho c_P V dz \tag{4.1}$$

In order to compute the flux divergence, (4.1) is differentiated with respect to y and expanded according to the Liebniz rule yielding

$$\begin{aligned} \frac{\partial F_E}{\partial y} = & \int_{z_{sfc}}^{h} \rho c_P V \frac{\partial \theta}{\partial y} dz \quad (I) \\ & + \int_{z_{sfc}}^{h} \rho c_P T \frac{\partial V}{\partial y} dz \quad (II) \\ & + \rho c_P T V|_h \frac{\partial h}{\partial y} \quad (III) \end{aligned} \tag{4.2}$$

where z_{sfc} is assumed to be zero, $\frac{\partial T}{\partial y} = \frac{\partial \theta}{\partial y}$, and where term III is assumed to be zero for the purposes of the constant boundary layer tests.

The response of each of these terms is reported in Fig. 4-3, which shows a snapshot of the total convergence, the contributions to convergence, as well as the compensating energy entrainment flux, which is computed according to the large-scale vertical velocity and the potential temperature inversion strength. The magnitude of the energy convergence field in Fig. 4-3 is quite large, and overwhelmingly responds to term II (the divergence term). Further study of this seemingly anomalous convergence pattern was discovered to be the result of the Profile III exponential scaling factor, which directly determines the relative strength of terms I and II in (4.2). The scaling factor z_{scl} not only influences the meridional wind with other constant parameters, but it also modifies the sensitivity of the profile to baroclinic conditions. Paradoxically, a large scale height creates *less* sensitivity to changes in the *shear* of the local-scale winds. (Obviously, U_{g0}^{SS} would have the opposite trend). Hence, large values (e.g. $> 10^4$ m) of z_{scl} cause the upper level winds to dominate over sensitivity to

local gradients. The absolute magnitude of v is increased, and the wind gradient is decreased, because local temperature gradients are drowned out by winds aloft. The components in Fig. 4-4 verify this property. Both of these factors increase the relative importance of Term I (advective component). Conversely, smaller values of the scale height cause the second integral to dominate. Throughout the following studies, the scale height explains seemingly reversed convergence patterns where z_{scl} has been modified.

Meridional wind and flux profiles from a linear temperature field

A diagnostic study of the Profile III flow was made over a linear temperature domain, primarily because this profile more closely resembles the gradual temperature gradients encountered over the Great Plains, in the absence of intersecting frontal boundaries. The potential temperature gradient from such a profile is constant (see Fig. 4-5, which causes the wind field to vary little over the domain. The small sensitivity which the meridional flow *does* have with respect to the actual potential temperature values is evident in the weak signal in both the mean wind and gradient profiles. The energy flux profiles in Fig. 4-6 show the slight energy convergence which is confirmed in the third frame. The non-periodic boundary conditions are evident as well, with the zero values at the edges of the convergence field and in the vertical velocity field.

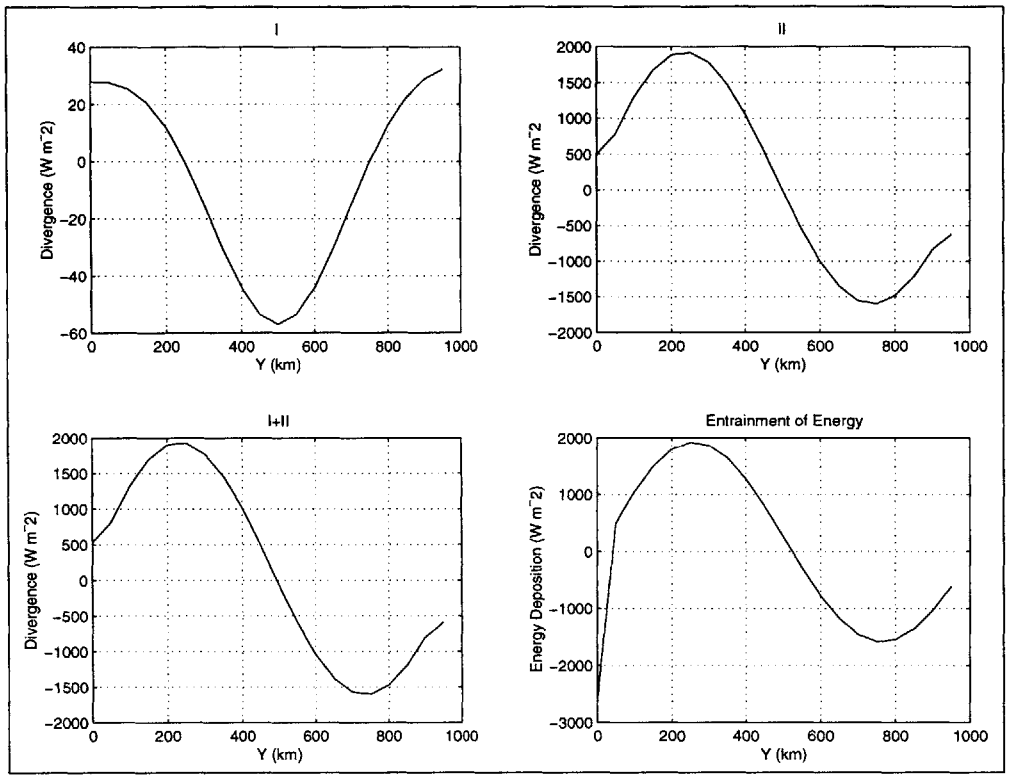

Figure 4-3: The relative magnitudes of the energy flux divergence components in (4.2). The first plot (I) shows the contribution to the energy divergence arising from the advective component of the Liebniz expansion of the flux differential. Note that this plot is in phase with the negative of the potential temperature gradient field and meridional wind fields in Fig. 4-1. Plot (II) depicts the energy convergence due to mass accumulation in a cell, caused by divergence in the wind field. As expected, this component is $\frac{\pi}{2}$ out of phase with the advective (I) contribution; the amplitude of this plot is an order of magnitude less than that of (I). The total (excluding meridional mixed-layer height variation) integrated flux divergence is shown in the third frame, indicating that term (I) greatly overwhelms the contribution of (II). However, term (II) produces enough of an impact to cause a slight shift in the convergence field of Fig. 4-2. Under the constraint of mass conservation, component (II) must be compensated by an equal and opposite flux into the cells through additional entrainment, as calculated in (3.10).Here, note that these results are contingent upon the value of $z_{scl} = 2000$ m.

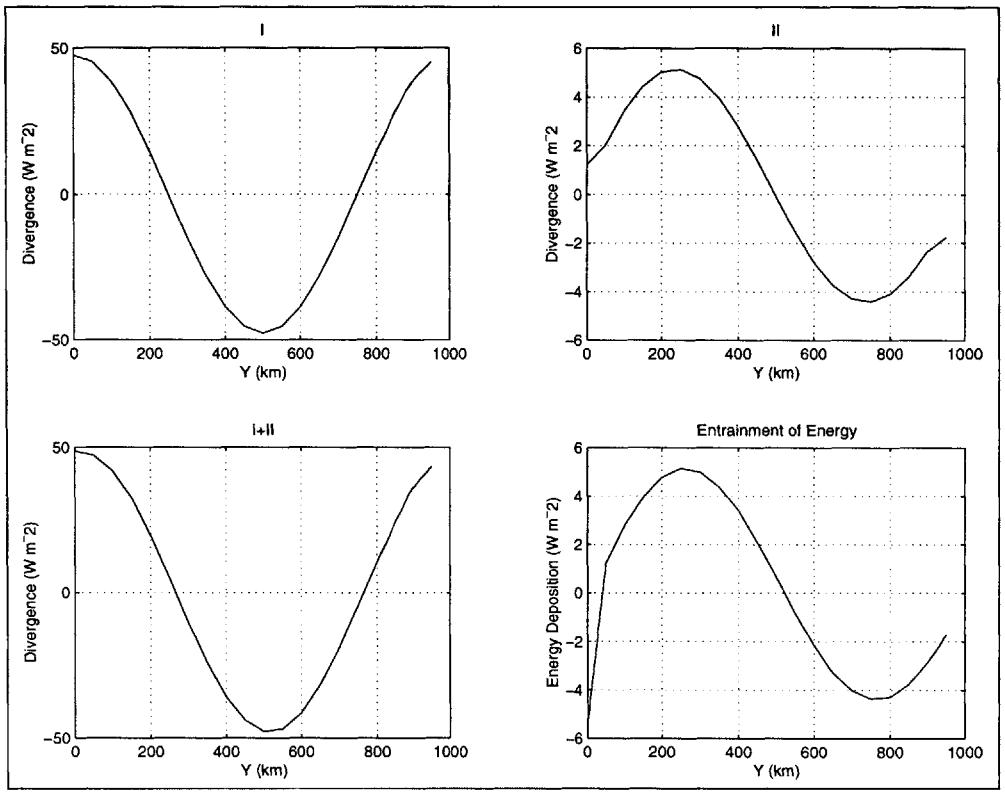

Figure 4-4: The relative magnitudes of the energy flux divergence components in (4.2), with an extremely high scaling factor (2E6 m). As in Fig. 4-3, the first plot (I) shows the contribution to the energy divergence arising from the advective component and plot (II) depicts the mass accumulation contribution. Note the much smaller magnitude in the mass accumulation term, and the larger magnitude in the advective term compared to Fig. 4-3. The relative strengths of the terms is directly linked to the Profile III scaling height. See text for details.

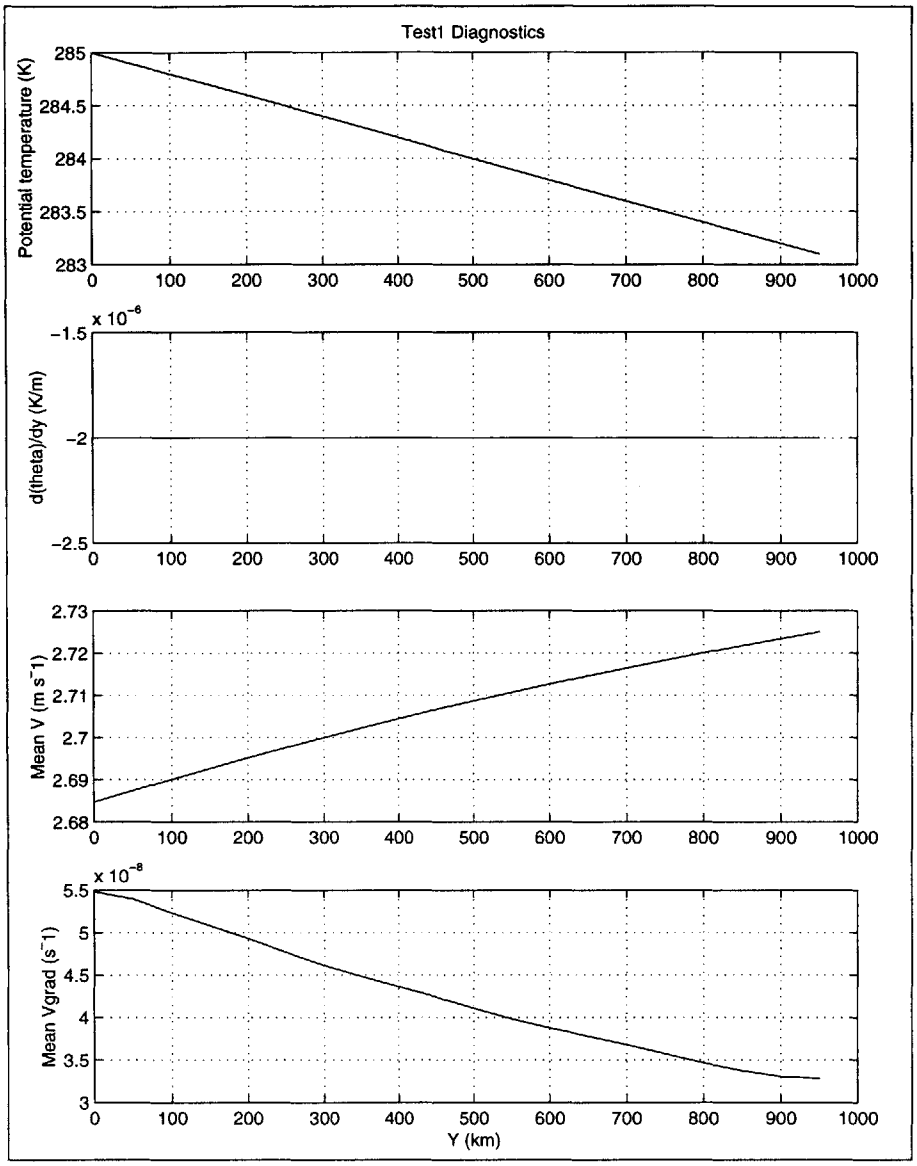

Figure 4-5: The meridional flow pattern associated with a linear temperature profile. The first and second plots show the potential temperature and temperature gradient fields which are used in modeling the synoptic conditions associated with the LLJ. The magnitude of the wind field variation in the third plot is negligible, as is expected with nearly constant local baroclinicity. The wind field and wind gradient each respond trivially to the temperature variation in the first plot, due to the explicit temperature parameter in the geostrophic wind shear.

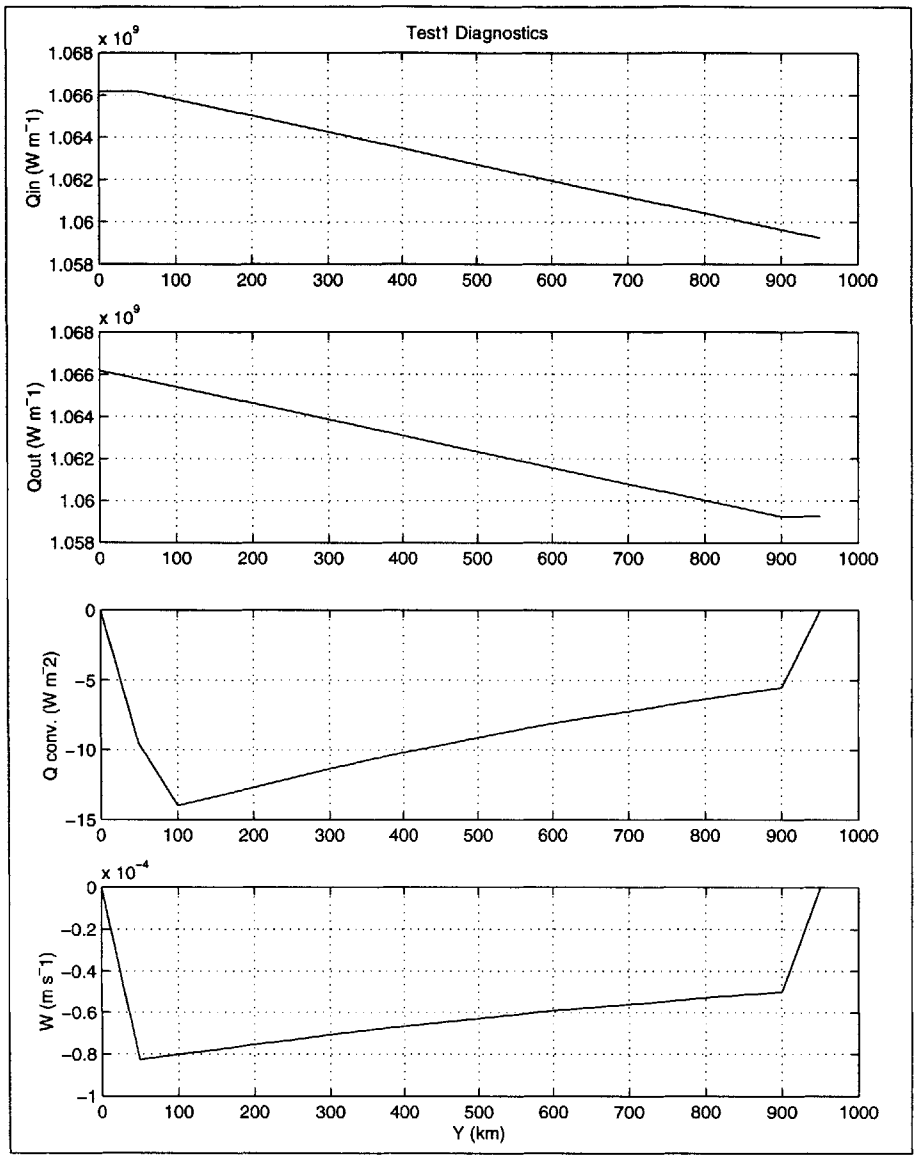

Figure 4-6: Energy deposition and vertical velocity compensation derived from the state variables in Fig. 4-5. The upstream and downstream energy fluxes exhibit a zone of no variation due to a non-convergence constraint at the upstream and downstream boundaries. Like the potential temperature and wind fields, the convergence is nearly constant with respect to y, with the exception of the constrained boundaries. The vertical velocity in the final frame compensates for the small accumulation of mass caused by wind divergence, but is negligible in magnitude due to a nearly constant meridional flow field.

4.3 Energy feedbacks in a time dependent model: Test 2

4.3.1 Description of model

The second prototype model implemented for this thesis was a time-dependent 2-D model, with temperature as the only model variable with a non-zero tendency equation. The potential temperature in each mixed-layer cell was governed by shortwave radiative heating (forcing), longwave radiative cooling (damping), convergence, and entrainment. The cooling from infrared emission in the test 2 model is computed according to the Stefan-Boltzman relationship governing "gray-body" radiation

$$R_{sd} = \epsilon \sigma T^4 \tag{4.3}$$

where T is the equilibrium emission temperature, ϵ is the atmospheric emissivity, and $\sigma = 5.67 \times 10^{-8}$ W m^{-2} K^{-4}. Incoming radiative forcing is provided by an empirical "S_0" which merely has been designed to create a radiative balance at the center of the meridional domain given the latitude and radiative cooling at that point, with an intended steady-state temperature. It is assumed that the atmosphere absorbs the incoming shortwave radiation as a slab - there are no effects of surface heating. The temporal variation of the radiative forcing is governed by a simple sinusoidal relationship, with sunlight only occurring between 0600 LST and 1800 LST as a first approximation. The effective shortwave forcing constant is thus given by:

$$S_0 = \frac{\epsilon \sigma T^4 \pi}{\cos \phi} \tag{4.4}$$

The actual values (in each of the tests) of the effective shortwave constant and the emissivity are found in Table 4.3. The change in temperature due to entrainment is calculated as stated in Chapter 3, using the potential temperature inversion strength parameter, and the large-scale vertical velocity. As shown in Fig. 4-3, the mass accumulation (divergence) portion of the energy convergence field is

mostly compensated by the energy entrainment. In order to reduce the amount of noise in the model, a running average smoothing algorithm was used to filter the potential temperature gradient and energy convergence fields with a rectangular (equal-weighting) bandwidth of 3 points. A horizontal resolution was chosen at dy=50 km, and dt=200 s, so that adequate stability was imposed. It remains unclear whether this resolution is too large to adequately determine the effects of surface heterogeneity upon atmospheric phenomena at the meso- or synoptic-scale.

4.3.2 Test 2 under sinusoidal spatial temperature field

Advection of potential temperature anomaly in meridional flow

The first trial run using the Test 2 setup studied the advection of temperature anomalies in the meridional domain. For the first preliminary trial, periodic boundary conditions were utilized, and the temperature gradient was also computed using a "wrap-around" approach. The prototype model was initialized with a sinusoidal temperature gradient, with ensuing diagnostic variables at the start of the Test 2 run, which are shown in Fig. 4-7.

The energetics plot in Fig. 4-8 shows the dominant convergence pattern (using a scale height of 2000 m under Profile III). The radiative cooling is aligned with the temperature gradient. The radiative heating (forcing) is dictated by the time of day; since the initialization is taken at midnight, the forcing is initially zero everywhere. The vertical velocity is about 1 cm s^{-1}, a value not uncommon for large-scale values. If the scaling factor were increased, both the convergence and vertical velocity profiles shown in Fig. 4-8 would be much reduced. The remaining diagnosed variables in Fig. 4-9 show the compensating energy entrainment (in response to horizontal wind convergence acting within mass continuity constraints) and overall trend in the temperature peak as it advects. The wind blows left to right, across the gradient of the temperature profile. The tendency shows that, as expected, the wave-form propagates to the right; the total heat transfer reflects both the advection and damping of the temperature profile. After the Test 2 model was run for 0.5

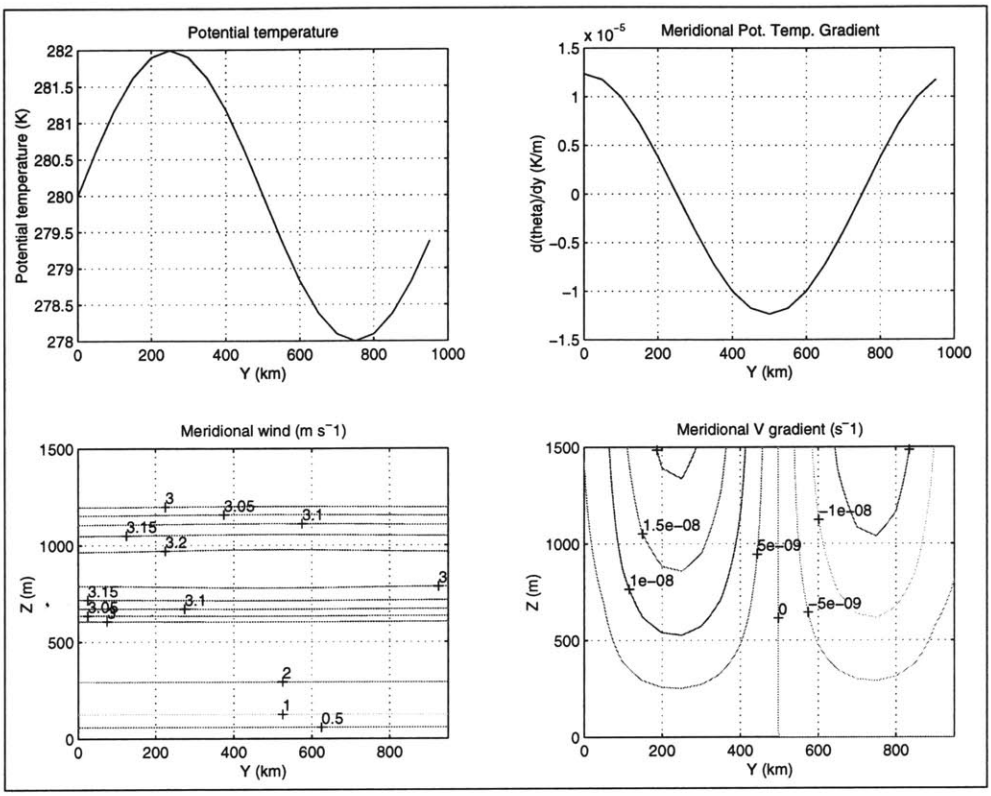

Figure 4-7: Test 2 initialization with sinusoidal temperature profile and periodic boundary conditions. The entries here are identical to the test 1 diagnostics in Fig. 4-1, except for full cross sections of the meridional wind and gradient fields. The V contour plot has been enhanced with arbitrary contours to reveal the slight but noticeable change in the meridional wind, as shown in the 3.2 m s^{-1} contour "bulge" in the center of the domain. Note that the maximum magnitudes of the meridional wind gradient occur at the *top* of the mixed-layer, while the maximum magnitude of the meridional wind occurs at some intermediate level, say, 850 m. This disparity is explained in Fig. 3-11, where the V-sensitivity to small-scale temperature gradients is maximized at a level somewhat higher than the LLJ height.

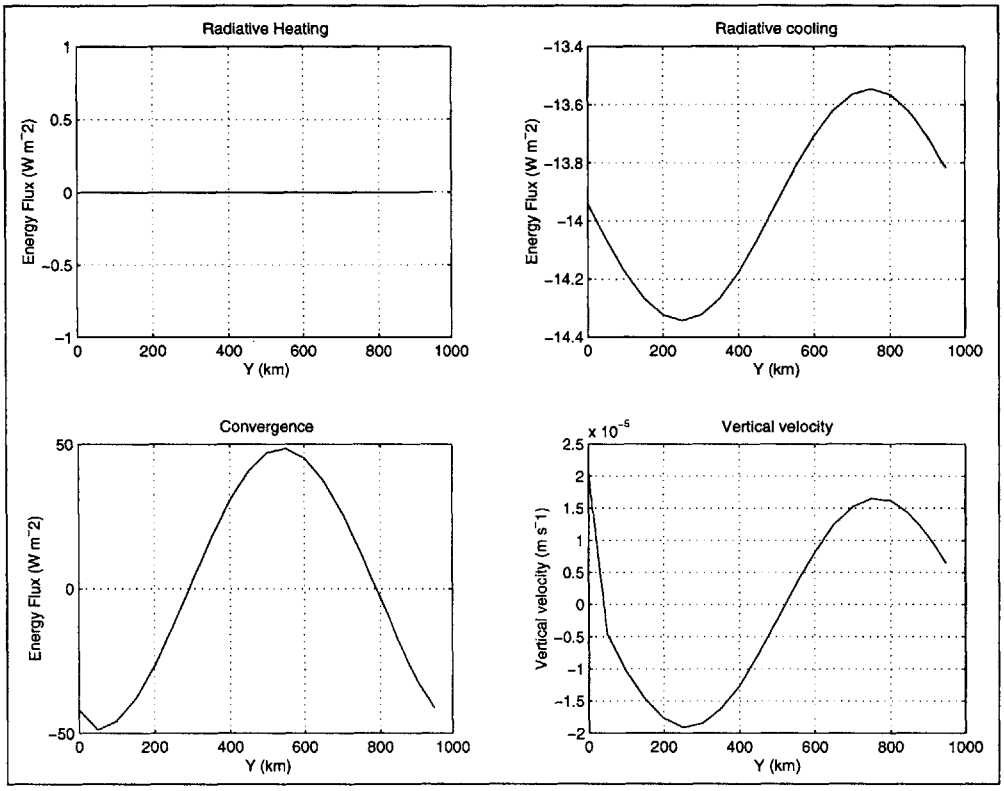

Figure 4-8: Test 2 initial energetics and vertical velocity. This initialization is at midnight, when the radiative heating is zero throughout the domain. Radiative cooling, as a function of temperature is governed according to the Stefan-Boltzman relationship in (4.3), and mirrors the behavior of the temperature plot in Fig. 4-7. Note that under Profile III wind field, the deposition of energy due to convergence is stably aligned with the temperature field (by deamplifying the signal) as opposed to Profile II winds, which had the opposite effect of amplifying temperature anomalies in Fig. 3-5.

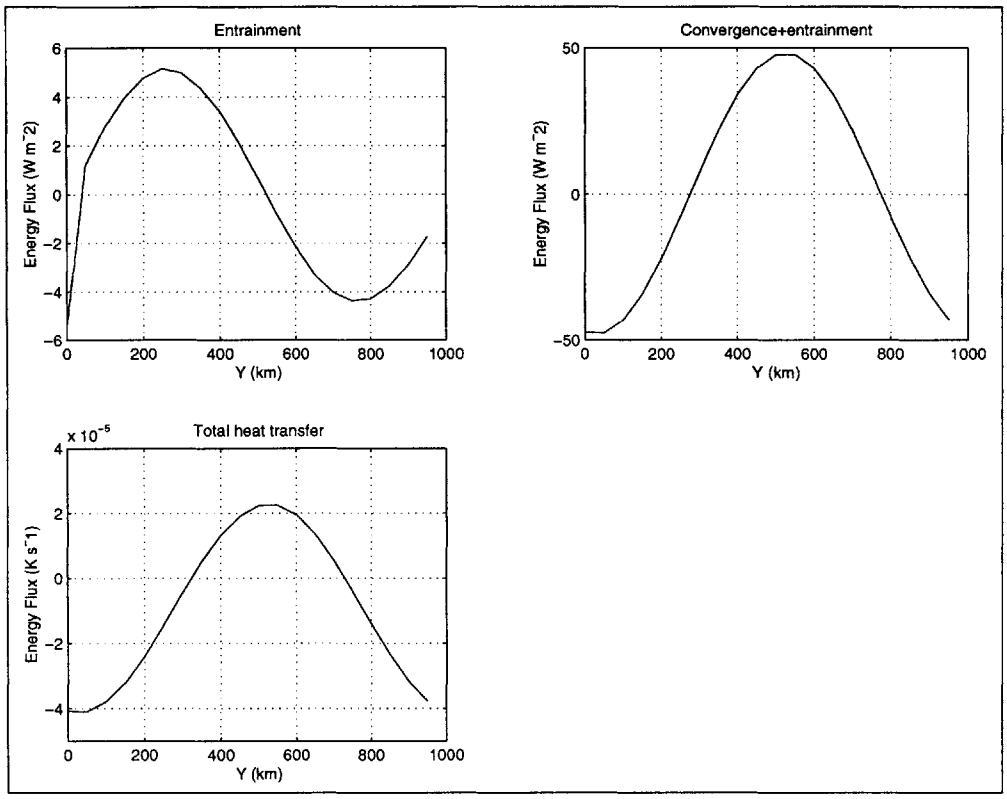

Figure 4-9: Test 2 initial entrainment of sensible heat, residual convergence from advection, and total heat transfer. The entrainment flux is parameterized according to (3.10) with regard to the vertical velocity. The advective component in frame 2 shows the tendency of the potential temperature spike downwind, which advects the peak through time. The peak should de-amplify for 6 hours before sunrise, and then change according to both radiative heating and cooling after shortwave forcing begins. The total heat transfer is dominated by the energy convergence with a downward shift from the nearly constant radiative cooling.

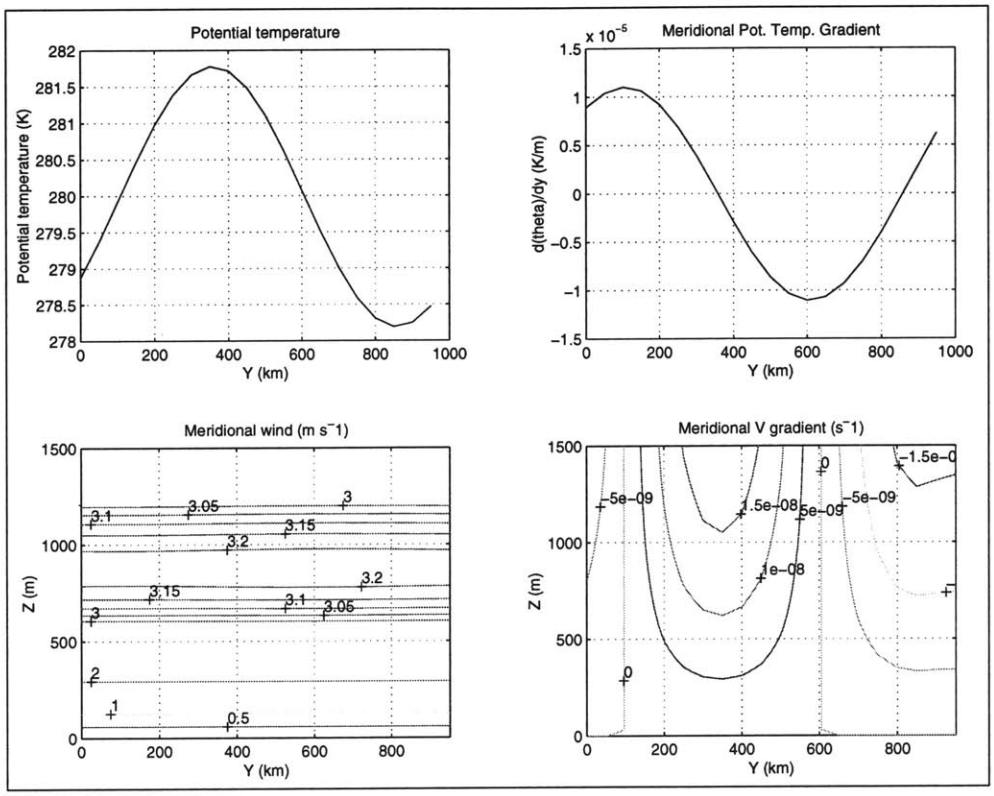

Figure 4-10: Test 2 snapshot after 0.5 days. As predicted in the tendency plots in Fig. 4-9, the potential temperature signal has de-amplified by .25 K and propagated downwind 100 km through advective transport. The meridional wind and wind gradient both exhibit the new position of the temperature extrema.

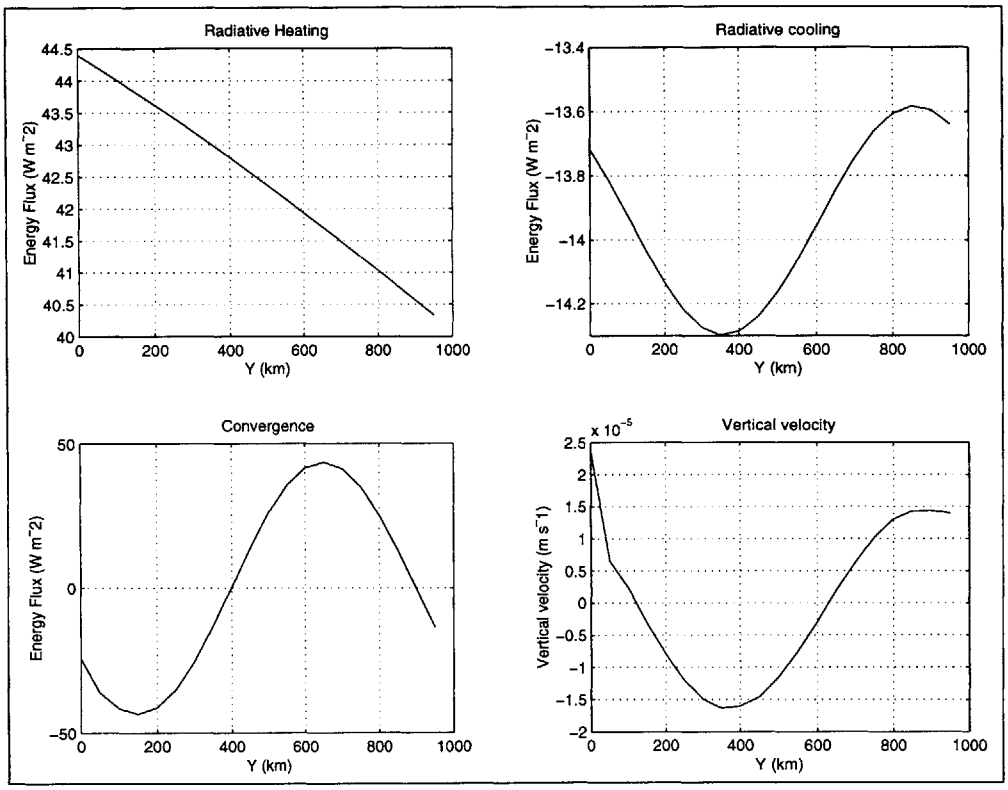

Figure 4-11: Test 2 energy forcing and vertical velocity after 0.5 days. The shortwave incoming radiation is weighted according to latitude, and is formulated in (4.4). This frame shows the temporal maximum of radiative forcing. The vertical velocity, convergence, and radiative cooling fields have each de-amplified in proportion to the decrease in strength of the temperature signal.

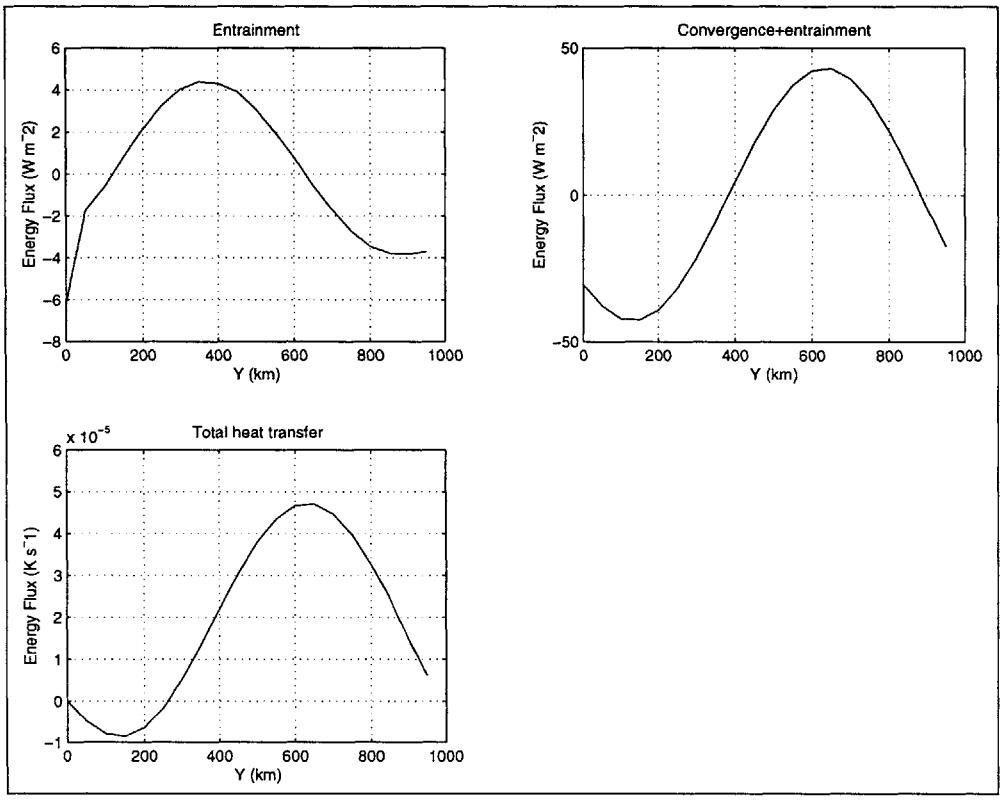

Figure 4-12: Test 2 tendency and energetic terms after 0.5 days. The frames verify the decrease in vertical velocity (in the case of the entrainment), and similar temporal changes in the convergence and tendency profiles.

days, the temperature profile propagated as expected from the tendency plots in prior figures. The potential temperature profile in Fig. 4-10 has propagated downstream from its previous position, and the meridional winds have shifted accordingly. Due to the radiative damping of the the temperature profile, the amplitude of the sinusoidal field has been reduced by .25 K. The propagation speed of the wave is the same as that predicted by meridional winds at the surface, or 3 m s^{-1} as expected from the vertical average of the northward flow. The radiative forcing in Fig. 4-11 exhibits the temporal maximum in shortwave flux, which is dependent upon the cosine of the latitude (noon LST is the time of greatest shortwave forcing). The radiative cooling (damping) of the system depends upon the temperature profile, and continues to dampen the gradient, and hence the wind field.

Shortwave forcing does not significantly alter the wind field under the sinusoidal conditions, due to the lack of correlation between the profiles in time and space. In response to the dampening of the temperature profile, the radiative cooling in Fig. 4-11 also has decreased in amplitude. The energy convergence continues to show the direction of propagation (downwind) of the temperature profile. In light of the scaling parameter used here (see Fig. 4-4), the vertical velocity is quite minimal. As a result, the entrainment flux in Fig. 4-12 also is very small, and compensates the divergence term of the Liebniz convergence expansion in (4.2). Also from Fig. 4-12, it is apparent that the convergence is primarily composed of the advective component, and that the total heat transfer is also in phase with the convergence+entrainment plot. Modified by diurnal radiative forcing, potential temperature advection dominates the total heat transfer as well, showing the translation of the temperature curve through time.

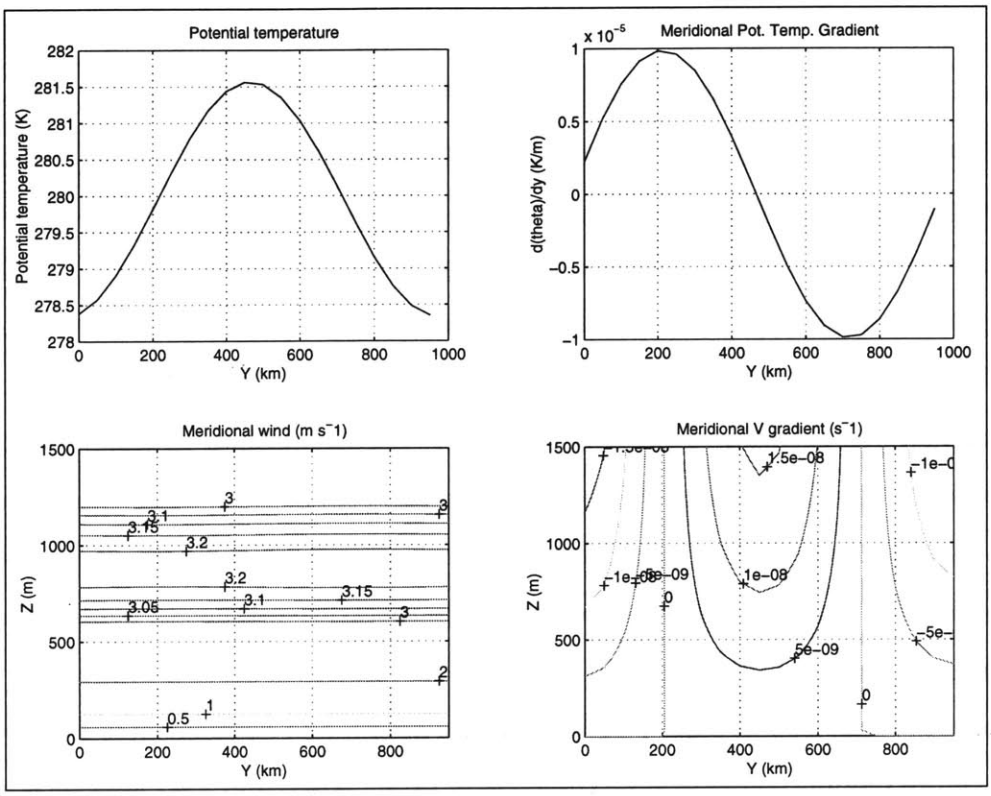

Figure 4-13: Test 2 snapshot of temperature and winds after 1.0 days. In a continuing sequence from Fig. 4-7 and Fig. 4-10, the potential temperature has become more flat, due to selective radiative cooling. Radiative heating does not amplify this wave appreciably due to its time-invariant latitudinal dependence. The propagation speed continues to be on the order of the velocity profile in the third frame, and the temperature peak has continued another 100 km downwind during one diurnal cycle. Because the radiative forcing has been designed to balance longwave emissions, the spatial mean of the potential temperature field has changed little. A comprehensive time series in Fig. 4-16 illustrates the radiative balance over longer intervals.

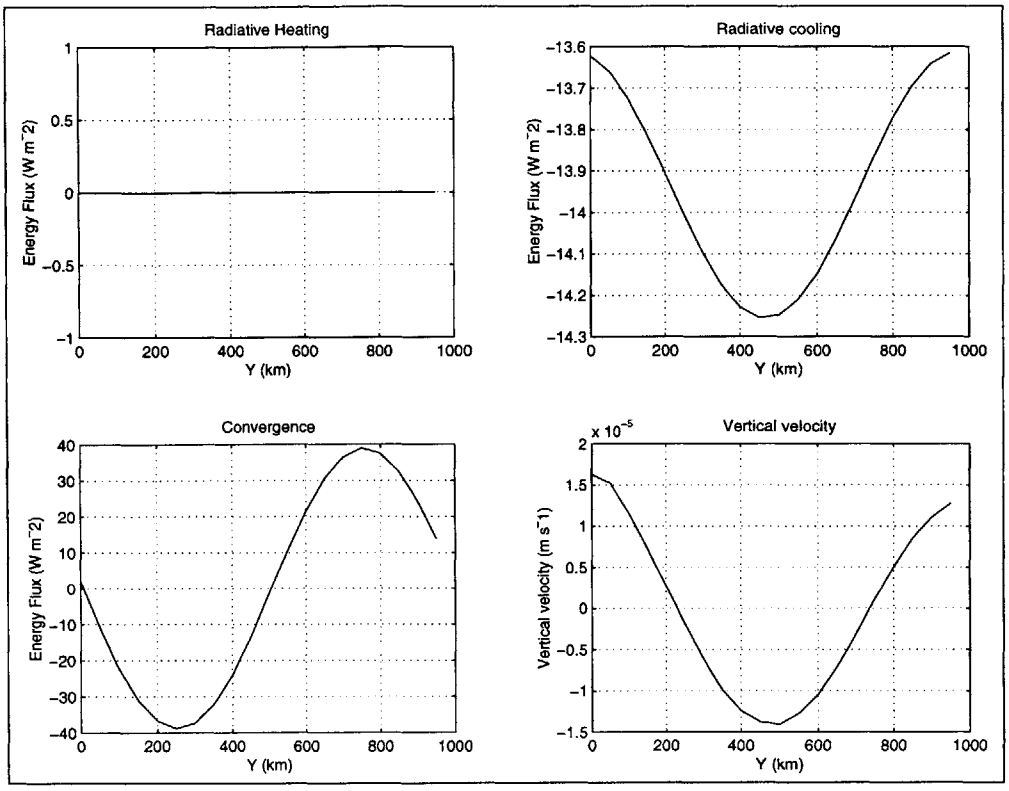

Figure 4-14: Test 2 snapshot of energy deposition and vertical velocity after 1.0 days. A change in these fields has occurred in response to a weakening temperature signal. At this time (midnight LST), the radiative forcing has returned to zero again, which completes the first diurnal cycle. Note that previously analyzed phase trends continue at the end of the diurnal cycle.

At the conclusion of the diurnal cycle, the temperature profile has translated downwind, as shown in Fig. 4-13, and the amplitude of this profile has again been reduced by about .25 K. The wind continues to show a quite reduced sensitivity to the potential temperature gradient, which is due to the selection of the scaling parameter used for this study. The meridional v gradient also remains quite small, resulting in trivial mass-accumulations throughout the domain. At midnight (LST), the Test 2 radiative heating term is identically zero. The convergence field has decreased in proportion to the decrease in the meridional temperature gradient, due to reductions in the wind velocity and potential temperature gradient. The vertical wind velocity is weak, due to a weak divergence term in the energy convergence. In Fig. 4-15, the

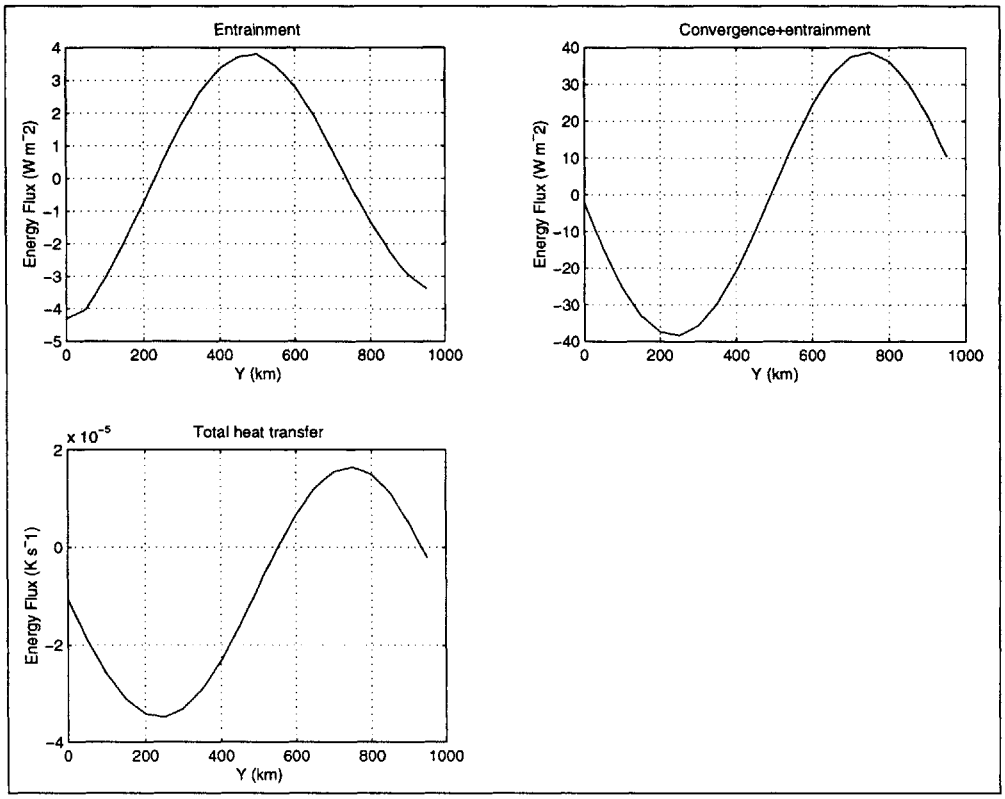

Figure 4-15: Test 2 tendency and energy deposition terms after 1.0 days. The profiles continue to reflect both the movement and decay of the temperature field. See Fig. 4-9 and Fig. 4-12 for details on the phase and amplitude relationships between the various plots.

entrainment has markedly decreased since the 0.5 day snapshot, indicating a bulk decrease in the gradient of the meridional wind. The total heat transfer is becoming increasingly dominated by the radiative cooling, meaning that the damping of the temperature profile becomes dominant in the tendency equation rather than the advection of temperature. This finding is corroborated by the time series analysis which follows in the next section.

Superposition of radiative forcing and advective processes

Analysis of Test 2 output in the snapshot figures revealed two phenomena which affected the temperature profile in time and space. As noted in the potential temperature plots just discussed, an *advective* process acts to transport the temperature field through space at a rate similar to the mean wind velocity, since "advection" in the Test 2 model is simply the result of air exchange between cells. In turn, the vertically-integrated flux is approximately the mean wind times the mean temperature in the layer. The second process which dominated the energetics of the Test 2 simulation was the diurnal energy cycle. The continual cooling of the mixed-layer is marked by spatial variability correlated with the temperature field, but a generally low temporal variability due to the small absolute changes in temperature at a point. The radiative heating, however, shows only slight spatial variability (according to rather small shifts in latitude) while exhibiting a very pronounced and consistent temporal evolution over the daily cycle. A time series of 20 days was constructed to analyze the evolution of a temperature field in the presence of both of these effects. Using the same initialization as in Fig. 4-7, the Test 2 model was run using the same parameters. A time series plot of the relevant energetics was constructed, to determine the impact of advective and radiative processes. Fig. 4-16 shows the potential temperature, temperature gradient, energy convergence, and meridional wind at a point in the center of the domain. The temperature profile is clearly influenced by both effects. This signal shows a large amplitude component with a smaller frequency overlaid with a high frequency diurnal oscillation of small amplitude. The advective process determines the larger "envelope," as the

sinusoidal temperature profile translates through the meridional domain. The small frequency signal is composed of a heating and cooling component, corresponding to the radiative forcing and damping. Because the radiative cooling is not spatially and temporally correlated with the passage of the temperature profile, the advection signal is eventually damped out and an equilibrium emission temperature is attained. The diagnostic fields produced from the temperature profile, however, only respond to the advective process rather than the diurnal cycle, except through the radiative cooling dampening the signals in all three cases. The potential temperature gradient is not affected, for example, by the shortwave radiation due to its lack of spatial correlation. Consequently, the remaining gradient-dependent fields (convergence and winds) also do not show a response to diurnal variations.

4.3.3 Test 2 with linear temperature profile

After the completion of Test 2 sinusoidal runs, the prototype model was initialized with a more realistic, gradually sloping linear temperature profile to more closely approximate the large-scale conditions over the Great Plains. The initialization of this brief study is shown in Fig. 4-17, where the temperature ranges from 285K to 283K over 1000 km. The potential temperature is essentially constant, with some exaggerated truncation error shown in the figure. The meridional wind speed shows only the slightest change with respect to y, as the potential temperature gradient does not vary meridionally. As opposed to the sinusoidal case, the linear model run is determined more strongly by the diurnal radiation balance than by advection, as the shortwave forcing and cooling both will affect the temperature gradient (and hence the winds), whereas in the sinusoidal run the temperature and radiative forcing are not so well correlated and hence do not form strong energetic feedbacks.

The relationship between the advective and radiative forcing is seen more clearly in Fig. 4-18, which shows the potential temperature, temperature gradient, energy convergence, and meridional wind. In contrast to Fig. 4-16, each plot shows some visible effects of both the advective and diurnal energetic processes. At the time of initialization, the linear profile is actually an effective peak with a local maximum at

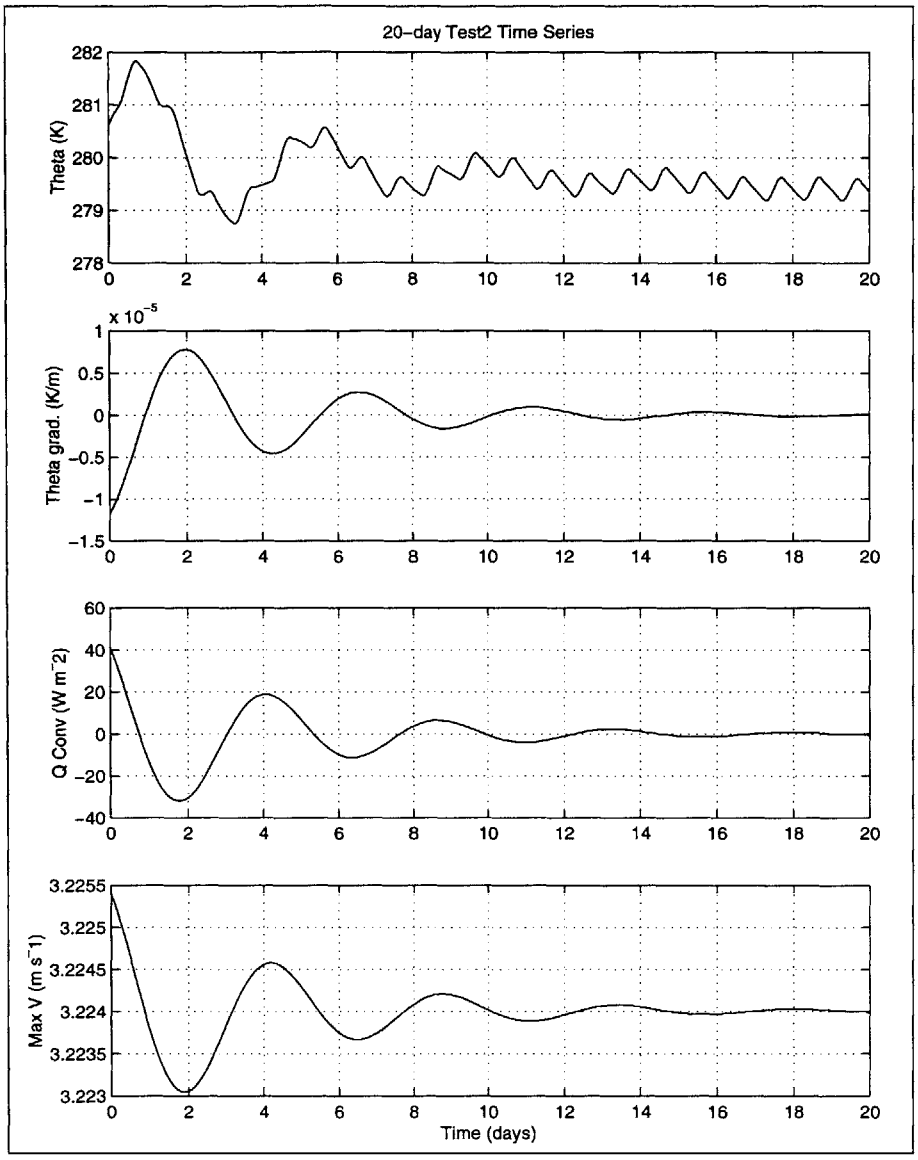

Figure 4-16: Test 2 time series through a 20-day period, taken at the center of the domain. The potential temperature, temperature gradient, energy convergence, and meridional wind frames exhibit two independent temporal processes. First, radiative forcing imposes an *almost* spatially uniform diurnal heating cycle, which causes the high frequency/low amplitude oscillation in the temperature field (frame 1). In addition, the temperature field also shows the effects of a propagating and damping spatial wave. The lower frequency oscillation arises from the propagation of spatial temperature pulse through the domain, which gradually de-amplify. This process is described in prior snapshot figures. The equilibrium value of the temperature is determined by radiative balance. The other three frames, in contrast, only exhibit the advection of the spatial wave and not the diurnal oscillation. The temperature gradient (and its dependent fields such as flux convergence and wind speed) responds only to spatially variable forcing. i.e., anomalies in the radiative forcing forcing field are not correlated with pulses in the spatial domain.

the left of the domain. Any temperature above the equilibrium emission value acts as a warm anomaly, even though the linear profile is continuous and of constant slope. The effective temperature peak starts at y=0 and propagates past the point y=10, where the time series is taken.

In the top frame, the potential temperature starts near the equilibrium. A warm anomaly is seen moving past the point y-10 after 3 days have elapsed. As the peak moves past, the meridional temperature profile has actually adjusted to the more shallow slope imposed by the shortwave latitudinal dependence. So, not only does the temperature itself equilibrate, but so also does its gradient. This gradient adjustment is seen in the 2nd frame of Fig. 4-18, where the slope starts at a magnitude well-above the equilibrium value - the peak moves past, and the gradient is permanently adjusted. In contrast to Fig. 4-16, the gradient and gradient-derived fields begin to show diurnal dependence, because now the radiative forcing is positively correlated with the temperature field, both spatially and temporally. This was not the case in the sinusoidal case. The convergence and winds both show the same adjustment process, with a small but noticeable diurnal forcing in their signals.

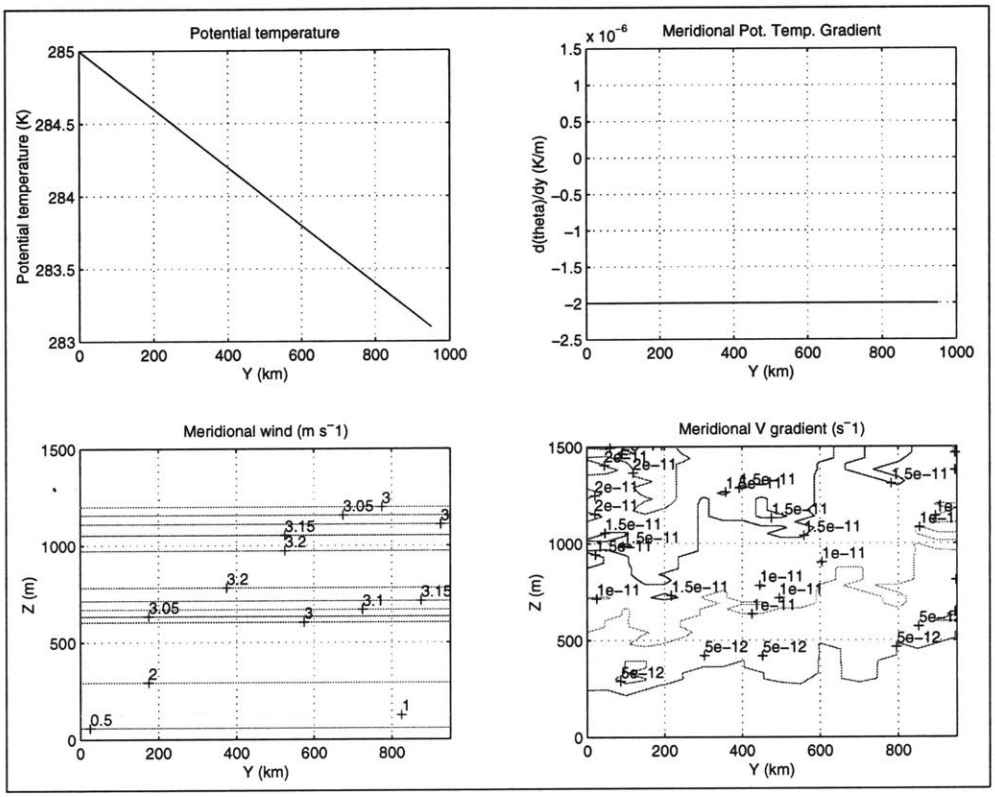

Figure 4-17: Test 2 snapshot at the time of initialization. Note that the temperature profile in frame 1 actually is an effective "pulse" since it exceeds the equilibrium mixed-layer temperature at the edge of the domain, which is an unstable arrangement and creates a pulse which propagates through time.

4.4 Passive vapor transport: Test 3

4.4.1 Analysis of vapor transport over a 1-day cycle

Using the 2-D prototype model in Test 2, the transport of moisture is tested on a domain with energetic feedbacks. The model run is identical to the Test 2 case with the linear temperature profile, which revealed the role of advection in gradient equilibration, and the imposed diurnal cycle. These same effects are again displayed, with water vapor acting as a passive admixture. The initialization of the model run is shown in Fig. 4-19, where the potential temperature, is ready to "restore" to a more uniform state, as evident in the energy convergence field. In Fig. 4-20, a specific humidity spike has been arbitrarily initialized. Moisture is allowed to advect horizontally between cells, with a sink arising from vertical entrainment induced by large scale divergence and vertical velocities. The specific humidity has no influence on the wind structure, and there are no feedbacks possible between the moisture profile and horizontal flow. The specific humidity peak advects downstream, as shown in the vapor convergence field. (See Fig. 4-21.) The "entrainment" plot, though showing positive values, actually represents a sink - this variable is actually a measure of the bulk water vapor transport into the cell. The final initialization plots in Fig. 4-22 show both the temperature equalization and the convergence-dominated tendency of the specific humidity. The wind field shows a slow but steady increase with increasing y to the north.

After one day (432 time steps) from the initialization, the specific humidity peak has begun to propagate downwind, while the temperature and temperature gradient profiles equilibrate, as shown in Fig. 4-23. Due to the scaling parameter used in the Profile III flow for this model run, the convergence is fairly sensitive to truncation error, and even the smoothing algorithms failed to completely filter high frequency noise. Comparing Figs. 4-20 and 4-24, the specific humidity peak has moved downstream. A steady state value of the specific humidity has been reached at the far left of the plot, as a result of the no-convergence boundary conditions imposed by the model. The peak of the humidity has likewise moved to the north in response

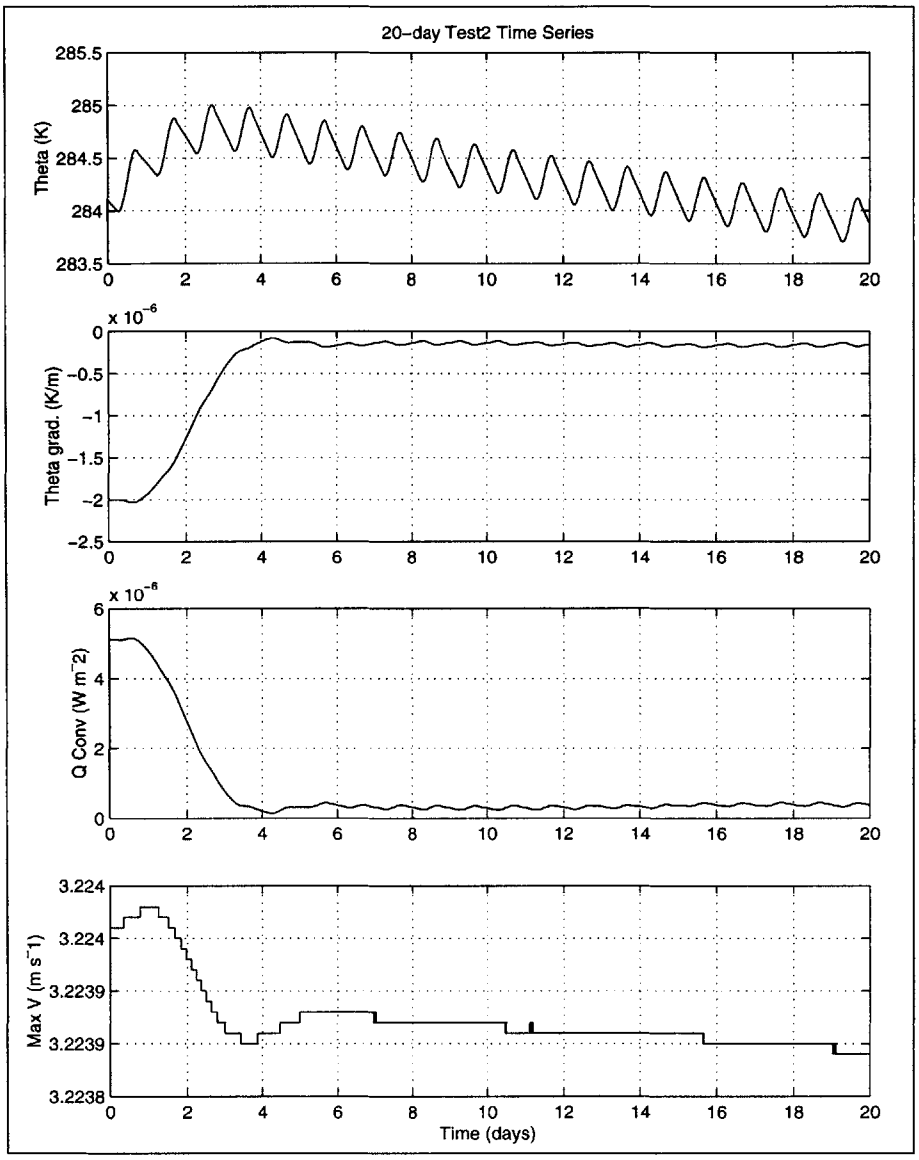

Figure 4-18: Test 2 model run over 20 days, with the linear temperature profile initialization. The time series is plotted for y=500 km. The potential temperature plot in the first frame shows the superposition of two independent signals. First, the diurnal oscillation due to radiative forcing is readily apparent as a high frequency sinusoid. The wave "envelope" is due to the spatial equilibration of the temperature profile with respect to radiative transfer. i.e., the purely linear temperature profile overshoots the equilibrium temperature at the southern boundary, as the shortwave forcing is anchored at the center. Therefore, the start of the model produces a small pulse which decays through time as the potential temperature begins to conform to an equilibrium both spatially and temporally. The temperature gradient, convergence, and winds do not depend lack the high-frequency oscillating pattern of the temperature profile at the beginning, but later exhibit this pattern after the temperature gradient has equilibrated to the shortwave forcing profile.

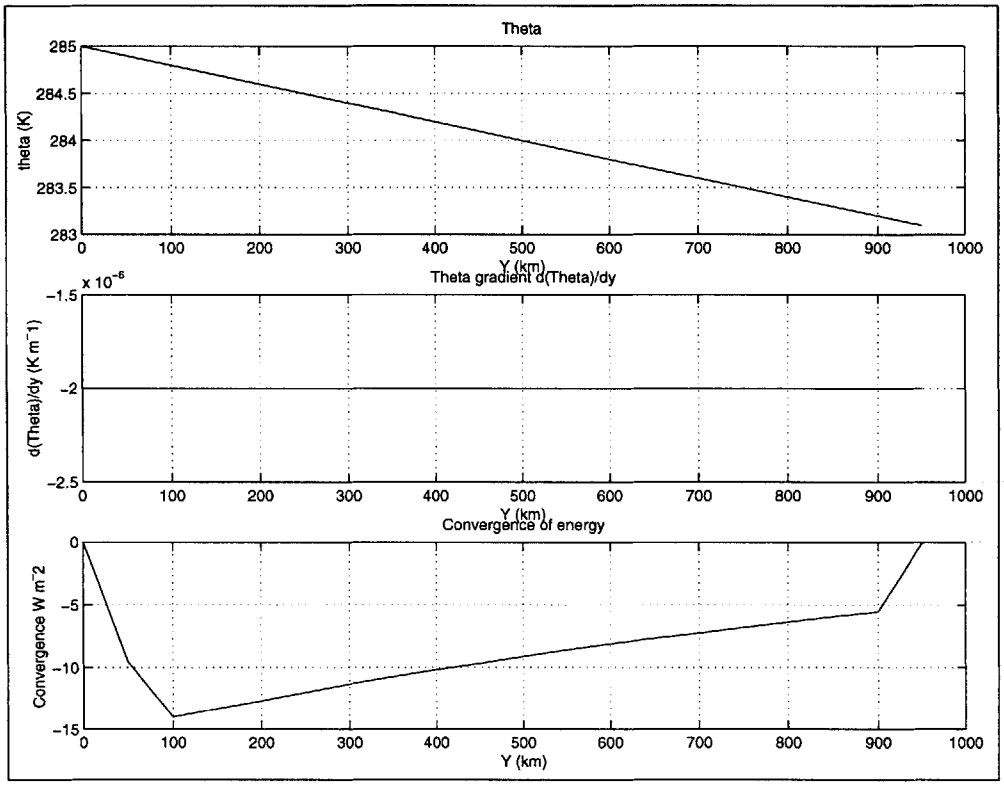

Figure 4-19: Test 3 initialization, with a linear temperature profile. The purpose of this experiment was to test the transport of water vapor as a passive admixture. The gradient and convergence are both similar to previous Test 1 and Test 2 setups.

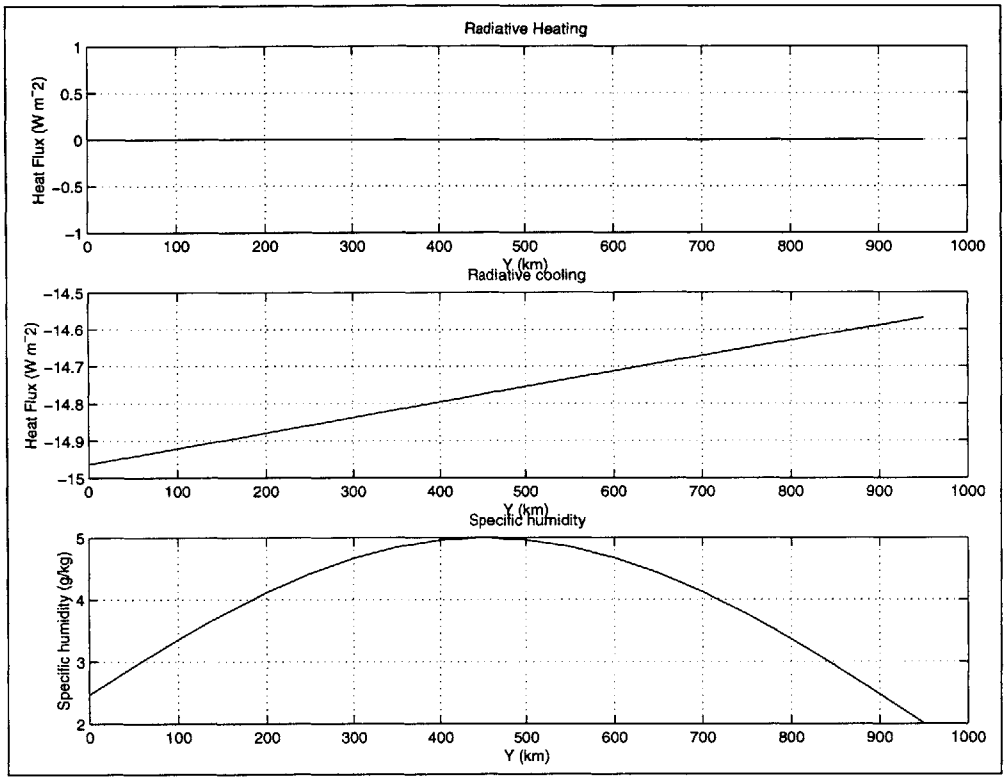

Figure 4-20: Test 3 initial derived parameters under a linear temperature profile. This snapshot is taken at midnight LST, so the radiative heating is zero. The radiative cooling curve mirrors that of the temperature profile in Fig. 4-19. In order to test the transport of water vapor under an energetically-coupled meridional flow, a characteristic "peak" was implemented, which might be physically caused by a synoptic rain event adding a "spike" of water vapor in the mixed-layer. The upstream boundary condition specifies that an equal amount of water vapor enters and departs the first cell in the domain. This produces a constant background value behind the pulse as it progresses downwind.

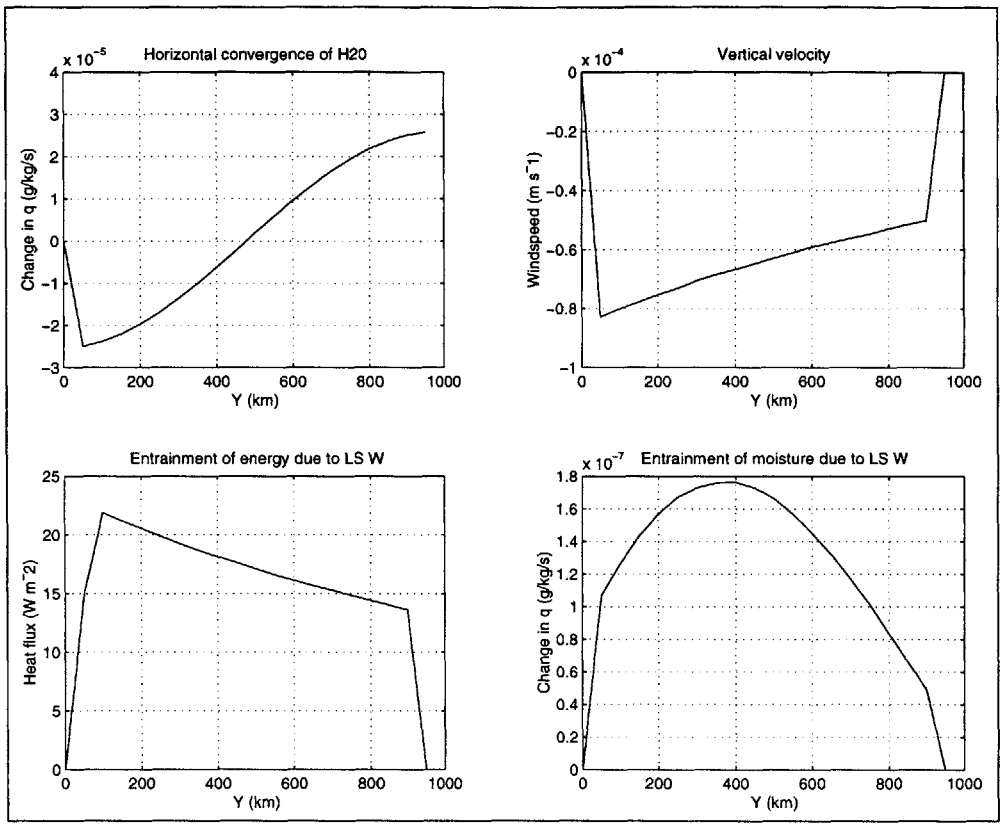

Figure 4-21: Test 3 under linear temperature profile, with moisture added passively to coupled flow. The convergence of water vapor is due to the differential between Q_q upstream and downstream. The total convergence of water vapor is dependent upon the advective (q gradient) and divergent (v gradient terms). In this case, the advective component dominates. This is verified through the final frame of the plot, which shows that the entrainment is out of phase with the horizontal convergence, but is proportional to the wind divergence. Therefore, the advective component of the flow dominates in the first frame. Note that the "entrainment" in the final frame is actually a mass input; it is positive due to the net input of water mass, but actually indicates dry air input and a net decrease in specific humidity. The deamplification (mass sink) of the humidity peak in Fig. 4-24 makes this clear.

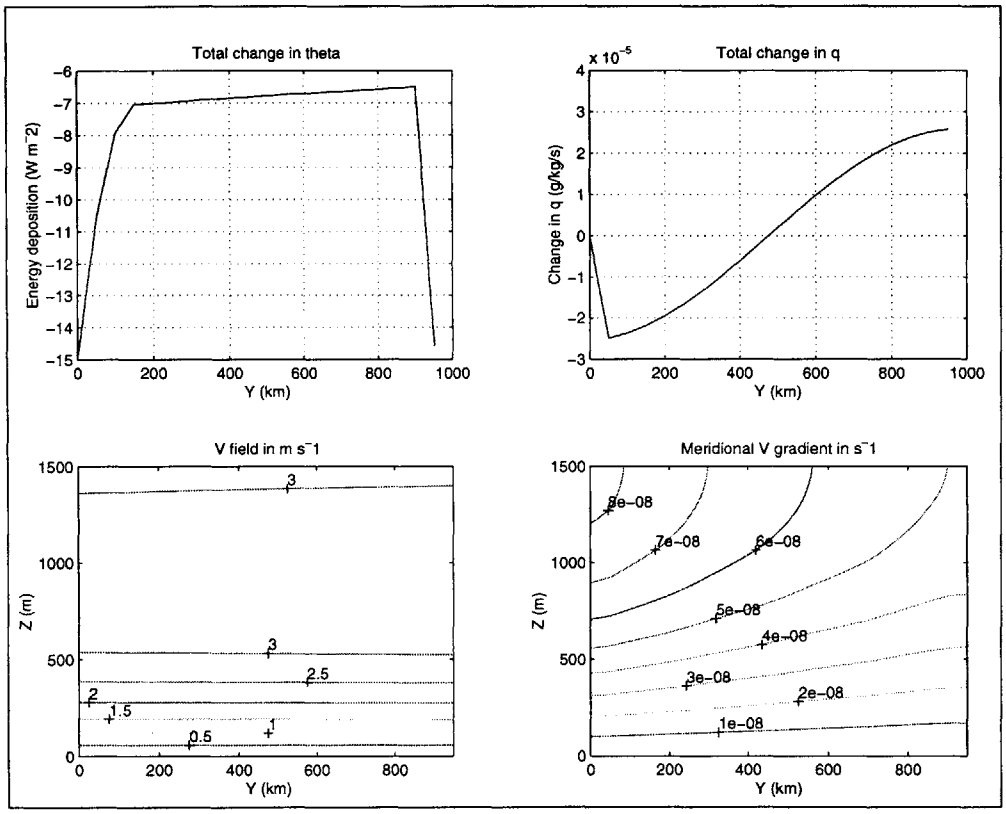

Figure 4-22: Test3 linear temperature profile under passive moisture transport case. As described in Fig. 4-21, the total increment of the specific humidity is determined according to the advective changes, instead of by wind divergence, as described in Fig. 4-21. The wind and meridional gradient of the flow show a well-behaved vertical structure under nearly constant conditions; the small increase from left to right is caused by the sensitivity to temperature decreases in the shear term.

to the meridional flow, and has reduced in amplitude due to the entrainment of dry air aloft. the overall trend terms indicate further movement of the specific humidity profile, as shown in Fig. 4-25 with further damping from negative vertical velocity and dry air entrainment. The total temperature tendency term in Fig. 4-26 shows both the slope equilibration described in the previous model run, and also some undesirable boundary condition anomalies. Again, the q tendency shows a steady progression to the right with a steady state conditions achieved to the left of the domain.

4.4.2 Analysis of water vapor transport over a 20-day time series

Similar thermodynamic processes appear in the Test 3 20-day as the time series for the linear Test 2 case, with additional information about vapor transport in the domain. The plots of Fig. 4-27 show both a diurnal cycle as well as the "slope shift" cited earlier, which is created by the rapid equilibration of the temperature profile to balance the incoming shortwave radiation. The sudden jumps in both the flux divergence and energy entrainment fields verify this conclusion. In contrast to the Test 2 case, the shortwave term has been set higher than the value stipulated in (4.4), so that the temperature trend is toward a higher emission temperature than in previous studies. The temperature tendency term is dominated only by the radiative diurnal cycle, and does not exhibit a signal from gradient equilibration. The movement of the specific humidity peak, as initially indicated in the Test 3 snapshots, is now more fully investigated in Fig. 4-28. As the initialization of the Test 3 study indicates, y=10 begins the run with a peak in the specific humidity, and then through time approaches the value of q stipulated by the initial condition and no-convergence boundary condition at y=0. The humidity-gradient-derived fields begin at an initial value close to zero, and then increase to a temporary peak after 1 day, when the maximum slope of the q peak has moved through. The specific humidity convergence is based upon the advection and divergence components, as in the energy convergence expansion in (4.2). As would be expected from the specific

humidity profile, the specific humidity convergence quickly returns to zero when the peak has passed by, due to the quasi steady-state moisture advection propagating from the southern boundary. The specific humidity entrainment (again, a mass flux not necessarily negative for negative specific humidity tendency) continues to inject dry air into the meridional domain. However, as the divergence of the meridional wind continues to increase (see Fig. 4-29), the entrainment also increases, since it is simply the mass flux of water vapor from above entering the cell. Additional entrainment after the peak has past causes the specific humidity to drop accordingly, but at a decreasing rate. The overall tendency term of the specific humidity shows the peak and then a very small but non-zero negative value associated with the entrainment. In conjunction with the specific humidity plots, the wind profiles the three trends discussed above. First, the diurnal cycle appears weakly in the wind field due to the dependence of the wind field upon the temperature. Second, as the temperature slope equilibrates at the beginning of the model run, the divergence and vertical velocity both show a sudden jump in their respective signals. A steady increase in the magnitudes of the meridional gradient (and decrease in the meridional wind) are both due to radiative disequilibrium resulting in overall heating through time, as shown on the potential temperature plot.

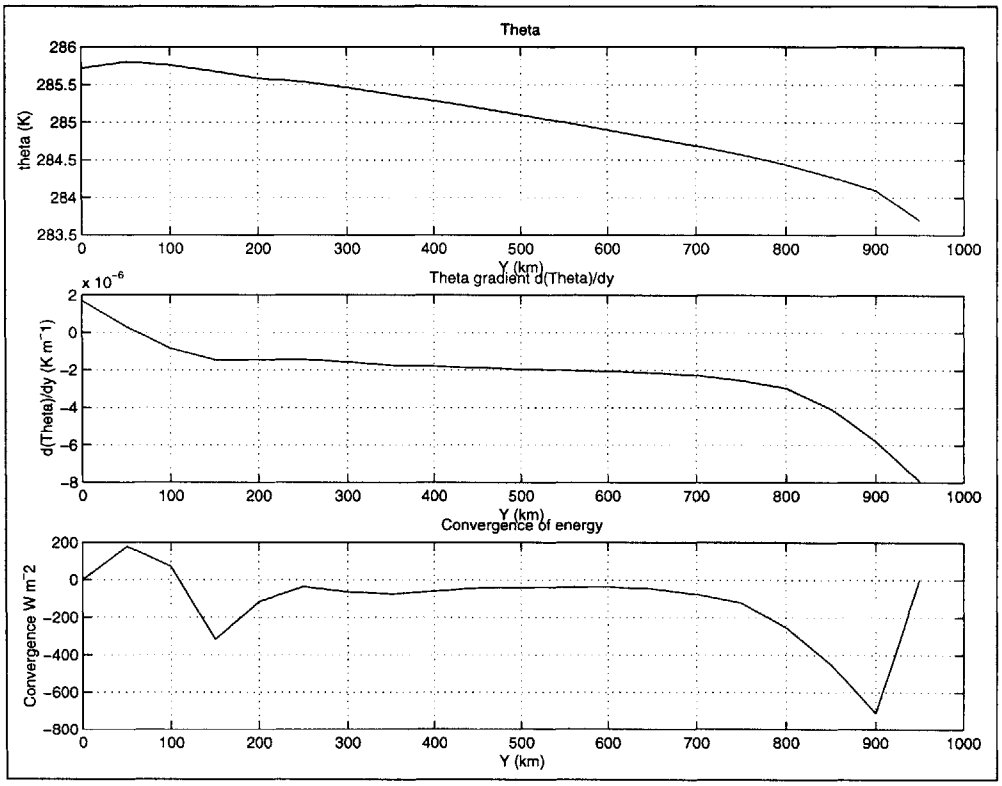

Figure 4-23: Test 3 model results after 1 day. The potential temperature of the mixed-layer has begun to be conformed to the net radiative forcing profile. While remaining close to -2E-6 K/m, the temperature gradient has been altered due to non-convergent boundary conditions and the resultant flow modifications.

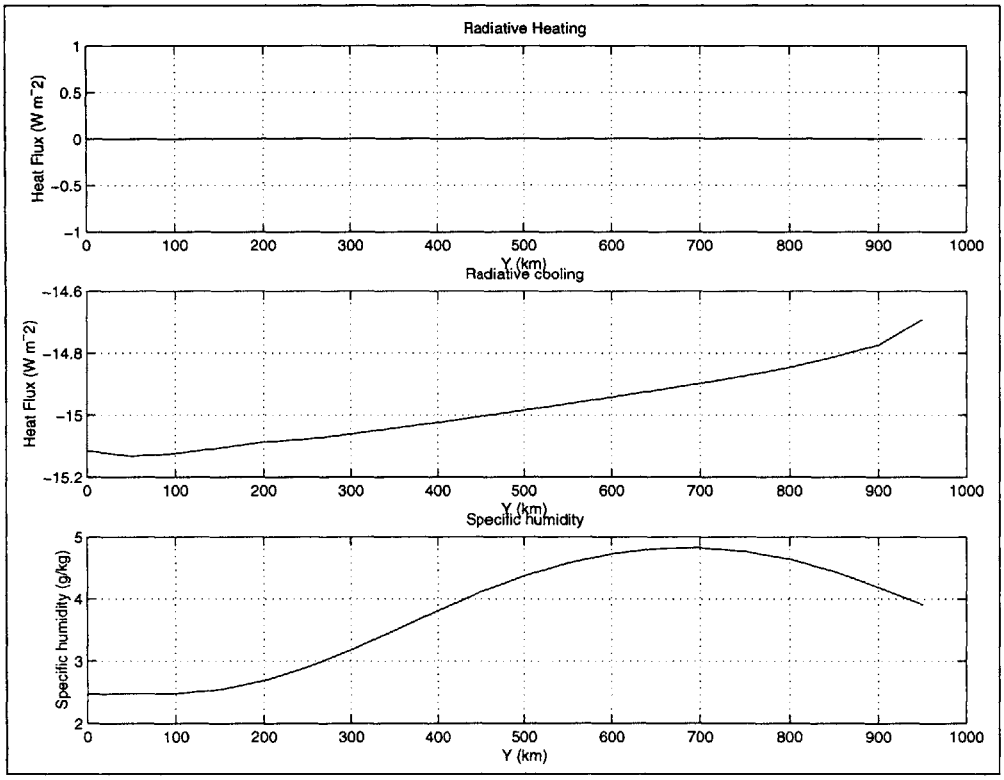

Figure 4-24: Test 3 model results after 1 day. The radiative heating in frame is zero, as the snapshot is taken at midnight. The specific humidity plot shows the progression of the moisture peak through the domain. The constant convergence boundary condition at the southern-most point causes the upstream specific humidity to approach 2.5 g kg^{-1}. The moisture peak has de-amplified due to the entrainment of dryer air from above.

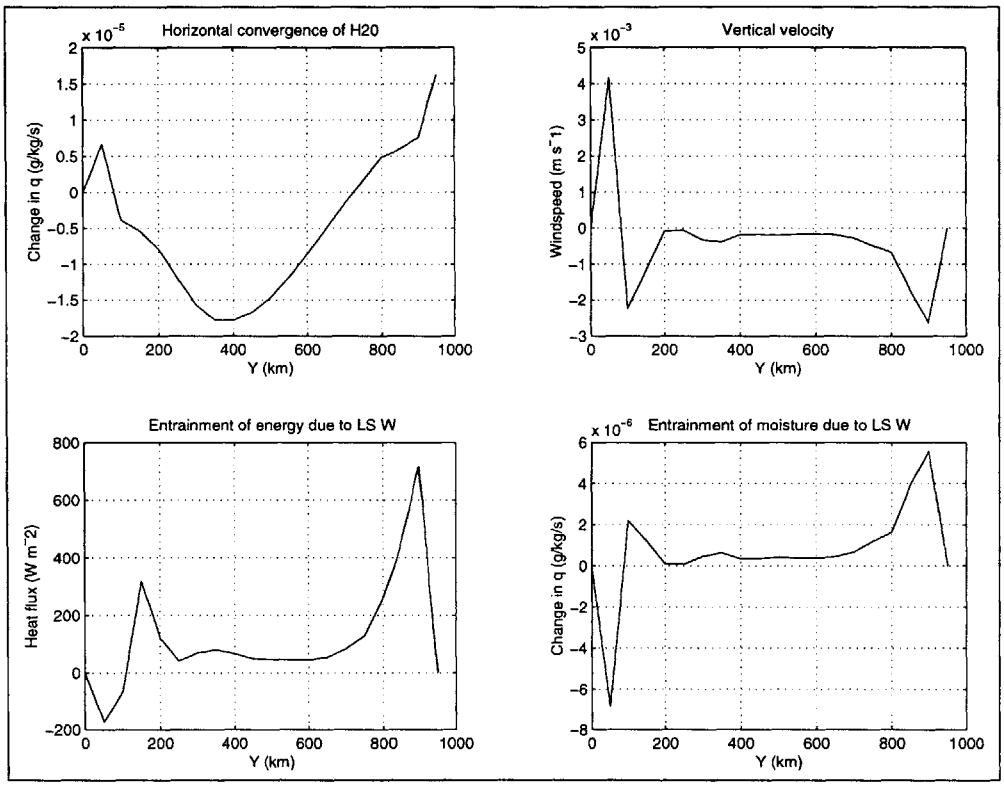

Figure 4-25: Test 3 model run out to 1 day. The frames in this figure depict the conditions created by horizontal wind convergence. The entrainment of moisture and energy are each calculated according to the vertical velocity, as before.

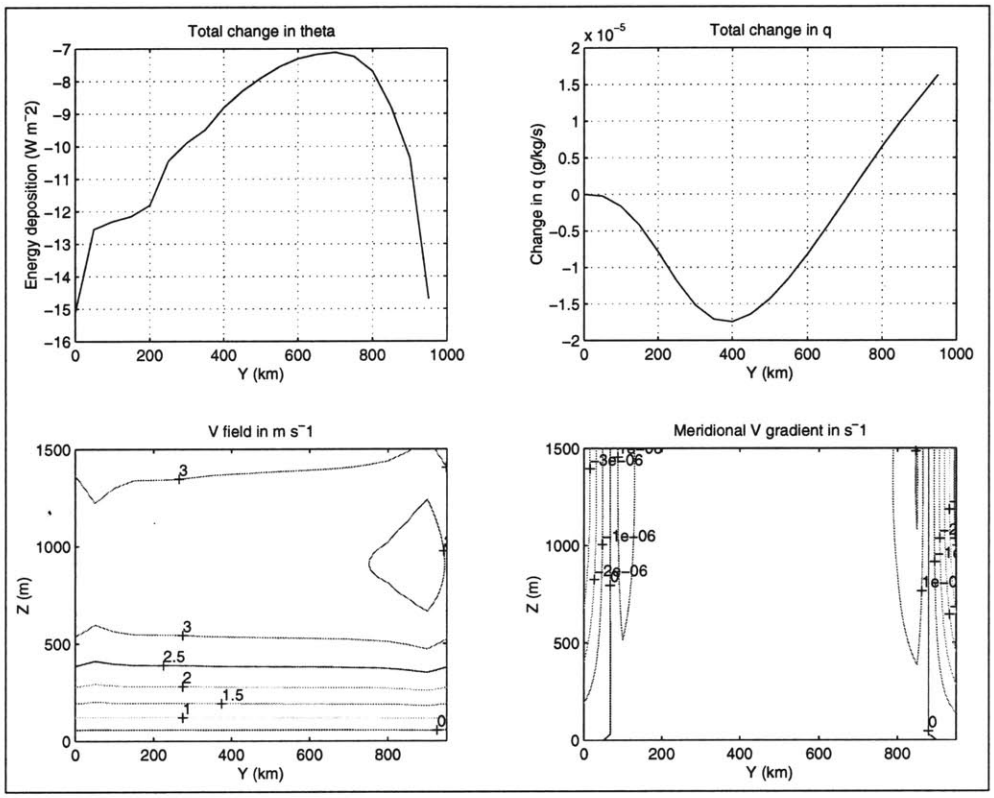

Figure 4-26: Test 3 tendency terms and winds after 1 day. The potential temperature is tending to a shallower linear profile. The specific humidity tendency shows the peak in moisture moving further to the right. Points at the extreme left of the humidity domain are already equilibrated in a region propagating from the southern boundary, as indicated in the region of zero-valued q-increments.

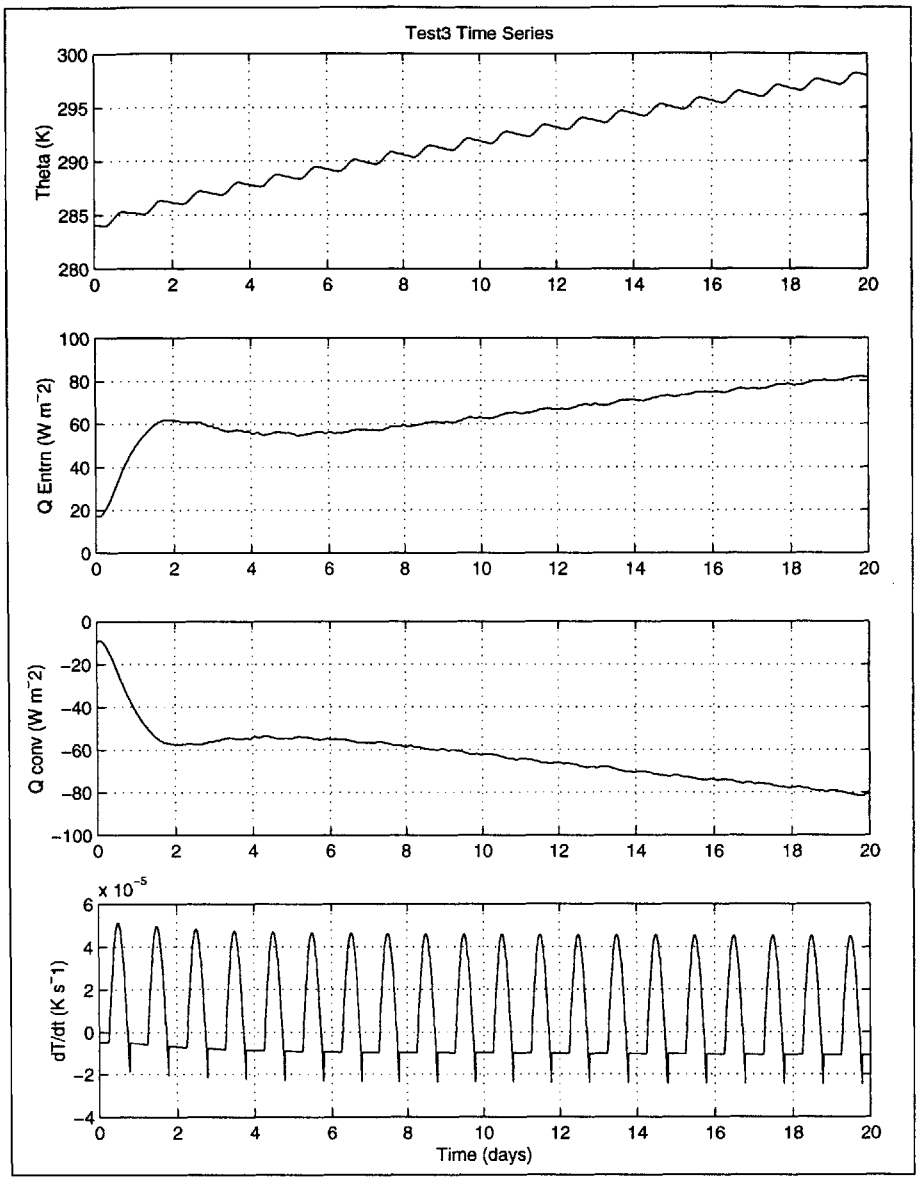

Figure 4-27: Test 3 20-day time series. This plot exhibits both the trends established in previous Test 2 cases, with additional tracking of specific humidity. The temperature in the first frame exhibits an identical characteristic profile as those in the earlier cases, except that the solar incoming radiation was set at a higher value, and the temperature has not yet reached equilibrium. The temperature tendency (last frame) shows a similar oscillatory pattern, with abrupt changes according to the diurnal radiation cycle. The middle frames indicate the compensation between the energy flux convergence (which in this case is dominated by wind divergence, due to the value of z_{scl} selected). The entrainment acts in an equal and opposite direction to balance the majority of the energy convergence.

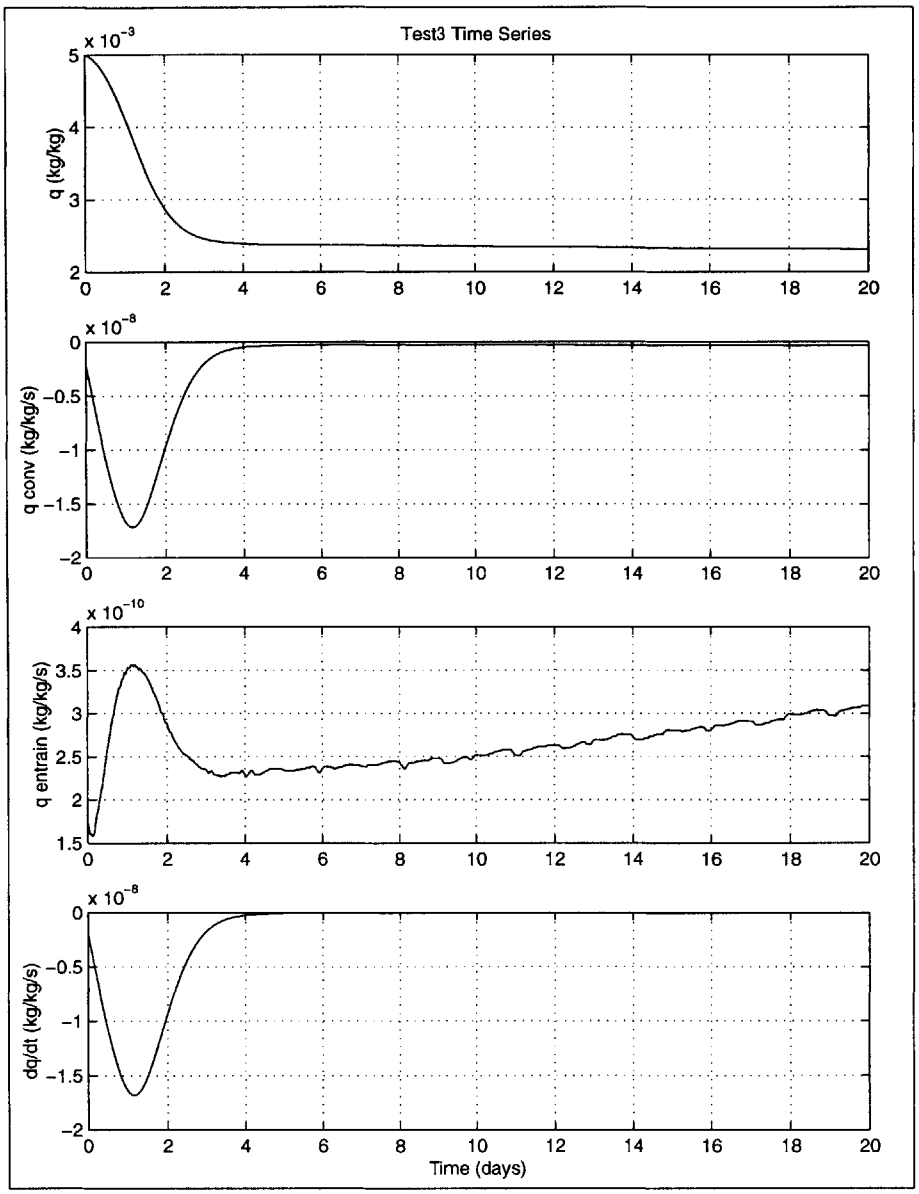

Figure 4-28: Test 3 20-day time series of specific humidity advection. This time series (like all of the others) is taken at the center of the meridional domain, which is the initial location of the specific humidity peak. As the maximum *slope* of humidity passes by, so also do maxima in moisture convergence, entrainment (technically mass flux) and overall tendency. Once the humidity maximum leaves the vicinity of the point y=10, q returns to a uniform state, and the tendency and convergence approach zero. The entrainment continues to diverge independently away from zero as the wind divergence and vertical velocity continue to increase through time. As a result, the specific humidity does show a small decrease through time after returning to its stable location.

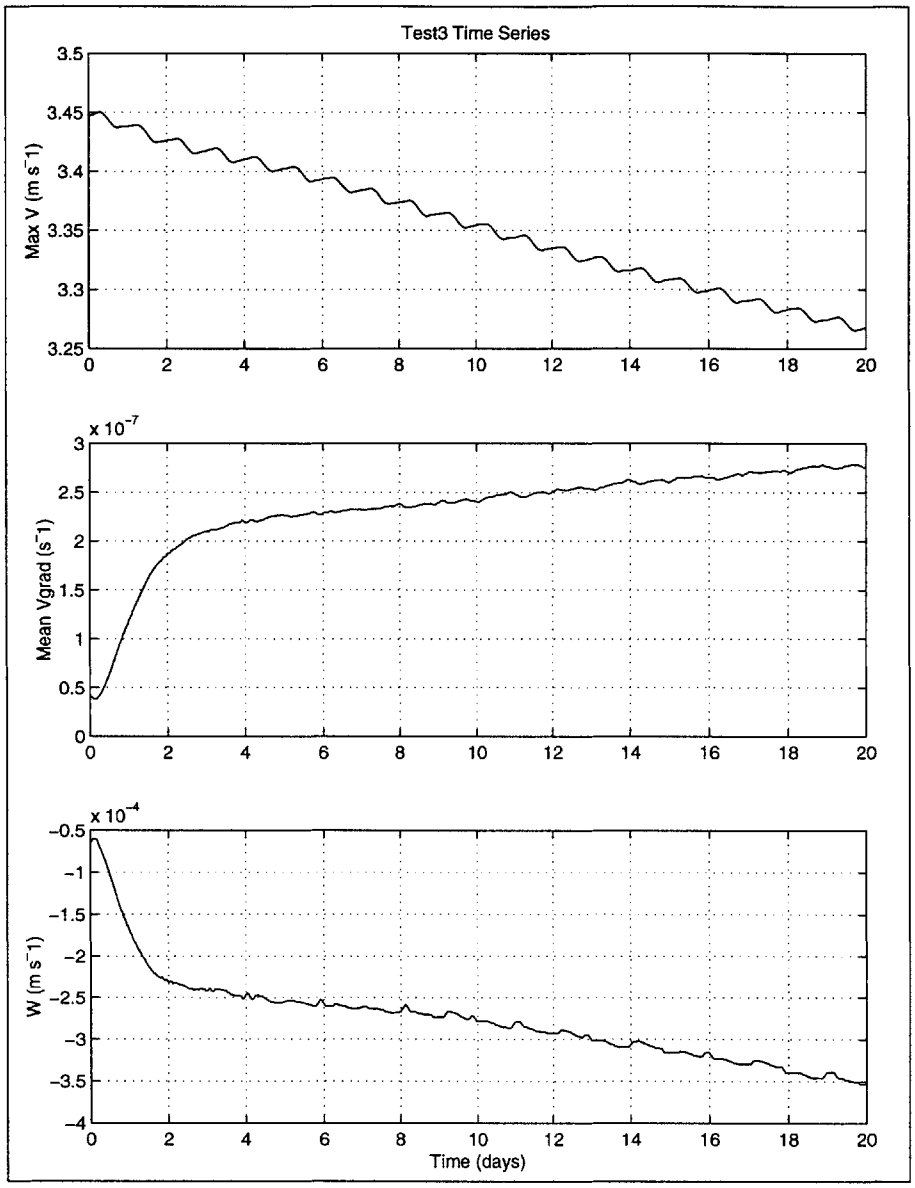

Figure 4-29: Test 3 20-day time series of horizontal and vertical winds. The general trend shown in this figure is for the magnitude of the meridional wind to decrease through time, while the gradient and associated vertical velocity continue to increase in magnitude. This occurs as a result of sensitivity of the wind field to spatial temperature gradients as the mixed-layer warms systematically. The initial spike in the last two plots occurs as a result of the temperature profile suddenly changing slope to match latitudinal heating patterns.

4.5 Integration of ABL code in meridional domain

4.5.1 Overview of model setup

The prototype models described in previous sections form the basis of meridional coupling which is used in the fully integrated LLJ code with mixed-layer processes. A strategy of gradual implementation of the complete LLJ simulation is described in Table 4.2. The mixed layer code is modified as described in Chapter 3, while the meridional coupling prototypes are detached from the radiative fluxes and entrainment which were used temporarily for testing purposes. Out of the five model experiments proposed in Table 4.2, the first has been successfully completed, while the remaining four are not, as will be explained in the final section of this chapter. The first experiment is constructed by using the mixed layer model in Kim and Entekhabi (1998) for the local tendency equations of temperature, specific humidity, and inversion strength, as outlined in the previous chapter. In this particular case, heat advection is decoupled from the potential temperature tendency equation, so that each cell acts as an isolated 0-D model separate from the others. The winds are calculated as a diagnostic and do not contribute to energy feedbacks. Also in contrast to the prototype models, the mixed layer height is now allowed to vary temporally and spatially, which also affects the energy and vapor flux divergences.

The model used for Experiment 1 is initialized in a meridional domain in the exact method of Test 3 and Test 2, and in this case the Profile III scaling parameter is set at 2000 m for the maximum realism. Due to the lack of spatial energetic coupling in this trial, only three major processes affect the 30-day time series at the edges of the domain. First, the soil moisture is kept constant as shown in Table 4.2, which creates an effective source term of moisture in the mixed layer model. Second, the diurnal cycle creates a periodic signal in the atmospheric variables effected by radiative transfer. Third, the height of the boundary layer is allowed to increase and decrease arbitrarily with respect to height, according to the parameterization provided in Chapter 3. The following paragraphs outline these effects on model variables at the southern (y=0) and northern (y=NY) boundaries. Except for a slight uniform shift

in the values due to latitudinal deviation, the plots at the two endpoints are virtually identical. A more extensive set of 30-day plots was constructed at the middle of the domain, denoted y=NY/2.

4.5.2 Experiment 1 results at domain boundaries

The soil moisture forcing creates a feedback process, in which continual increases in the moisture content of the air affect the partitioning of energy at the surface in favor of evaporative fluxes. In Figs. 4-30 and 4-38, the potential temperature continues to increase with respect to time, after first achieving a temporary equilibrium with respect to the radiative fluxes. Mirroring this trend, the ground temperature also shows a temporary equilibrium in Figs. 4-31 and 4-39, but with a higher amplitude due to greater surface cooling at night than the mixed layer itself. The specific humidity in Figs. 4-31 and 4-39 also show a diurnal cycle superimposed upon a steadily increasing moisture content through time. Besides the diurnal cycle, the LCL in the same figures experiences two competing effects: first, the air temperature is becoming warmer, so the LCL should become higher, but as the moisture content increases, the LCL should decrease. Both Figs. 4-31 and 4-39 show that these two factors seem to cancel on another out through time. The differential height of the boundary layer and diurnal cycle comprise the remaining trends found in the 30-day time series at the edges of the domain. The energy flux in Figs. 4-30 and 4-38 shows the competing effects of an increase in temperature overall in the mixed layer, together with a decrease in the boundary layer height (see next section). As the temperature gets higher, the energy flux should increase; as the boundary layer height decreases, the total flux should decrease as well. Similarly, the vapor flux shows an increase due to specific humidity forcing from the soil, together with decreasing mixed layer heights, which cause a leveling off and slight decrease at the end of the time series. the flux divergence shown in Figs. 4-31 and 4-39 both show a weak diurnal cycle, with anomalous peaks due to boundary layer collapse occurring at neighboring points before the boundary layer collapses at the point shown in the figures.

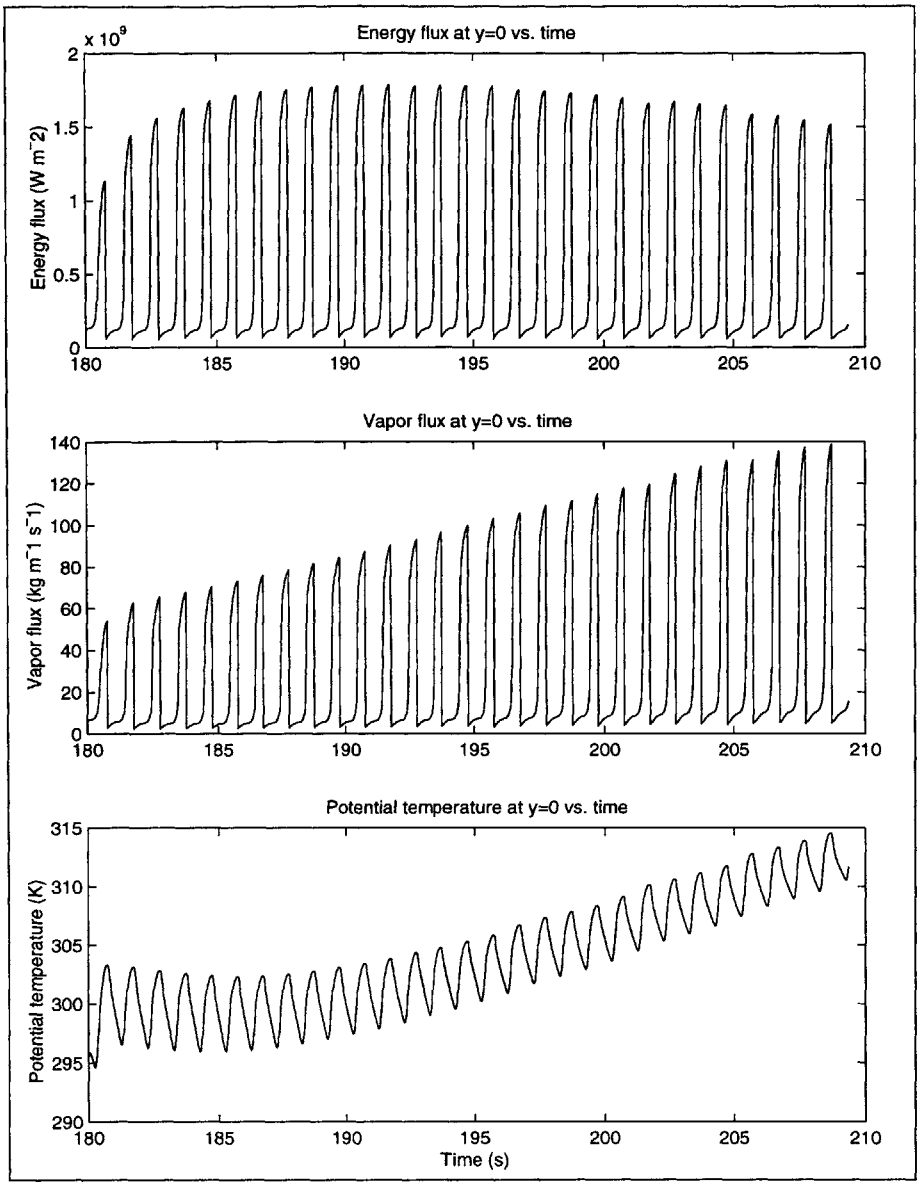

Figure 4-30: Experiment 1 of mixed-layer implementation, over a 30-day time period. The setup for this trial simply involves isolated point diagnostics of derived wind and convergence fields, as dependent only upon mixed-layer processes (and not upon the coupling with adjacent points). These time series are taken at the point y=0, which lies at the far southern boundary of the meridional domain. Overlaying the diurnal cycle imposed by radiative forcing, the time series are affected by soil moisture forcing in the mixed-layer, given the constant soil moisture constraint. In response to the continually increasing moisture content of the boundary layer, the potential temperature increases with respect to time as the evaporation efficiency is limited. The energy flux increases at first, as the potential temperature increases, but then decreases slightly in response to diminishing wind speeds. The vapor flux also exhibits an increase through time as vapor content increases, and a leveling off later in response to weaker winds.

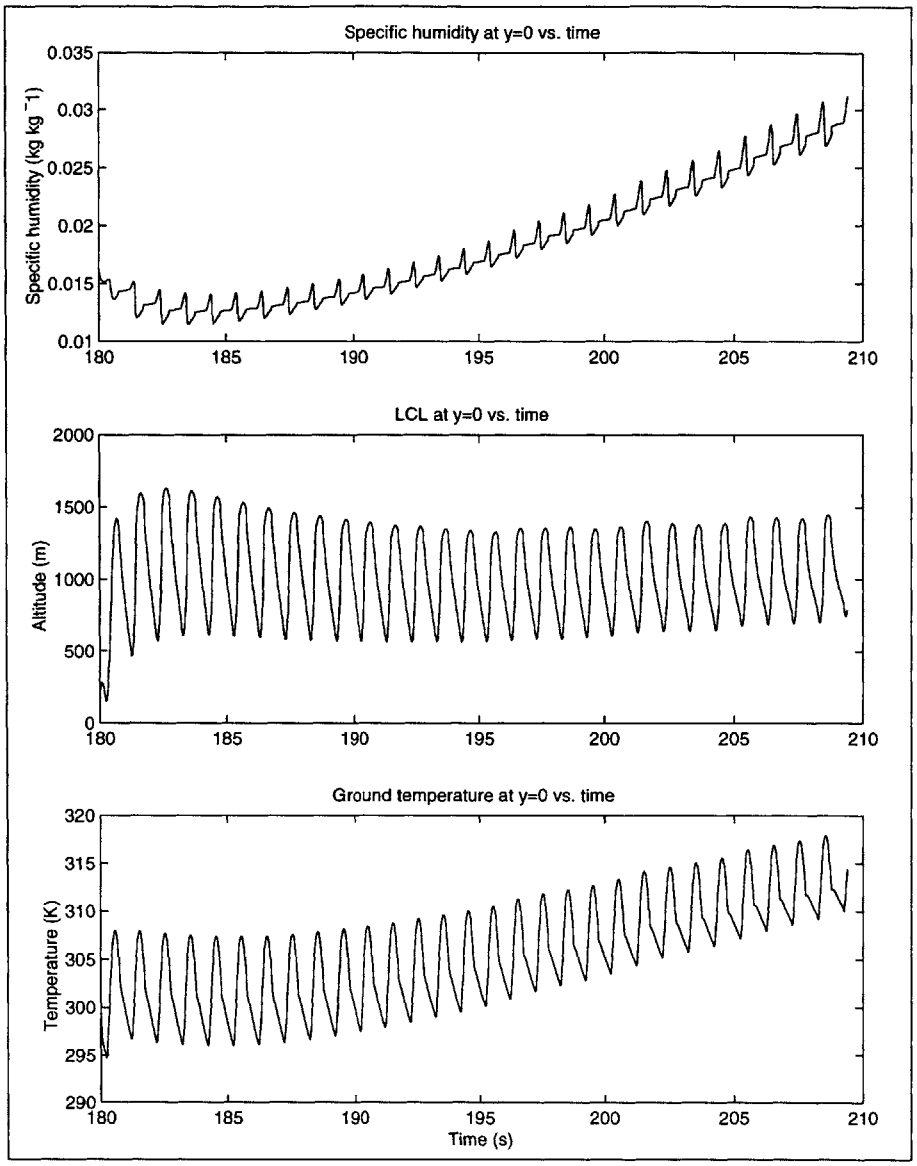

Figure 4-31: 30-day simulation of Experiment 1 trial, with mixed-layer interaction and wind diagnostics. The diurnal oscillation in the specific humidity field is the result of radiative forcing, but out of phase with the potential temperature. The specific humidity experiences a sharp drop late in the morning due to dry air entrainment during mixed-layer growth. Later during daylight hours the mixed-layer has slowed its growth and evaporation has begun to slightly increase the humidity in the layer. A slow increase continues during the stable nighttime conditions, and then more sharply as evaporation occurs in the early morning sunlight. The specific humidity and ground temperature both increase due to evaporative humidity increases (the ground must be warmer to continue to partition energy under more moist conditions). The LCL is under the influence of two competing effects: increasing air temperature raises the LCL while increasing moisture lowers it. In this case the two effects nearly cancel one another and the LCL changes only slightly.

4.5.3 Auxiliary Exp. 1 results at y=NY/2

Verification with boundary time series

A set of time series constructed at the center of the domain more fully details the time evolution from an uncoupled 0-D model. The following plots have been fully discussed in light of the trends described previously: energy flux, vapor flux and energy flux divergence found in Fig. 4-32; potential temperature and specific humidity in Fig. 4-33; the LCL and ground temperature in Fig. 4-34. Of the remaining plots, the water vapor divergence shows a similar, but not identical response to differential boundary-layer collapse (Fig. 4-33).

Surface energy partitioning

The diurnal cycle is clearly evident and stationary through time as shown in the net radiation curve in Fig. 4-35. The positive values (sharp peaks) correspond to daytime heating, while the radiative cooling at night is revealed in the shallow troughs. As discussed earlier, a shift in the energy partitioning at the surface toward latent heating is clear evident in the evaporative energy flux in Fig. 4-34 and the sensible heating flux in Fig. 4-35. The evaporative energy flux increases, due to soil moisture forcing acting on the mixed layer, while the sensible heat flux decreases. The atmospheric boundary-layer height (ABL) shows a decrease corresponding to the decrease in sensible heating in Fig. 4-36. The frictional velocity also decreases slightly in response to the change in surface energy partitioning in Fig. 4-37.

Inversion strength trends

As the maximum daily height of the mixed layer begins to decrease (Fig. 4-36), the potential temperature and vapor inversion strengths both respond accordingly. In the case of the specific humidity inversion strength, the plot is the result of several subtle mechanisms. First, the mixed layer is becoming increasingly moist through time, which creates a greater contrast between the free atmosphere and the mixed layer. As seen from the inversion strength plot in Fig. 4-35, the daily maximum

specific humidity inversion strength becomes more negative (here, "increases") due to this contrast. In addition to the increasing mixed-layer moisture content, the *minimum* daily inversion strength stays about the same, and then decreases slowly, which results in a higher amplitude diurnal cycle on this plot. This process is due to the fact that the nighttime inversion lies in a region which was in the mixed layer during the daytime, so the effective moisture contrast is not as great. In contrast to the specific humidity inversion strength, the potential temperature inversion strength shows a decrease with respect to time, due to the increasing temperature. The free-atmosphere is characterized by warm, dry air, so the temperature contrast is reduced through time.

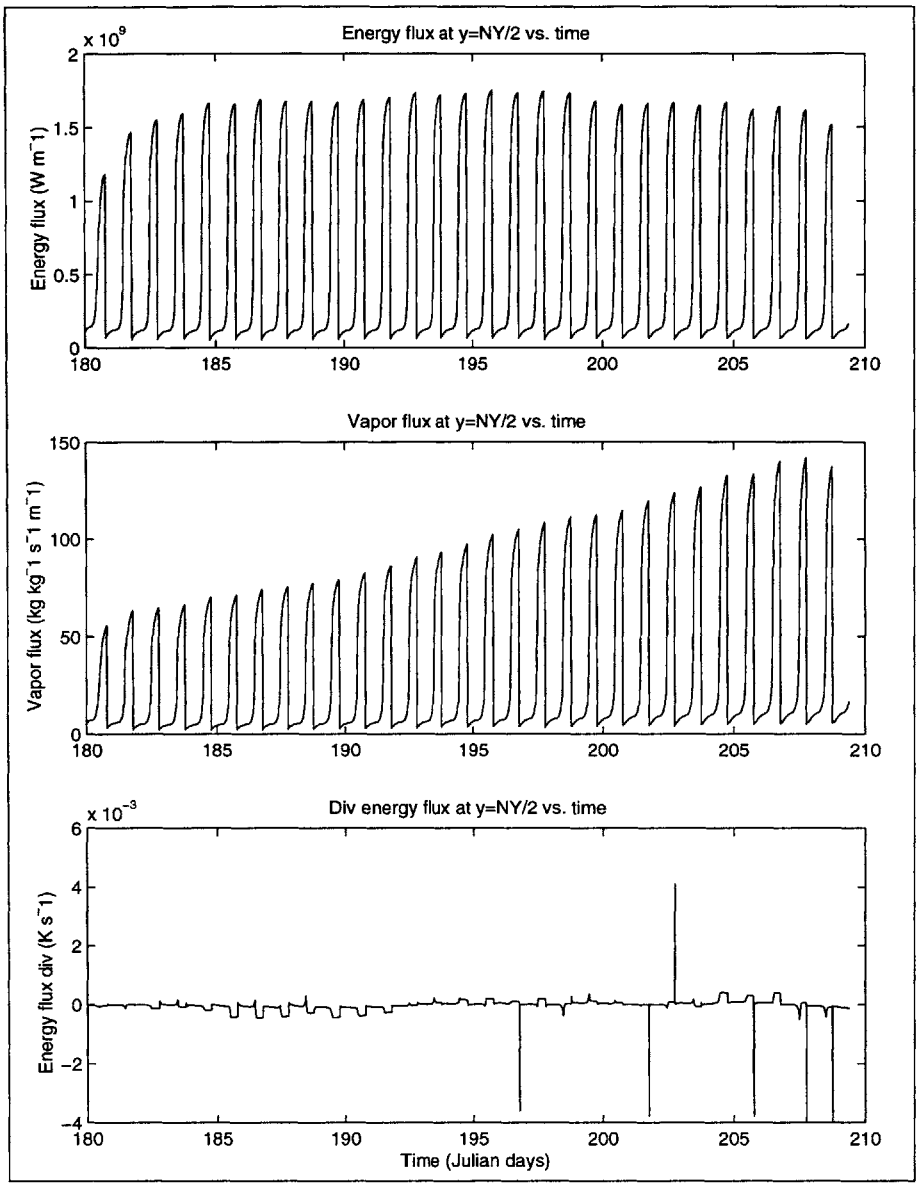

Figure 4-32: Diagnostic 30-day simulation of mixed-layer effects on winds and convergence. The time series in this plot are taken at the point y=NY/2, and show the same effects as described in prior figures. Here, the energy flux increases initially and then actually decreases, due to increasing temperatures and decreasing wind speeds through time. The vapor flux also increases at first under more moist conditions, and then falls off when the wind decreases in magnitude. The divergence of energy flux shows a weak diurnal cycle overshadowed by larger, anomalous peaks in the the time series.

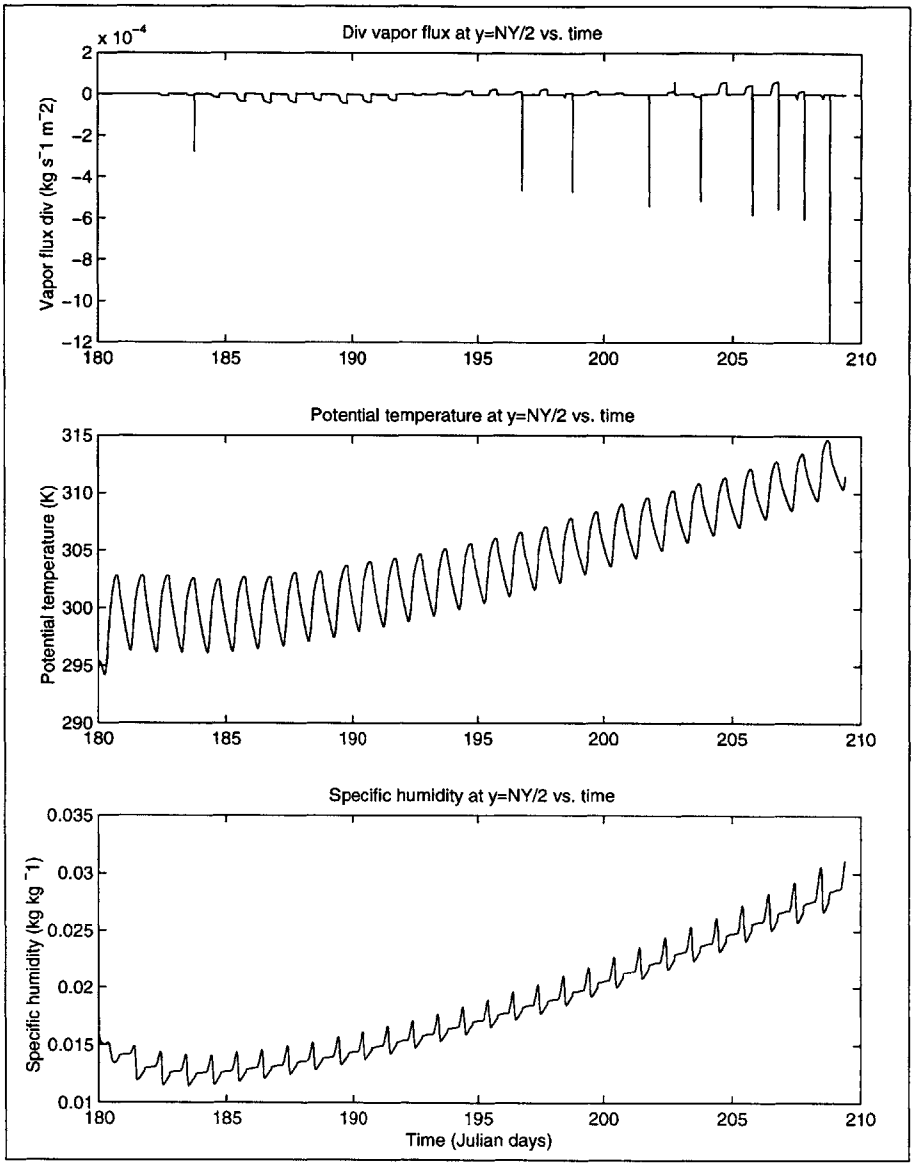

Figure 4-33: Experiment 1 30-day time series in the middle of the meridional domain. The first frame shows the diurnal cycle drowned out be anomalous peaks from boundary layer collapse. The potential temperature profile increases through time, but decreases in amplitude as the moisture content of the mixed-layer increases. The specific humidity shows a similar diurnal trend and long-term trend as in prior figures. However, both the potential temperature and specific humidity are reduced slightly from the y=0 case, due to the increase in latitude.

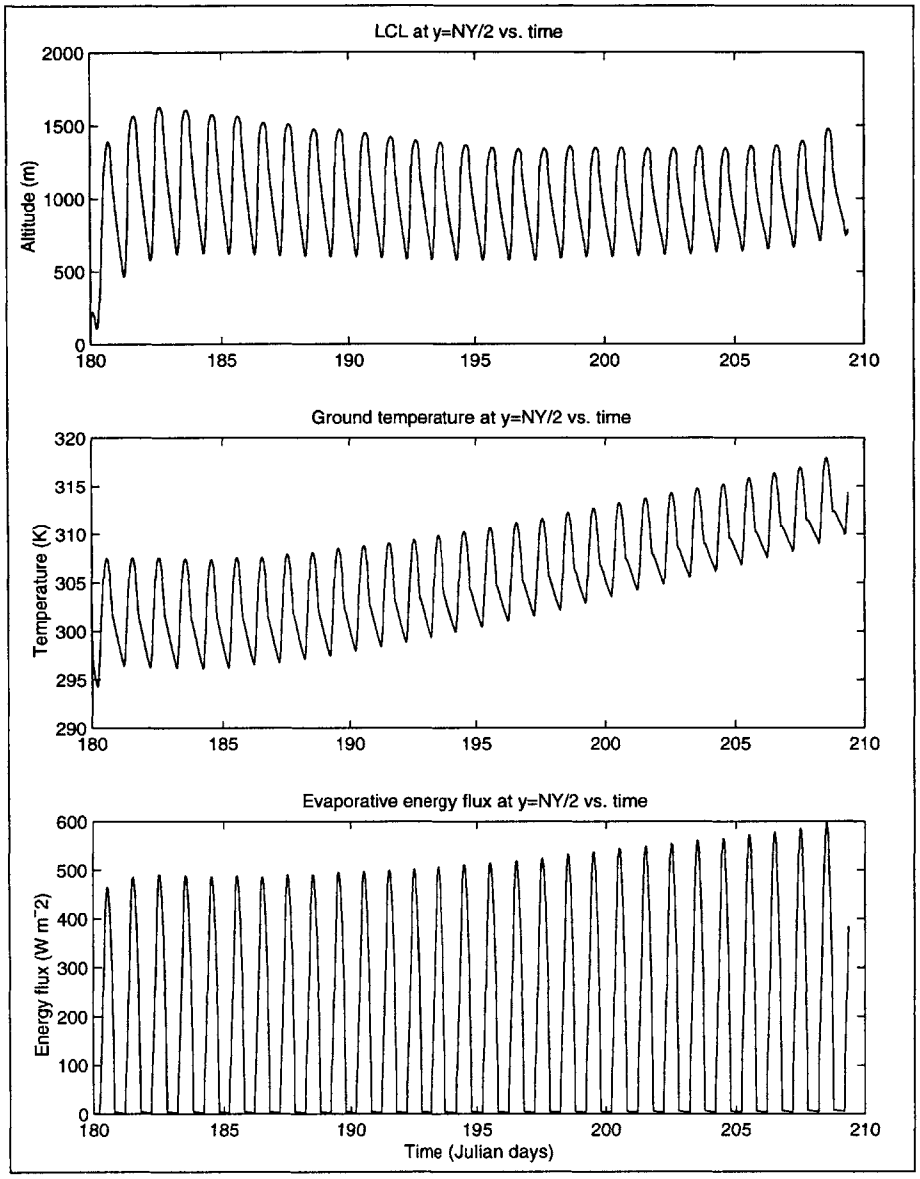

Figure 4-34: 30-day time series of Experiment 1 diagnostics. Under increasingly moist conditions, the ground temperature increases in order to continue to partition energy and remain at equilibrium. This can be verified in the evaporation plot in the final frame, which shows that an increasing portion of the energy is being partitioned into evaporation at the surface. As described in Fig. 4-31, the LCL is under the influence of both increasing moisture at the earth's surface and increasing temperatures, causing it to reach an equilibrium.

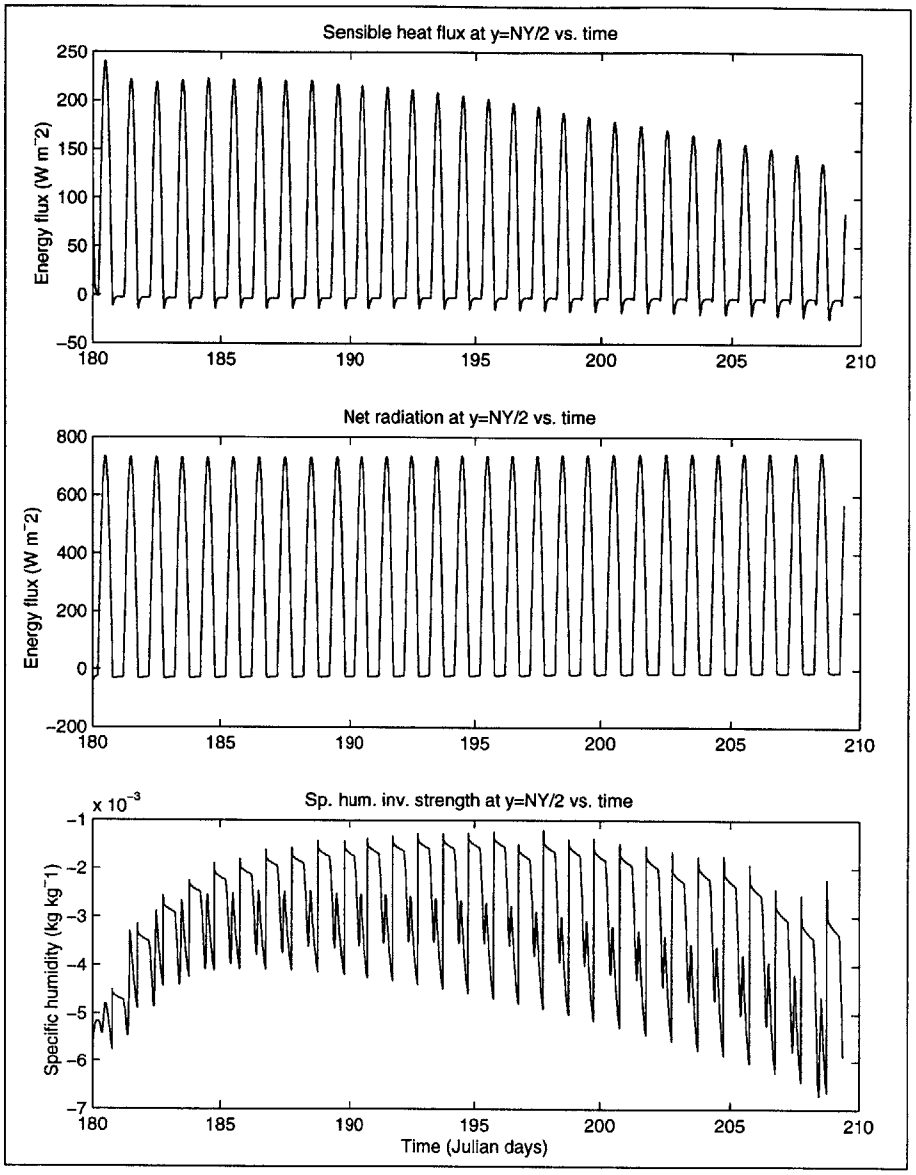

Figure 4-35: Diagnostics of Experiment 1 mixed-layer study. Soil moisture forcing influences the time series of the sensible heating and specific humidity inversion strength. As increasing amounts of energy are partitioned into evaporative flux, the sensible heat flux decreases through time. A more moist mixed-layer creates an enhanced gradient with the free atmosphere. The amplitude of this signal increases with time: the maximum inversion strength in the diurnal cycle increases faster than the minimum, because after boundary layer collapse the boundary layer height lies in the residual mixed-layer, thereby keeping the inversion strength at night smaller. The daytime maximum (more negative) increases more rapidly due to the greater contrast with the free atmosphere. In frame two, the net radiation shows the diurnal cycle of daytime heating and nighttime cooling.

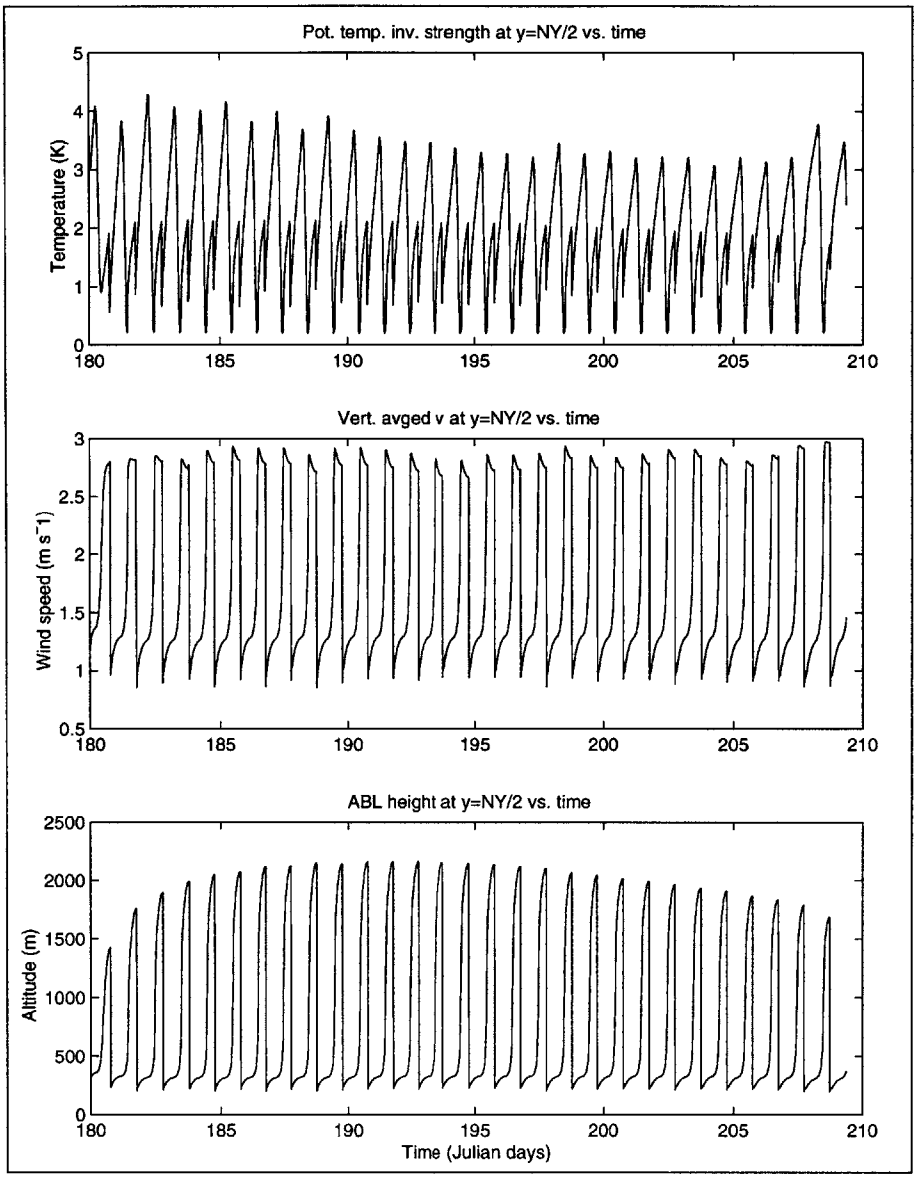

Figure 4-36: Results from Experiment 1 time series taken at the point y=NY/2. The vertically averaged meridional flow is dominated by the diurnal cycle, because it is influenced most strongly by spatial gradients rather than by absolute values of atmospheric state variables. The atmospheric boundary layer height (in the third frame) decreases through time in response to reduced sensible heating from the earth's surface. The potential temperature inversion strength correspondingly reduces somewhat through the majority of the time interval in response to the decrease in the ABL maximum heights.

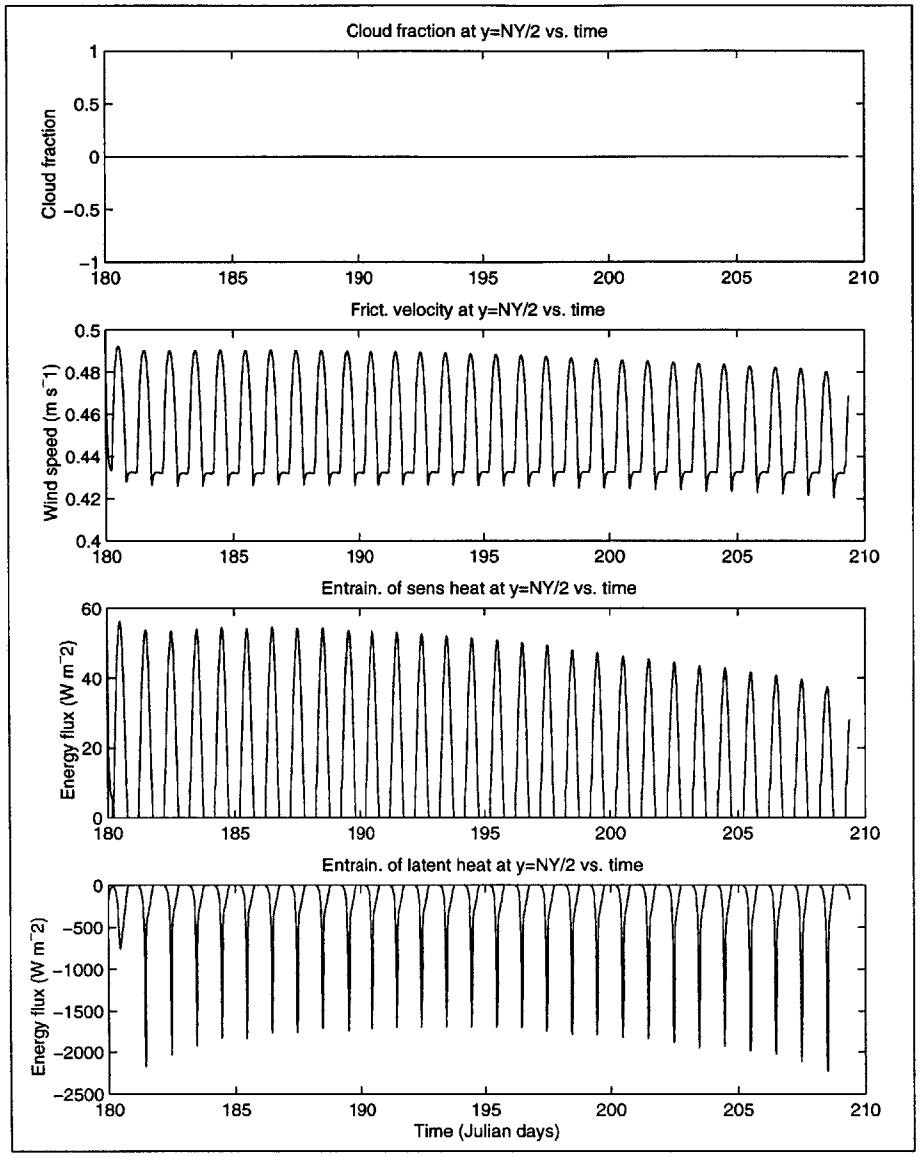

Figure 4-37: Experiment 1 30-day time series at y=NY/2. The cloud fraction in the first plot has been set to 0 arbitrarily in the model, to avoid complications with radiative transfer initially. The frictional velocity decreases slightly due to thermodynamic effects rather than the wind at screen height, which is fixed for this model run. The entrainment of sensible heat is directly coupled to the sensible heating at the earth's surface, so it would be expected that this would occur. The increase in magnitude of the latent heat entrainment is a result of the similar increase of the specific humidity inversion strength, which also increases through the period. As the difference between the free atmosphere and the mixed-layer increases, the amount of energy loss from the intrusion of dry air also increases.

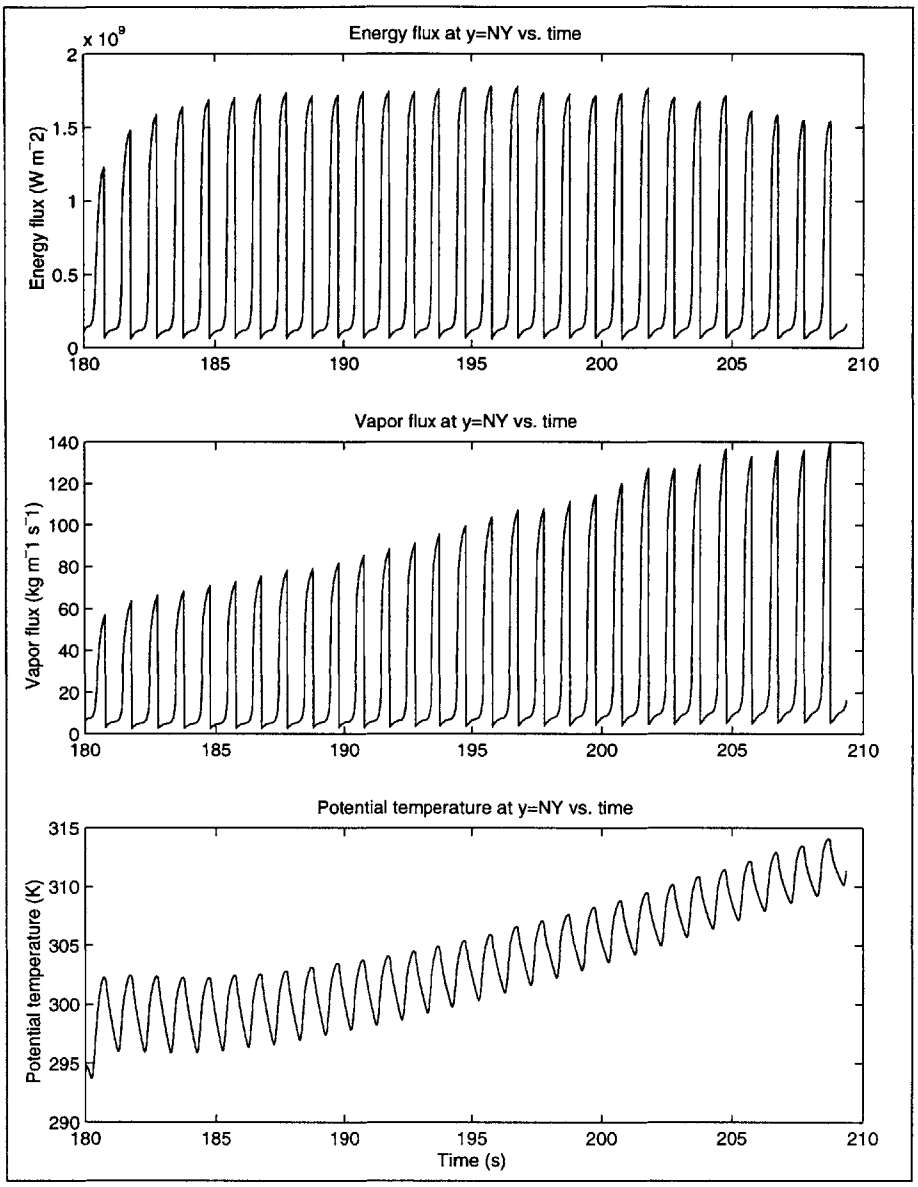

Figure 4-38: 30-day time series results at the northern-most meridional boundary. Like in the previous time series studies, the mixed-layer temperature, moisture content, and wind increase through time. The energy flux and vapor respond to two opposing forcings. On one hand, the wind and the constituent being measured (vapor or heat) are being measured. On the other hand, the maximum daily boundary layer height is decreasing with respect to time, which decreases the interval of integration, and numerically creates smaller flux values. In the case of the energy flux, the second effect is takes effect sooner than in the case of the vapor flux.

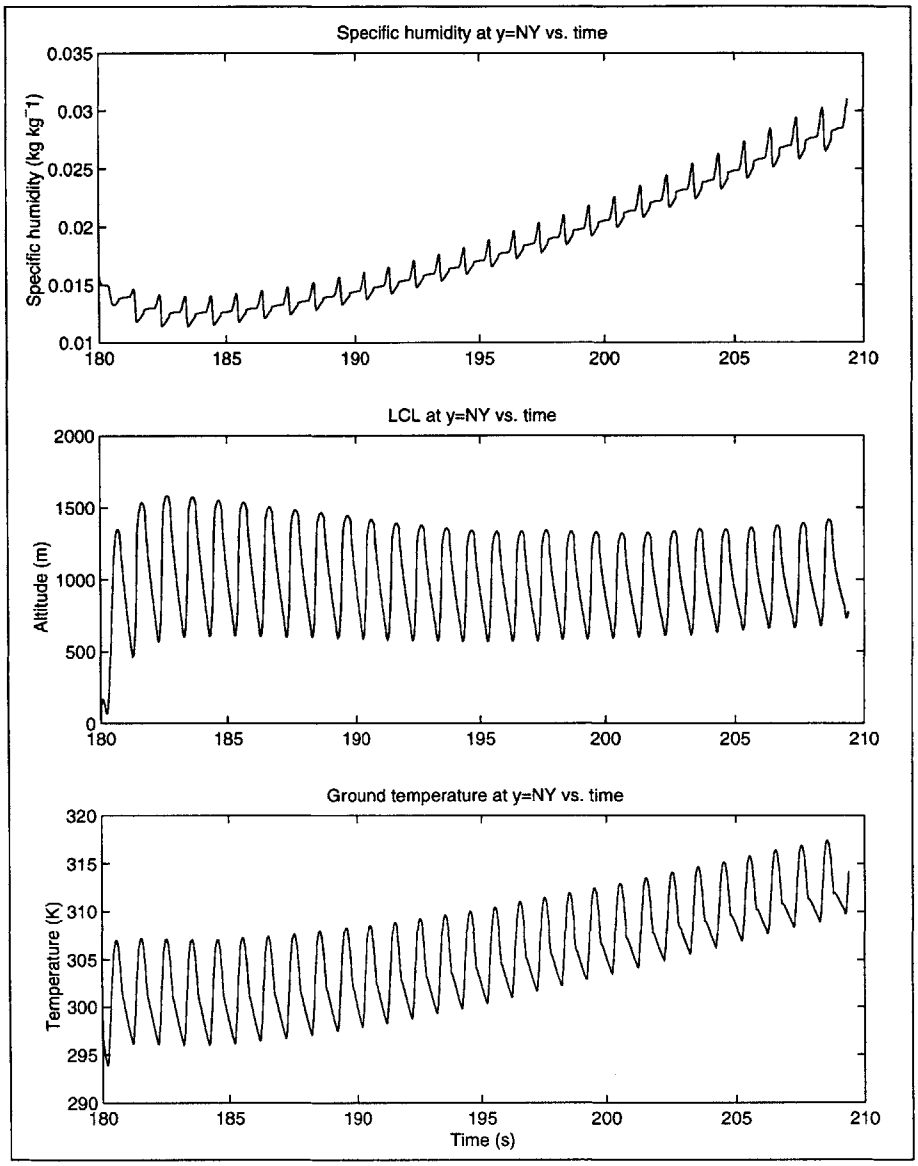

Figure 4-39: Experiment 1 time series trials over 30-days at the point y=NY. The frames here show identical trends as in previous plots, except for the imposed reduction in radiative heating and the imposed boundary conditions in the neighboring cell. Here, we still see a diurnally oscillating trend in all three frames, with increasing moisture and ground temperature as previously noted. The LCL again is influenced by the two competing effects of temperature and humidity increases in the mixed-layer.

Chapter 5

Conclusions

5.1 Remarks on prototype model development

The prototype models determined a number of important trends which are useful for future LLJ simulations using meridional coupling in a 2-D domain.

- A newly-derived Profile III Ekman spiral solution simulates a wind field that is stable to energetic coupling, is physically reasonable at all altitudes, and and is sensitive to baroclinic conditions.
- The Profile III scaling parameter produced significant changes in convergence partitioning. Convergence partitioning in turn determines both the feasibility and nature of LLJ energetic coupling.
- Under a convergence field dominated by advection, a time-dependent sinusoidal temperature profile is successfully modeled as moving downwind in the meridional domain.
- Time series of the sinusoidal Test 2 run showed a superposition of the diurnal cycle, and a larger wavelength "envelope" caused by the advection of a temperature peak.
- Linear time-dependent model runs reveal a sudden initial gradient equilibration of the potential temperature field to net radiative fluxes.

- Test 3 passive water vapor transport is successfully modeled. Advection, dry-air entrainment, and boundary conditions acted as source and sink terms.
- Energy coupling and non-divergent boundary conditions amplify truncation errors in both the linear Test 2 and Test 3 studies.

5.2 Integrated models

The experiments designed in Table 4.2 are not fully executed, except for the first experiment. This trial is designed to diagnose convergence and other meridional fields before fully integrating the mixed-layer 0-D code. From Experiment 1, some general principles emerge.

- Radiative fluxes create an overwhelming diurnal signal in all atmospheric variables analyzed.
- Because the soil moisture tendency term is set to zero, the surface acts as a net source of water and significantly modifies the energy partitioning.
- As the energy partitioning at the surface becomes dominated by latent heating, the maximum daily height of the boundary layer diminishes.
- Changes in the daily maximum height of the mixed layer alter the potential temperature and specific humidity inversion strengths.
- Sudden changes in boundary-layer heights result in unphysical conditions in the energy convergence field, due to both the spatial heterogeneity of collapse times, as well as the altered vertically-integrated fluxes between non-collapsed and collapsed cells.

5.3 Future research

The additional models presented in Table 4.2 form a starting point for further LLJ studies. Several obstacles must be overcome for the models to be run, however.

First, more work needs to be done on the nature of the relationship between the Profile III scaling parameter and the partitioning of convergence in the meridional model, as shown in Figs. 4-3 and 4-4. Choosing the scaling parameter must be done carefully in order to insure model stability with regard to spatial anomalies. Second, boundary conditions (except sinusoidal case) continue to warrant attention. The non-convergent conditions at the edges of the domain seem to create spurious noise which propagates and is amplified by spatial instability. Third, the collapse of the boundary layer has proved difficult to accommodate—possible solutions include using the LCL as a surrogate boundary layer height for the purposes of flux convergence. After accomplishing these objectives, added realism might result from adding the effects of terrain, another documented source of LLJ forcing. In addition, it is speculated that soil moisture gradients over the Great Plains would create feedbacks between energy and vapor transport.

Appendix A

Thermal wind parameterization of vertical shear in geostrophic flow

The thermal wind is defined as the change in the geostrophic wind with respect to height, which depends upon the horizontal temperature gradients normal to the geostrophic flow. The following thermal wind derivation closely parallels Hess (1959). The geostrophic winds in Cartesian coordinates are given by

$$fu_g = -\frac{1}{\rho}\frac{\partial P}{\partial y} \tag{A.1}$$

$$fv_g = \frac{1}{\rho}\frac{\partial P}{\partial x} \tag{A.2}$$

where P is the thermodynamic pressure. The Coriolis parameter, f, is given by $f = 2\omega \sin\phi$, where $\omega \approx 7.29 \times 10^{-5}$ s^{-1} is the angular velocity of the earth and ϕ is the latitude measured from the equatorial plane. The vertical variation of the geostrophic wind will be assumed to follow a first-order Taylor series approximation with respect to altitude,

$$u_g \approx u_g|_{z=z_*} + \left(\left.\frac{\partial u_g}{\partial z}\right|_{z=z_*}\right)(z - z_*) = U_{g*} + m_*(z - z_*) \tag{A.3}$$

$$v_g \approx v_g|_{z=z_*} + \left(\left.\frac{\partial v_g}{\partial z}\right|_{z=z_*}\right)(z - z_*) = V_{g*} + n_*(z - z_*) \tag{A.4}$$

Here, the geostrophic winds at the top of the boundary layer in the x- and y-direction are denoted by U_{g*} and V_{g*}, respectively. The Taylor series first order approximation is centered at the point z_*. The terms m_* and n_* are the vertical shear terms of the zonal and meridional geostrophic winds evaluated at $z = z_*$ and are invariant with respect to height. Expressions for m and n will now be sought by taking the vertical derivative of (A.1) and (A.2),

$$\frac{\partial u_g}{\partial z} = \frac{\partial}{\partial z}\left(-\frac{1}{f\rho}\frac{\partial P}{\partial y}\right) \tag{A.5}$$

$$\frac{\partial v_g}{\partial z} = \frac{\partial}{\partial z}\left(\frac{1}{f\rho}\frac{\partial P}{\partial x}\right) \tag{A.6}$$

The ideal gas law for dry air is given by

$$P = \rho RT \tag{A.7}$$

where R is the specific gas constant for dry air and T is the temperature. As a result, ρ may be expressed in terms of the thermodynamic variables in (A.7) and substituted into (A.5) and (A.6) to obtain

$$\frac{\partial u_g}{\partial z} = -\frac{R}{f}\frac{\partial}{\partial z}\left(\frac{T}{P}\frac{\partial P}{\partial y}\right) \tag{A.8}$$

$$\frac{\partial v_g}{\partial z} = \frac{R}{f}\frac{\partial}{\partial z}\left(\frac{T}{P}\frac{\partial P}{\partial x}\right) \tag{A.9}$$

where $\frac{1}{\rho}$ is given by $\frac{1}{\rho} = \frac{RT}{P}$. Expanding the vertical derivative in (A.8) and (A.9) according to the chain rule of calculus,

$$\frac{\partial u_g}{\partial z} = -\frac{R}{f}\left(\left[\frac{1}{P}\frac{\partial T}{\partial z} - \frac{T}{P^2}\frac{\partial P}{\partial z}\right]\frac{\partial P}{\partial y} + \frac{T}{P}\frac{\partial^2 P}{\partial z \partial y}\right) \tag{A.10}$$

$$\frac{\partial v_g}{\partial z} = \frac{R}{f}\left(\left[\frac{1}{P}\frac{\partial T}{\partial z} - \frac{T}{P^2}\frac{\partial P}{\partial z}\right]\frac{\partial P}{\partial x} + \frac{T}{P}\frac{\partial^2 P}{\partial z \partial x}\right) \tag{A.11}$$

Now, the change in pressure with respect to height is given by the hydrostatic relation, e.g.

$$\frac{\partial P}{\partial z} = -\rho g = -\frac{P}{RT} g \tag{A.12}$$

The expression for $\frac{\partial P}{\partial z}$ in (A.12) is substituted into (A.10) and (A.11) and $\frac{1}{P}$ terms are now replaced with $\frac{1}{\rho RT}$ to obtain

$$\frac{\partial u_g}{\partial z} = -\frac{R}{f}\left(\left[\frac{1}{\rho RT}\frac{\partial T}{\partial z} - \frac{T}{P^2}\left(-\frac{Pg}{RT}\right)\right]\frac{\partial P}{\partial y} + \frac{T}{P}\frac{\partial}{\partial y}\left(\frac{-Pg}{RT}\right)\right) \tag{A.13}$$

$$\frac{\partial v_g}{\partial z} = \frac{R}{f}\left(\left[\frac{1}{\rho RT}\frac{\partial T}{\partial z} - \frac{T}{P^2}\left(-\frac{Pg}{RT}\right)\right]\frac{\partial P}{\partial x} + \frac{T}{P}\frac{\partial}{\partial x}\left(\frac{-Pg}{RT}\right)\right) \tag{A.14}$$

Expanding the horizontal derivatives and simplifying terms in (A.13) and (A.14),

$$\frac{\partial u_g}{\partial z} = -\frac{R}{f}\left[\frac{1}{\rho RT}\frac{\partial T}{\partial z}\frac{\partial P}{\partial y} + \frac{g}{RP}\frac{\partial P}{\partial y} - \frac{g}{RP}\frac{\partial P}{\partial y} + \frac{g}{RT}\frac{\partial T}{\partial y}\right] \tag{A.15}$$

$$\frac{\partial v_g}{\partial z} = \frac{R}{f}\left[\frac{1}{\rho RT}\frac{\partial T}{\partial z}\frac{\partial P}{\partial x} + \frac{g}{RP}\frac{\partial P}{\partial x} - \frac{g}{RP}\frac{\partial P}{\partial x} + \frac{g}{RT}\frac{\partial T}{\partial x}\right] \tag{A.16}$$

Straightforward algebraic manipulation yields

$$\frac{\partial u_g}{\partial z} = -\frac{1}{\rho f T}\frac{\partial P}{\partial y}\frac{\partial T}{\partial z} - \frac{g}{fT}\frac{\partial T}{\partial y} \tag{A.17}$$

$$\frac{\partial v_g}{\partial z} = \frac{1}{\rho f T}\frac{\partial P}{\partial x}\frac{\partial T}{\partial z} + \frac{g}{fT}\frac{\partial T}{\partial x} \tag{A.18}$$

Substituting from (A.1) and (A.2) into (A.17) and (A.18),

$$\frac{\partial u_g}{\partial z} = \frac{u_g}{T}\frac{\partial T}{\partial z} - \frac{g}{fT}\frac{\partial T}{\partial y} \tag{A.19}$$

$$\frac{\partial v_g}{\partial z} = \frac{v_g}{T}\frac{\partial T}{\partial z} + \frac{g}{fT}\frac{\partial T}{\partial x} \tag{A.20}$$

The desired expressions for m and n in (A.3) and (A.4) are now evaluated at $z = z_*$. Recalling from (A.3) and (A.4), the geostrophic winds at this level are

$$u_g|_{z=z_*} = U_{g*} \tag{A.21}$$

$$v_g|_{z=z_*} = V_{g*} \tag{A.22}$$

In the well-mixed layer, the lapse rate is simply the dry adiabatic lapse rate, denoted Γ_d,

$$\frac{\partial T}{\partial z} = -\Gamma_d = -\frac{g}{c_P} \tag{A.23}$$

where c_P is the specific heat for dry air at constant pressure. Under a background dry adiabatic lapse rate, the temperature is a linear function of height given by

$$T|_{z=z_*} = \theta - \Gamma_d z_* \tag{A.24}$$

Using this result, the horizontal derivatives of temperature at any altitude within the mixed layer are equal to the horizontal potential temperature gradients at the same height,

$$\frac{\partial T}{\partial x} = \frac{\partial}{\partial x}(\theta - \Gamma_d z) = \frac{\partial \theta}{\partial x} \tag{A.25}$$

$$\frac{\partial T}{\partial y} = \frac{\partial}{\partial y}(\theta - \Gamma_d z) = \frac{\partial \theta}{\partial y} \tag{A.26}$$

Substituting the expressions in (A.21), (A.22), (A.23), (A.24), (A.25), and (A.26) into (A.19) and (A.20) yields

$$\left.\frac{\partial u_g}{\partial z}\right|_{z=z_*} = m_* = -\frac{U_{g*}\Gamma_d}{\theta - \Gamma_d z_*} - \frac{g}{f(\theta - \Gamma_d z_*)}\frac{\partial \theta}{\partial y} \tag{A.27}$$

$$\left.\frac{\partial v_g}{\partial z}\right|_{z=z_*} = n_* = -\frac{V_{g*}\Gamma_d}{\theta - \Gamma_d z_*} + \frac{g}{f(\theta - \Gamma_d z_*)}\frac{\partial \theta}{\partial x} \tag{A.28}$$

Upon inspection, the terms in (A.19) and (A.20) constitute the two mechanisms by which vertical shear in the geostrophic wind is generated. The terms $-\frac{U_{g*}\Gamma_d}{T}$ and $-\frac{V_{g*}\Gamma_d}{T}$ correspond to the vertical shear in the geostrophic flow caused by the background atmospheric instability. The second terms, $-\frac{g}{fT}\frac{\partial \theta}{\partial y}$ and $\frac{g}{fT}\frac{\partial \theta}{\partial x}$ constitute the shear caused by local potential temperature gradients.

Appendix B

Profile I, II, and III Ekman spiral solutions

In the meridional model presented in this paper, the effects of friction at the no-slip boundary of the earth's surface are parameterized according to an Ekman spiral. While the classical Ekman spiral assumes a constant zonal geostrophic wind with respect to height, the following derivation takes into account vertical variation in the background flow. Three Ekman layer profiles of the meridional and zonal wind are formulated from three zonal geostrophic wind profiles. (In all three cases it will be assumed that there is no meridional geostrophic wind, that is, $v_g = 0$.) The second-order momentum equation will be solved for its homogeneous solution, with the three particular solutions presented in order of increasing complexity. The derivation in the first case is taken from Holton (1992), with details of particular solutions taken from Boyce and DiPrima (1992).

B.0.1 Homogeneous solution to horizontal equations of motion

Assuming the flux-gradient approximation (with constant eddy viscosity), the Reynolds-averaged equations of motion in Cartesian coordinates become

$$K_m \frac{\partial^2 U}{\partial z^2} + f\left(V - v_g\right) = 0 \text{ where } v_g{=}0 \tag{B.1}$$

$$K_m \frac{\partial^2 V}{\partial z^2} - f\left(U - u_g\right) = 0 \tag{B.2}$$

with the boundary conditions

$$U = 0, V = 0 \text{ at } z = z_{sfc} \tag{B.3}$$

$$U \to u_g, V \to 0 \text{ as } z \to \infty \tag{B.4}$$

Here, K_m is the eddy viscosity (with units of $\mathrm{m}^2\ \mathrm{s}^{-1}$) and is assumed to be constant. The total zonal wind speed, U, and the total meridional wind speed, V, are distinct from the zonal geostrophic wind, u_g, and the meridional geostrophic wind, $v_g = 0$. The two momentum equations will now be combined by multiplying (B.2) by $i = \sqrt{-1}$, adding it to (B.1), and dividing the result by K_m to yield

$$\frac{\partial^2 \left(U + iV\right)}{\partial z^2} - \frac{if}{K_m}\left(U + iV\right) = -\frac{if}{K_m}\left(u_g\right) = G\left(z\right) \tag{B.5}$$

where $G\left(z\right)$ is the forcing function. In (B.5), consider the following variable substitutions,

$$\frac{\partial^2 q}{\partial z^2} - a^2 q = -a^2 u_g \tag{B.6}$$

where $a = \sqrt{\frac{if}{K_m}}$ and $q = U + iV$. The differential equation is now solved using a technique found in Boyce and DiPrima (1992). The desired general solution to (B.6) is of the form

$$Q\left(z\right) = Q_{hom}\left(z\right) + Q_{par}\left(z\right) = C_1 q_1\left(z\right) + C_2 q_2\left(z\right) + Q_{par}\left(z\right); C_1, C_2 \in \Re \tag{B.7}$$

where q_1 and q_2 are linearly independent solutions of the homogeneous equation

$$\frac{\partial^2 q}{\partial z^2} - a^2 q = 0 \tag{B.8}$$

The homogeneous solutions q_1 and q_2 are computed from the characteristic equation of (B.8) and are given by

$$Q_{hom}(z) = C_1 q_1(z) + C_2 q_2(z) = C_1 e^{az} + C_2 e^{-az} \tag{B.9}$$

The particular solution, $Q_{par}(z)$, is of the form

$$Q_{par}(z) = -q_1(z) \int \frac{q_2(z) G(z)}{W(q_1, q_2)(z)} dz + q_2(z) \int \frac{q_1(z) G(z)}{W(q_1, q_2)(z)} dz \tag{B.10}$$

where $W(q_1, q_2)(z)$ denotes the Wronskian of q_1 and q_2 with respect to z, defined as

$$W(q_1, q_2)(z) = \begin{vmatrix} q_1 & q_2 \\ \frac{\partial q_1}{\partial z} & \frac{\partial q_2}{\partial z} \end{vmatrix} = \begin{vmatrix} e^{az} & e^{-az} \\ ae^{az} & -ae^{-az} \end{vmatrix} = -2a \tag{B.11}$$

The total solution $Q(z)$ becomes

$$\begin{aligned} Q(z) &= Q_{hom} + Q_{par} \\ &= C_1 e^{az} + C_2 e^{-az} \\ &\quad -q_1(z) \int \frac{q_2(z) G(z)}{W(q_1, q_2)(z)} dz + q_2(z) \int \frac{q_1(z) G(z)}{W(q_1, q_2)(z)} dz \end{aligned} \tag{B.12}$$

B.0.2 Particular solutions from uniform and linear zonal geostrophic wind profiles

The simplest Ekman spiral profile involves a functional form of $G(z)$ in (B.10) which is invariant with respect to height. i.e.,

$$G(z) = U_{go} \in \Re \tag{B.13}$$

Substituting the expression for $G(z)$ into (B.10) yields

$$Q_{par}(z) = -\frac{e^{az}}{2a}\int\left[e^{-az}\left(-a^2 Ugo\right)\right]dz + \frac{e^{-az}}{2a}\int\left[e^{az}\left(-a^2 Ugo\right)\right]dz \tag{B.14}$$

which, when simplified, becomes

$$Q_{par}(z) = \frac{U_{go}}{2} + \frac{U_{go}}{2} = U_{go} \tag{B.15}$$

and so

$$Q(z) = C_1 e^{az} + C_2 e^{-az} + U_{go} \tag{B.16}$$

In order to separate the U and V terms, the solution in (B.16) will be split into its real and imaginary components by replacing a with $\sqrt{\frac{if}{K_m}}$, by utilizing the identity $\sqrt{i} = \frac{1+i}{\sqrt{2}}$, and by setting $\gamma = \sqrt{\frac{f}{2K_m}}$.

$$U + iV = C_1 e^{(1+i)\gamma z} + C_2 e^{-(1+i)\gamma z} + U_{go} \tag{B.17}$$

Applying boundary conditions in (B.3) and (B.4) to (B.17) yields the following constants

$$\begin{aligned} C_1 &= 0 \\ C_2 &= -U_{go} e^{\gamma z_{sfc}(1+i)} \end{aligned} \tag{B.18}$$

The full solution for the Ekman spiral is thus given by

$$Q(z) = U + iV = U_{go}\left(1 - e^{\gamma\left(z_{sfc}-z\right)(1+i)}\right) \tag{B.19}$$

After separating the imaginary and real components using Euler's formula, the solution becomes

$$U = U_{go}\left(1 - e^{-\gamma\left(z-z_{sfc}\right)}\cos\gamma\left(z - z_{sfc}\right)\right) \tag{B.20}$$

$$V = U_{go} e^{-\gamma\left(z - z_{sfc}\right)} \sin\gamma\left(z - z_{sfc}\right) \tag{B.21}$$

A plot of the U and V components in (B.20) and (B.21) is shown in Fig. B-1. In Fig. B-1, increasing height corresponds to distance traversed along the curve. Both the zonal and meridional winds have an initial value of zero corresponding to the no-slip boundary condition at the surface. The curve asymptotically approaches the point $(1, 0)$ as expected, since the actual wind approaches the zonal geostrophic wind with increasing z. The first occurrence of a zero value for the meridional wind (aside from the origin) occurs at the height of $\frac{\pi}{\gamma}$. An Ekman spiral derived from a background zonal geostrophic wind with linear shear has a solution similar to (B.20) and (B.21). Assume that the zonal geostrophic wind is given by

$$u_g = U_{g*} + m_* \left(z - z_*\right) \tag{B.22}$$

where U_{g*}, m_*, and z_* are constants. (For the physical meaning of this profile, refer to Chapter 3.) Then the particular solution of the zonal and meridional momentum equations is given by:

$$\begin{aligned} Q_{par}\left(z\right) = & -\tfrac{e^{az}}{2a} \int \left[e^{-az}\left(-a^2\left(U_{g*} + m_*\left(z - z_*\right)\right)\right)\right] dz \\ & + \tfrac{e^{-az}}{2a} \int \left[e^{az}\left(-a^2\left(U_{g*} + m_*\left(z - z_*\right)\right)\right)\right] dz \end{aligned} \tag{B.23}$$

Solving this integral form results in the following particular solution,

$$\begin{aligned} Q_{par} &= \frac{a}{2}\left[\frac{U_{g*}}{a} + \frac{m}{a}\left(z - z_*\right) + \frac{m}{a^2} + \frac{U_{g*}}{a} + \frac{m}{a}\left(z - z_*\right) - \frac{m}{a^2}\right] \\ &= U_{g*} + m_*\left(z - z_*\right) = u_g \end{aligned} \tag{B.24}$$

Since the particular solution again reduces to the geostrophic wind, the general Ekman spiral solution becomes

$$U = \left(U_{g*} + m_*\left(z - z_*\right)\right)\left(1 - e^{-\gamma\left(z - z_{sfc}\right)} \cos\gamma\left(z - z_{sfc}\right)\right) \tag{B.25}$$

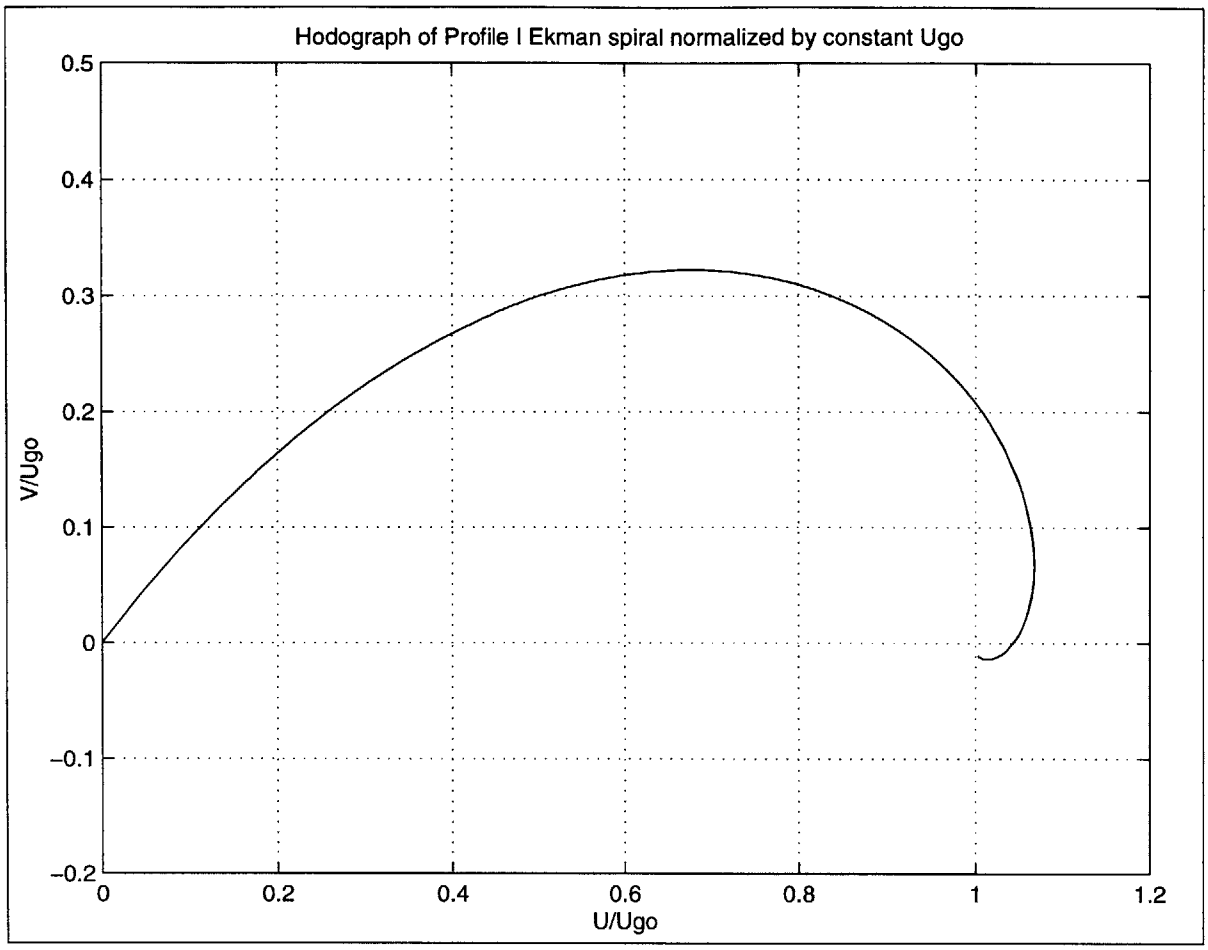

Figure B-1: This hodograph was generated using a zonal geostrophic wind which is invariant with respect to height. The background geostrophic wind is set at 15 m s^{-1}, the Ekman layer depth is assigned the value of 3500 m (corresponding to the point at which V first becomes zero), $\theta = 280$ K, and $f = 10^{-4}$ s^{-1}. The trajectory is parameterized from $z = 0$ m to $z = 5000$ m.

$$V = (U_{g*} + m_* (z - z_*)) e^{-\gamma(z - z_{sfc})} \sin \gamma (z - z_{sfc}) \tag{B.26}$$

The modified linear profile formulated in (B.25) and (B.26) is shown in Fig. B-2. Two features distinguish the Ekman spiral in the linear case from the z-invariant case. First, the normalized maximum meridional wind velocity is of lesser magnitude in Fig. B-2 than in Fig. B-1. This occurs as a result of the bulk decrease in the zonal wind between the two profiles, beneath the altitude $\frac{\pi}{\gamma}$. At the extrapolation point in the linear profile, $u_g = U_{go}$. Below $\frac{\pi}{\gamma}$ in the linear profile, the zonal geostrophic wind is smaller in Fig. B-2 than in Fig. B-1. Thus the Coriolis-deflected (meridional) component will also be reduced in this layer. The second difference in the linear geostrophic wind case is the flattened tail of the profile above $\frac{\pi}{\gamma}$, while the uniform profile asymptotically approaches $(1, 0)$. This effect is also a signature of the extrapolation procedure in the linear profile. Above $\frac{\pi}{\gamma}$, the geostrophic wind continues to increase without bound in the linear case, while the deflected meridional wind continues to decay. In contrast, the geostrophic wind in Fig. B-1 remains fixed with increasing altitude, so the curve spirals into a stable pole.

B.0.3 Particular solutions from exponentially weighted composite geostrophic wind profiles

The final solution to be analyzed is a composite geostrophic wind profile consisting of the sum of two exponentially-weighted linear profiles. The explicit form of this zonal geostrophic wind profile is given by

$$\begin{aligned} u_g = \; & [U_{g*,LS} + m_{LS} (z - z_{LS})] \left(1 - e^{-\frac{z - z_{sfc}}{z_{scl}}}\right) \\ & + [U_{g*,SS} + m_{SS} (z - z_{SS})] e^{-\frac{z - z_{sfc}}{z_{scl}}} \end{aligned} \tag{B.27}$$

where $U_{g*,LS}, m_{LS}, z_{LS}, z_{scl}, U_{g*,SS}, m_{SS}, z_{SS} \in \Re$, and with the forcing function $G(z)$ given by

$$G(z) = -a^2 \left([U_{g*,LS} + m_{LS} (z - z_{LS})] \left(1 - e^{-\frac{z - z_{sfc}}{z_{scl}}}\right) \right.$$

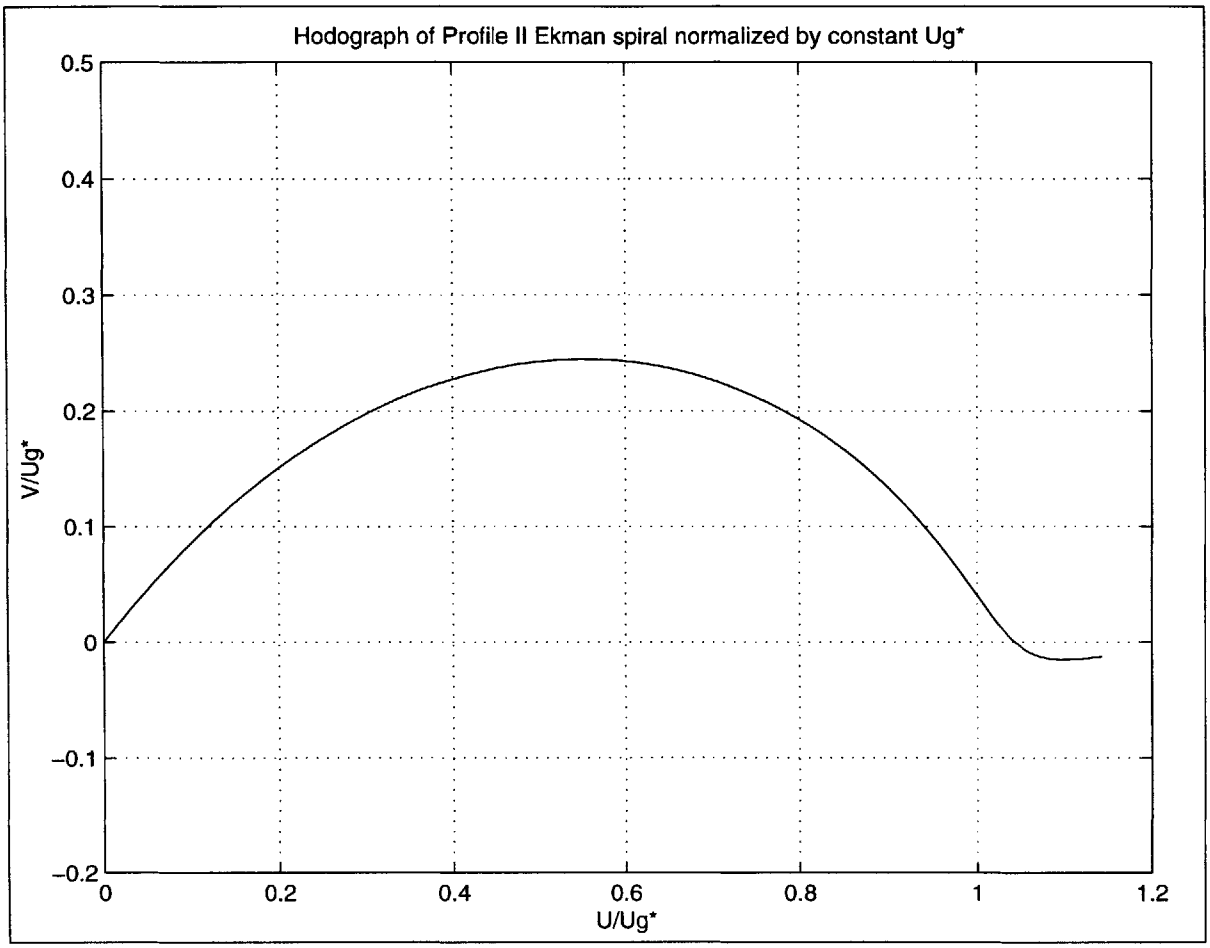

Figure B-2: This Ekman spiral solution assumes a zonal geostrophic wind which varies linearly with respect to height. The background geostrophic wind is set to 15 m s^{-1} at the extrapolation point, the Ekman layer depth is assigned the value of 3500 m (corresponding to the point at which $V = 0$), $m = .0014$ s^{-1}, and $f = 10^{-4}$ s^{-1}. The altitude of the extrapolation point is assigned as the depth of the Ekman layer. The hodograph is parameterized from $z = 0$ m to $z = 5000$ m.

$$+\left[U_{g*,SS}+m_{SS}\left(z-z_{SS}\right)\right]e^{-\frac{z-z_{sfc}}{z_{scl}}}\Big) \tag{B.28}$$

Simplifying (B.28) in terms of the independent functional forms of z,

$$\begin{aligned} G\left(z\right) &= -a^2\left(A_1+A_2z+A_3e^{-\left(z-z_{sfc}\right)b}+A_4ze^{-\left(z-z_{sfc}\right)b}\right) \\ &= g_a\left(z\right)+g_b\left(z\right)+g_c\left(z\right)+g_d\left(z\right) \end{aligned} \tag{B.29}$$

where $b=\frac{1}{z_{scl}}$, and given that

$$\begin{aligned} g_a\left(z\right) &= -a^2A_1=-a^2\left(U_{g*,LS}-m_{LS}z_{LS}\right) \\ g_b\left(z\right) &= -a^2A_2z=-a^2m_{LS}z \\ g_c\left(z\right) &= -a^2A_3e^{-\left(z-z_{sfc}\right)b}=-a^2\left(-U_{g*,LS}+m_{LS}z_{LS}+U_{g*,SS}-m_{SS}z_{SS}\right)e^{-\left(z-z_{sfc}\right)b} \\ g_d\left(z\right) &= -a^2A_4ze^{-\left(z-z_{sfc}\right)b}=-a^2\left(m_{SS}-m_{LS}\right)ze^{-\left(z-z_{sfc}\right)b} \end{aligned} \tag{B.30}$$

The particular solution may then be expressed as the sum of the particular solutions calculated from the four terms of the forcing function in (B.29)

$$Q_{par}=q_a+q_b+q_c+q_d \tag{B.31}$$

where

$$\begin{aligned} q_a &= -\frac{e^{az}}{2a}\int\left[e^{-az}g_a\left(z\right)\right]dz+\frac{e^{-az}}{2a}\int\left[e^{az}g_a\left(z\right)\right]dz \\ q_b &= -\frac{e^{az}}{2a}\int\left[e^{-az}g_b\left(z\right)\right]dz+\frac{e^{-az}}{2a}\int\left[e^{az}g_b\left(z\right)\right]dz \\ q_c &= -\frac{e^{az}}{2a}\int\left[e^{-az}g_c\left(z\right)\right]dz+\frac{e^{-az}}{2a}\int\left[e^{az}g_c\left(z\right)\right]dz \\ q_d &= -\frac{e^{az}}{2a}\int\left[e^{-az}g_d\left(z\right)\right]dz+\frac{e^{-az}}{2a}\int\left[e^{az}g_d\left(z\right)\right]dz \end{aligned} \tag{B.32}$$

After substituting the expressions of the forcing functions in (B.30) into (B.32) the following particular solutions follow after the integrals are evaluated:

$$\begin{aligned} q_a &= A_1 = U_{g*,LS} - m_{LS} z_{LS} \\ q_b &= A_2 z = m_{LS} z \\ q_c &= \frac{a^2 A_3}{(a+b)(a-b)} e^{-(z-z_{sfc})b} \\ q_d &= \frac{a^2 A_4}{(a+b)^2 (a-b)^2} \left(za^2 - zb^2 - 2b\right) e^{-(z-z_{sfc})b} \end{aligned} \tag{B.33}$$

Solutions q_a and q_b are strictly real. The final two solutions, q_c and q_d, contain both real and imaginary components. To separate these components, consider the following calculations derived from rules of complex analysis.

$$\frac{a^2}{(a+b)(a-b)} = \frac{4\gamma^4 - 2i\gamma^2 b^2}{b^4 + 4\gamma^4} \tag{B.34}$$

$$\frac{a^4}{(a+b)^2 (a-b)^2} = \frac{(16\gamma^8 - 4b^4\gamma^4) - 16ib^2\gamma^6}{b^8 + 8\gamma^4 b^4 + 16\gamma^8} \tag{B.35}$$

$$\frac{-a^2 b^2}{(a+b)^2 (a-b)^2} = \frac{8b^4\gamma^4 + i\left(8b^2\gamma^6 - 2b^6\gamma^2\right)}{b^8 + 8\gamma^4 b^4 + 16\gamma^8} \tag{B.36}$$

$$\frac{-2a^2 b}{(a+b)^2 (a-b)^2} = \frac{16b^3\gamma^4 + i\left(16b\gamma^6 - 4b^5\gamma^2\right)}{b^8 + 8\gamma^4 b^4 + 16\gamma^8} \tag{B.37}$$

Note the following variable substitutions corresponding to the real and imaginary components of the coefficients in q_c and q_d:

$$D_3 = \frac{4\gamma^4}{b^4 + 4\gamma^4} \tag{B.38}$$

$$E_3 = \frac{-2\gamma^2 b^2}{b^4 + 4\gamma^4} \tag{B.39}$$

$$D_4 = \frac{16\gamma^8 - 4b^4\gamma^4}{b^8 + 8\gamma^4 b^4 + 16\gamma^8} \tag{B.40}$$

$$E_4 = \frac{-16b^2\gamma^6}{b^8 + 8\gamma^4 b^4 + 16\gamma^8} \tag{B.41}$$

$$D_5 = \frac{8b^4\gamma^4}{b^8 + 8\gamma^4 b^4 + 16\gamma^8} \tag{B.42}$$

$$E_5 = \frac{8b^2\gamma^6 - 2b^6\gamma^2}{b^8 + 8\gamma^4 b^4 + 16\gamma^8} \tag{B.43}$$

Utilizing the constants in (B.38), (B.39),(B.40), (B.41), (B.42), and (B.43), the particular solutions q_c and q_d become

$$q_c = (D_3 + iE_3) A_3 e^{-(z-z_{sfc})b} \tag{B.44}$$

$$q_d = \left[A_4 \left((D_4 + D_5) + i\left(E_4 + E_5\right)\right) z + A_4 \left(D_6 + iE_6\right)\right] e^{-(z-z_{sfc})b} \tag{B.45}$$

Summing the particular solutions and parsing into the real and imaginary components according to functions of z, the following solution results

$$\begin{aligned} Q_{par} = \quad & D_1 + D_2 z + \left[A_3 \left(D_3 + iE_3\right) + A_4 \left(D_6 + iE_6\right)\right] e^{-(z-z_{sfc})b} \\ & + \left[A_4 \left(\left(D_4 + D_5\right) + i\left(E_4 + E_5\right)\right)\right] z e^{-(z-z_{sfc})b} \end{aligned} \tag{B.46}$$

where $D_1 = U_{g*,LS} - m_{LS} z_{LS}$ and $D_2 = m_{LS}$. The general solution assumes the following form, according to (B.12)

$$\begin{aligned} Q(z) &= U + iV = Q_{hom} + Q_{par} \\ &= C_1 e^{az} + C_2 e^{-az} \\ &\quad + D_1 + D_2 z \\ &\quad + \left[A_3 \left(D_3 + iE_3\right) + A_4 \left(D_6 + iE_6\right)\right] e^{-(z-z_{sfc})b} \\ &\quad + \left[A_4 \left(\left(D_4 + D_5\right) + i\left(E_4 + E_5\right)\right)\right] z e^{-(z-z_{sfc})b} \end{aligned} \tag{B.47}$$

For further clarity, let $J_3 = A_3D_3 + A_4D_6$, $J_4 = A_4D_4 + A_4D_5$, $K_3 = A_3E_3 + A_4E_6$, and $K_4 = A_4E_4 + A_4E_5$, so

$$\begin{aligned} Q(z) &= C_1e^{az} + C_2e^{-az} + D_1 + D_2z \\ &\quad + (J_3 + iK_3)\, e^{-(z-z_{sfc})b} + (J_4 + iK_4)\, ze^{-(z-z_{sfc})b} \end{aligned} \tag{B.48}$$

Applying the boundary condition (B.4) to the solution for the Ekman spiral winds in (B.47) again yields the constraint that $C_1 = 0$. (Note that $ze^{-(z-z_{sfc})b} \to 0$ as $z \to \infty$.) The surface constraint (B.3) determines the second coefficient of the homogeneous solution,

$$C_2 = -\left[D_1 + D_2z_{sfc} + (J_3 + iK_3) + (J_4 + iK_4)\, z_{sfc}\right] e^{az_{sfc}} \tag{B.49}$$

The expressions for C_1 and C_2 are now substituted into (B.48) and the real and imaginary components are separated to yield the final form of the Ekman spiral winds for the exponentially weighted geostrophic wind.

$$\begin{aligned} U &= -(D_1 + D_2z_{sfc} + J_3 + J_4z_{sfc})\, e^{-\gamma(z-z_{sfc})} \cos\gamma(z - z_{sfc}) \\ &\quad -(K_3 + K_4z_{sfc})\, e^{-\gamma(z-z_{sfc})} \sin\gamma(z - z_{sfc}) \\ &\quad +D_1 + D_2z + J_3e^{-(z-z_{sfc})b} + J_4ze^{-(z-z_{sfc})b} \end{aligned} \tag{B.50}$$

$$\begin{aligned} V &= -(K_3 + K_4z_{sfc})\, e^{-\gamma(z-z_{sfc})} \cos\gamma(z - z_{sfc}) \\ &\quad +(D_1 + D_2z_{sfc} + J_3 + J_4z_{sfc})\, e^{-\gamma(z-z_{sfc})} \sin\gamma(z - z_{sfc}) \\ &\quad K_3e^{-(z-z_{sfc})b} + K_4ze^{-(z-z_{sfc})b} \end{aligned} \tag{B.51}$$

The explicit formulae for the total wind speeds in (B.50) and (B.51) are plotted in Fig. B-3. The Ekman spiral from the exponential profile produces an enhanced

meridional wind maximum at a level lower than the corresponding feature in Fig. B-2. In this particular example, the geostrophic wind begins at the surface at a value higher than that in the linear profile, then decreases with height initially, and then increases at a rate approaching that of the linear profile. In general, the geostrophic wind at the surface is governed by the small-scale geostrophic wind profile, while at greater altitudes the large scale wind has a greater effect.

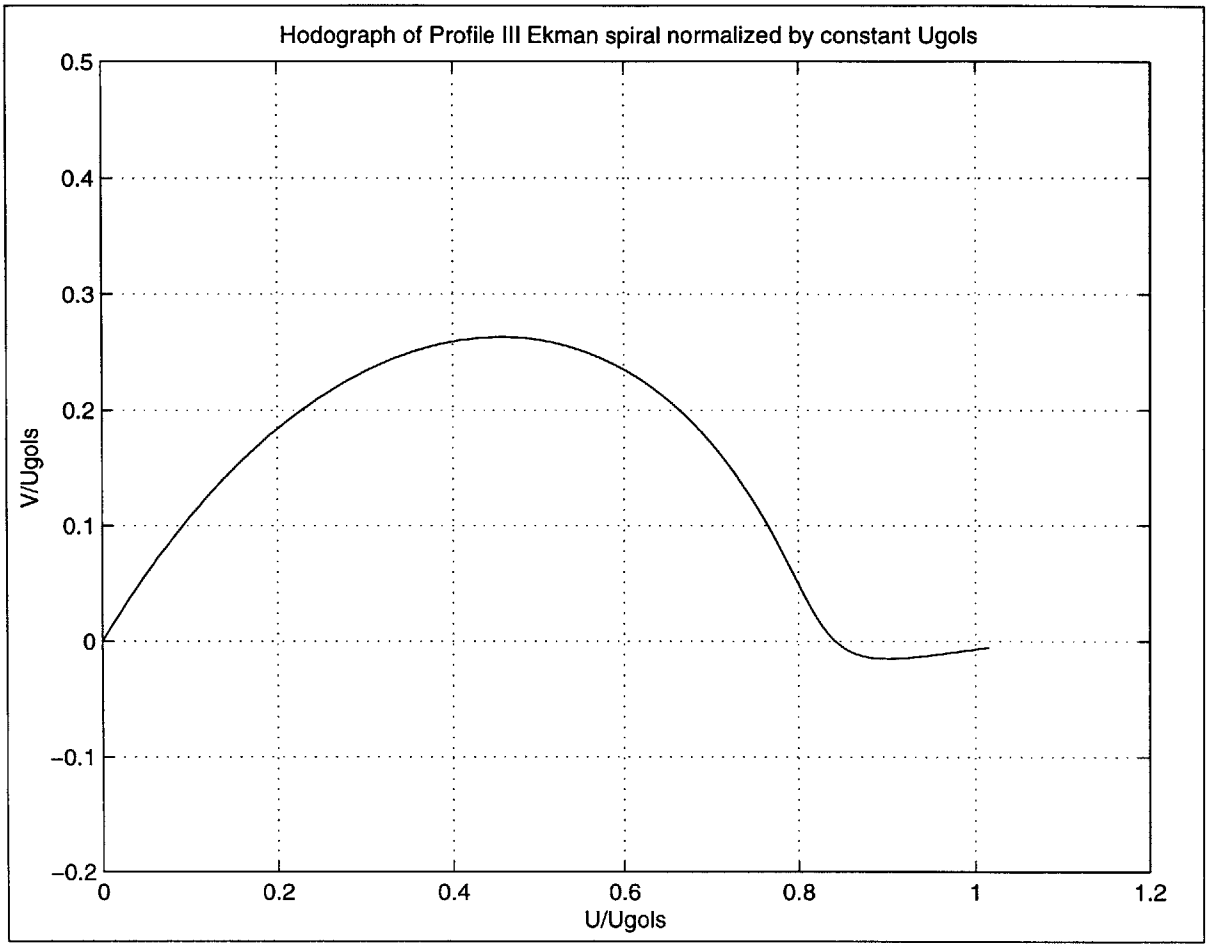

Figure B-3: This hodograph was generated using a zonal geostrophic wind composed of the sum of two exponentially weighted linear profiles. In computing the trajectory, the following values were used: $m_{LS} = .0014$ s^{-1}, $m_{SS} = -.004$ s^{-1}, Ekman layer depth = 3500 m, $U_{g*,LS} = 15$ m s^{-1}, $z_{LS} = 3500$ m, $z_{scl} = 3500$ m, $U_{g*,SS} = 15$m s^{-1}, $z_{SS} = 0$.

Bibliography

Arritt, R. W., Rink, T. D., Segal, M., Todey, D. P. and Clark, C. A. (1997). The Great Plains low-level jet during the warm season of 1993, *Monthly Weather Review* **125**: 2176–2192.

Augustine, J. A. and Caracena, F. (1994). Lower-tropospheric precursors to nocturnal MCS over the Central United States, *Weather and Forecasting* **9**: 116–135.

Blackadar, A. K. (1957). Boundary layer wind maxima and their significance for the growth of nocturnal inversions, *Bulliten of the American Meteorological Society* **38**: 283–290.

Bleeker, W. and Andre, M. J. (1951). On the diurnal variations of precipitation, paritcularly over central U.S.A., and its relation to large-scale orographic circulation systems, *Quarterly Journal of the Royal Meteorological Society* **77**: 260–271.

Bonner, W. D. (1966). Case study of thunderstorm activity in relation to the low-level jet, *Monthly Weather Review* **94**: 167–178.

Bonner, W. D. (1968). Climatology of the low level jet, *Monthly Weather Review* **96**: 833–850.

Boyce, W. E. and DiPrima, R. C. (1992). *Elementary Differential Equations and Boundary Value Problems*, John Wiley and Sons, Inc., New York, NY.

Fast, J. D. and McCorcle, M. D. (1990). A two-dimenstional numerical sensitivity study of the Great Plains low-level jet, *Monthly Weather Review* **118**: 151–163.

Gerhardt, J. R. (1962). An example of a nocturnal low-level jet stream, *Journal of the Atmospheric Sciences* **19**: 116–118.

Helfand, H. M. and Schubert, S. D. (1995). Climatology of the simulated Great Plains low-level jet and its contribution to the continental moisture budget of the United States, *Journal of Climate* **8**: 784–806.

Hess, S. L. (1959). *Introduction to theoretical meteorology*, Robert Krieger Publishing Company, Malabar, FL.

Hoecker, W. J. (1963). Three southerly low-level jet systems delineated by the Weather Bureau special pibal network of 1961, *Monthly Weather Review* **91**: 573–582.

Holton, J. R. (1967). The diurnal boundary layer wind oscillation above sloping terrain, *Tellus* **19**: 199–205.

Holton, J. R. (1992). *An introduction to dynamic meteorology*, Academic Press, Inc., San Diego, California.

Izumi, Y. (1964). The evolution of temperature and velocity profiles during breakdown of a nocturnal inversion and a low-level jet, *Journal of Applied Meteorology* **3**: 70–82.

Izumi, Y. and Barad, M. L. (1963). Wind and temperature variations during development of a low-level jet, *Journal of Applied Meteorology* **2**: 668–673.

Kim, C. P. and Entekhabi, D. (1998). Feedbacks in the land-surface and mixed-layer energy budgets, *Boundary Layer Meteorology* **88**: 1–21.

Mahrt, L. (1977). Influence of low-level environment on severity of high-plains moist convection, *Monthly Weather Review* **105**: 1315–1329.

Mahrt, L. J. and Schwerdtfeger, W. (1970). Ekman spirals for exponential thermal wind, *Boundary-Layer Meteorology* **1**: 137–145.

McCorcle, M. D. (1988). Simulation of the surface-moisture effects on the Great Plains low-level jet, *Monthly Weather Review* **116**: 1705–1720.

McNider, R. T. and Pielke, R. A. (1981). Diurnal boundary-layer development over sloping terrain, *Journal of the Atmospheric Sciences* **38**: 2198–2212.

Means, L. L. (1954). A study of the mean southerly wind-maximum in low levels associated with a period of summer precipitation in the Middle West, *Bulliten of the American Meteorological Society* **35**: 166–170.

Paegle, J. and McLawhorn, D. W. (1983). Numerical modelling of diurnal convergence oscillations above sloping terrain, *Monthly Weather Review* **111**: 67–85.

Paegle, J., Paegle, J. N., McCorcle, M. and Miller, E. (1984). Diagnoses and numerical simulation of a low-level jet during ALPEX, *Contributions to Atmospheric Physics* **57**: 419–430.

Parish, T. R., Rodi, A. R. and Clark, R. D. (1988). A case study of the summertime Great Plains low level jet, *Monthly Weather Review* **116**: 94–105.

Pitchford, K. L. and London, J. (1962). The low-level jet as related to nocturnal thunderstorms over the Midwest United States, *Journal of Applied Meteorology* **1**: 43–47.

Rasmusson, E. M. (1967). Atmospheric water vapor transport and the water balance of North America: Part I. Characteristics of the water vapor flux field, *Monthly Weather Review* **95**: 403–426.

Singh, M. P., McNider, R. T. and Lin, J. T. (1993). An analytical study of diurnal wind-structure variations in the boundary layer and the low-level nocturnal jet, *Boundary-Layer Meteorology* **63**: 397–423.

Smeda, M. S. (1979). A bulk model for the atmospheric boundary layer, *Boundary-Layer Meteorology* **17**: 411–427.

Wallace, J. M. (1975). Diurnal variations in precipitation and thunderstorm frequency over the conterminous United States, *Monthly Weather Review* **103**: 406–419.

Wexler, H. (1961). A boundary layer interpretation of the low-level jet, *Tellus* **13**: 368–378.

Whiteman, C. D., Bian, X. and Zhong, S. (1997). Low-level jet climatology from enhanced rawinsonde observations at a site in the southern Great Plains, *Journal of Applied Meteorology* **36**: 1363–1376.

Wipperman, F. (1973). Numerical study on the effects controlling the low-level jet, *Contributions to Atmospheric Physics* **46**: 137–154.

Zeman, O. (1979). Parameterizations of the dynamics of stable boundary layers and nocturnal jets, *Journal of the Atmospheric Sciences* **36**: 792–804.

Zhong, S., Fast, J. D. and Bian, X. (1996). A case study of the Great Plains low-level jet using wind profiler network data and a high-resolution mesoscale model, *Monthly Weather Review* **124**: 785–806.